



**University of
Nottingham**

UK | CHINA | MALAYSIA

**COMPOSITES OF MWCNTS AND METAL
OXIDES (HYDROXIDES) PREPARED VIA
FENTON REACTION AND THEIR
APPLICATIONS IN LIBS AND OER**

Xiaojuan LIU, MSc, BEng.

**Thesis submitted to the University of Nottingham
for the degree of Doctor of Philosophy**

March 2019

Abstract

With the rapid development of society, the soaring consumption on fossil energy and the heavy environmental deterioration, looking for sustainable and clean energy such as solar, wind, hydrogen, has become the top priority for improving the environment pollution and accelerating the economic growth. However, the time and region limitation unable to meet the regional demand of energy, therefore, the research of effective energy storage and conversion (EESC) devices has become the research priorities. Lithium ion batteries (LIBs) as one of the EESC devices have been studied by many research groups. Oxygen evolution reaction (OER), as the anode reaction in water splitting and positive electrode charging reaction in metal-air batteries, plays a crucial role in the field of EESC. Composites of carbon material and metal oxide (or hydroxide) with their intrinsic properties can be used in the above two field as an anode or an electrocatalyst, respectively. But the common preparation method published in most articles for this type of composites usually contains two steps: first, the carbon materials should be oxidized to introduce oxygen functional groups to react with metal ions, then followed with hydrothermal reaction to make sure the reaction happened between oxidized carbon material and metal ions and finally to generate the composites of carbon materials and metal oxides.

Herein, Fenton reaction with Fenton reagents (Fe^{2+} - H_2O_2) was used to synthesize composites of carbon material and metal oxides (or hydroxides). Because carbon material could be firstly oxidized by Fenton reagents and secondly Fe^{3+} in Fenton reagents can be used as iron sources. Hence, in this work, composites of $\text{Fe}(\text{OH})_3$ and expandable graphite nanosheets ($\text{Fe}(\text{OH})_3/\text{EG}$), $\text{Fe}(\text{OH})_3$ and multi-walled carbon

nanotubes ($\text{Fe}(\text{OH})_3/\text{MWCNTs}$), $\text{Fe}_2\text{O}_3/\text{MWCNTs}$, NiFe layered double hydroxides and MWCNTs (NiFe LDHs/MWCNTs) were prepared by Fenton reaction with sonication assistance. and $\text{Fe}_2\text{O}_3/\text{MWCNTs}$ used as anode material in LIBs and NiFe LDHs/MWCNTs used as electrocatalyst for OER were investigated, respectively.

Firstly, after a series of comparison, acidified EG after dealing with Fenton reaction (AEG-F) show higher capacity than that of EG after reacting with Fenton reaction (EG-F), because surface of AEG has oxygen functional groups which can easily react with Fenton reagent, while EG with worm-like structure were not easily reacted with Fenton reagents due to the thick layered structure. However, considering the energy consumption and side-product generated in the process of preparing AEG by concentrated sulfuric and nitric, AEG is not suitable as a raw material for preparing composite used in this work. MWCNTs as a type of carbon materials show high conductivity and have network structure which is beneficial for MWCNTs applied as the substrate for preparing composites of carbon materials and metal oxides (or hydroxides). After Fenton reaction, MWCNTs-F have high capacity due to the network structure and high conductivity of MWCNTs compared with EG-F. Considering the temperature influence on particle size and crystal structure of metal hydroxide in the process of crystallization, hydrothermal treatment was applied after Fenton reaction which was named as EG-F-H and MWCNTs-F-H, respectively. However, the results show that MWCNTs-F without hydrothermal reaction has higher capacities than that of MWCNTs-F-H. Because the particle size of metal hydroxide on MWCNTs-F surface is smaller than that of MWCNTs-F-H, and part of metal hydroxide particles located on the surface of MWCNTs-F could drop down to the solution during the hydrothermal

reaction. And EG-F also show a higher capacity than that of EG-F-H. In the Fenton reaction process, sonication was used to enhance the reaction. Hence, the optimized sonication time was also selected according to the properties of composites and the optimized sonication time is 3h.

Composite of $\text{Fe}_2\text{O}_3/\text{MWCNTs}$ was prepared by Fenton reaction with a heat treatment (200°C) to ensure that $\text{Fe}(\text{OH})_3$ was transferred to Fe_2O_3 . It was characterized by X-ray diffraction (XRD), scanning electron microscopy (SEM), Fourier-transform infrared spectroscopy (FT-IR) etc. The XRD and Selected area electron diffraction (SAED) display that Fe_2O_3 in the composite has an amorphous structure, and SEM shows Fe_2O_3 nanoparticles load on MWCNTs surface. This indicates that MWCNTs was oxidized by Fenton reagents and introduced oxygen functional groups with negative charge. The electrostatic interaction between MWCNTs and iron ions with positive charge finally promote the production of composite of $\text{Fe}_2\text{O}_3/\text{MWCNTs}$. The electrochemical measurement for composite used as an anode in LIBs shows that the composite of $\text{Fe}_2\text{O}_3/\text{MWCNTs}$ exhibits an excellent cycle performance with a reversible capacity of 900 mAh/g at 500 mA/g after 500 cycles and a high rate capability of 785 mAh/g at a high current density of 2 A/g. It is ascribed that the random ordered amorphous structure of Fe_2O_3 decreases the ion pathway and increase the diffusion of Li ions. The MWCNTs substrate provides an electronic path way and promotes the charge transportation and enhances the rate capability.

Herein, NiFe LDHs/MWCNTs as an electrocatalyst used as a type of EESC was also synthesized by obtained by Fenton reaction followed with a coprecipitation process. Ni ions was simply added into the suspension of MWCNTs after the process of Fenton

reaction under pH=9-10, NiFe LDHs/MWCNTs was obtained. XRD and SAED images indicate that the composites have low crystalline structure because the temperature and pressure used in this reaction is room temperature and atmospheric pressure with short reaction time. Linear sweep voltammetry (LSV), Chronopotentiometry (CP) and multi-CP were used to test their electrocatalytic properties. The results show that F(3-1)3 (named based on total ration and molar ratio between Ni: Fe explained in experimental part) displays excellent electrocatalytic properties with small overpotential of 212 mV and 283 mV at 10 mA/cm² and 100 mA/cm², respectively, and a few Tafel slope of 64.46 mV/dec. The outstanding electrocatalytic performance is traced to the low crystal structure of NiFe LDHs nanoparticles which could expose more active sites and facilitate the reaction between electrode and electrolyte. MWCNTs is also responsible for the excellent electrocatalytic properties, because MWCNTs enhance the conductivity of composites and improve the kinetic of OER.

Achievements

1. Journal papers

Xiaojuan Liu, TaoWu, Zengxin Dai, Keran Tao, Yong Shi, Chuang Peng, Xiaohang Zhou, George Z. Chen Bipolarly stacked electrolyser for energy and space efficient fabrication of supercapacitor electrodes. *Journal of Power Sources*, 2016, 307: 208-213.

2. Journal Papers under Preparation

Xiaojuan Liu, Shizhen Li, Bamidele AKINWOLEMIWA Honglei Zhang, Tao Wu and Chuang Peng. Low-crystalline NiFe LDHs/MWCNTs composite electrocatalyst for oxygen evolution reaction by Fenton reaction inspired green synthesis. *Green Chemistry*, under preparation.

Xiaojuan Liu, Shizhen Li, Bamidele AKINWOLEMIWA Honglei Zhang, Tao Wu and Chuang Peng. Scalable preparation of Fe₂O₃/MWCNTs by Fenton reaction and its application for lithium ion batteries. *Journal of Alloys and Compounds*, under preparation.

Acknowledgements

After the experimental work and writing, this thesis was finally accomplished. Without the help of many people, it could never be completed, thus here I would like to express my sincere gratitude towards them.

Firstly, I would like to express my heartfelt thanks to my distinguished and cordial supervisor Prof. Tao Wu at The University of Nottingham Ningbo China, who influenced me with his insightful ideas and meaningful inspirations, guided me with practical academic advice and feasible instructions, and enlightened me while I was confused during the experimental procedure. I also owe my sincere gratitude to my supervisor Prof. Chuang Peng at Wuhan University, for his support and supervision throughout this work. His thought-provoking comments and patiently encouragements are indispensable for my accomplishment of this thesis. Without his dedicated assistance and insightful supervision, this thesis could never be finished. I also learned a lot from my supervisors especially the way of thinking to meet challenges during the process of experiment and life.

Sincere thanks should be expressed to Julian Zhu, Jane Zhang, Carey Tao and Helen Xu for providing the most helpful lab help. And I would also like to express my thanks to all members of staff at the Department of Chemical Engineering Prof. George Chen, Dr. Di Hu, Dr. Bencan Tang, Dr. Linbo Yu, and Dr. Philip Hall for their help throughout this work.

My special gratitude also goes to my fellow classmates and friends at UNNC: Dr. Kaiqi Shi, Dr. Jiefeng Yan, Dr. Haitao Zhao, Dr. Honglei Zhang, Dr. Xiang Luo, Dr.

Hong Yu, Dr. Wanru Chen, Dr. Bamidele Akinwolemiwa, Chaohui Wei, Matthew Thomas Bishop, Gang Yang, and at Wuhan University: Shizhen Li, Yin Cui, Fang Yu, Xin Ma, Danqing, Su, Yating Zhou, Lingyun Xu, Yingjie Li, Fangxuan Liu and Bailing Liu for their help and friendship.

University of Nottingham is also acknowledged for its generosity on providing me PhD scholarship.

Ultimately, thanks for my parents and my husband who are my mentor and guardian of the life. Without their support, understanding and encouragement, I have no the courage to confront any obstacles on my way to finish my PhD.

Table of Contents

Abstract	I
Achievements	V
Acknowledgements	VI
Table of Contents	VIII
List of Figures	XI
List of Tables	XVIII
List of Abbreviations	XIX
List of Nomenclature	XXIII
Chapter 1 Introduction	1
1.1 Research Background	1
1.2 Aim and Objectives.....	3
1.3 Structure of the Thesis	5
Chapter 2 Literature Review	6
2.1 Basic Introduction.....	6
2.2 Overview for LIBs	7
2.2.1 Introduction.....	7
2.2.2 Fe ₂ O ₃ with Carbon Materials	8
2.2.3 Conclusion	27
2.3 Overview for OER	28
2.3.1 Introduction.....	28
2.3.2 Mechanism and Electrocatalytic Kinetic of OER.....	30
2.3.3 The Design Strategies	40
2.3.4 Materials Used in OER	42
Chapter 3 Experiment	68
3.1 Introduction.....	68
3.2 Chemicals and Materials.....	68
3.3 Instruments for Preparation and Test.....	70
3.4 Characterization	72
3.4.1 XRD	72
3.4.2 SEM	72
3.4.3 TEM and EDX	72
3.4.4 FT-IR.....	73

3.4.5 XPS	73
3.4.6 N ₂ Adsorption-Desorption Measurement	73
3.5 Electrochemical Measurements for LIBs.....	74
3.5.1 Preparation of Electrode Pad and Assembling Coin Cell.....	74
3.5.2 Land Test	75
3.5.3 CV and EIS	75
3.6 Electrochemical Measurement for OER	75
3.6.1 Preparation of Electrode	75
3.6.2 Electrochemical Test.....	76
Chapter 4 Preparation of Composites of Fe(OH)₃/EG Nanosheets and Fe(OH)₃/MWCNTs and Their Electrochemical Performance.....	77
4.1 Introduction.....	77
4.2 Experimental Section	77
4.2.1 Preparation of Composites.....	77
4.2.2 Electrochemical Test.....	79
4.3 Characterization	79
4.3.1 pH Control	80
4.3.2 Comparison of EG and AEG	83
4.3.3 Comparison of EG and MWCNTs.....	87
4.3.4 The Sonication Time Influence on Cycling Performance.....	90
4.4 Conclusion	92
Chapter 5 Scalable Preparation of Fe₂O₃/MWCNTs by Fenton Reaction and Their Application in LIBs	93
5.1 Introduction.....	93
5.2 Experimental Section	93
5.2.1 Preparation of Material of Fe ₂ O ₃ /MWCNTs	93
5.3 Materials Characterization	94
5.3.1 SEM and TEM	94
5.3.2 XRD	95
5.3.3 FT-IR.....	96
5.3.4 N ₂ Adsorption-Desorption Measurement	97
5.3.5 XPS	98
5.4 Electrochemical Test.....	99
5.4.1 CV	99
5.4.2 GCD	101
5.4.3 Cycling Performance and Rate Capability.....	102
5.4.4 EIS.....	104
5.5 Summary	105

Chapter 6 Low-Crystalline NiFe LDHs/MWCNTs Composites Fabricated by Fenton Reaction and Their Application in OER	107
6.1 Introduction.....	107
6.2 Experiment Section.....	107
6.3 Material Characterization.....	108
6.3.1 SEM and TEM	108
6.3.2 XRD	109
6.3.3 N ₂ Adsorption-Desorption Measurement	111
6.3.4 XPS	113
6.4 Electrochemical Measurements	115
6.4.1 LSV and Tafel plot.....	115
6.4.2 CP/Multi-CP	116
6.4.3 ECSA and Faradic Efficiency	118
6.5 XPS Test for Composites after Activation.....	121
6.6 Summary	122
Chapter 7 Summary and Future Work.....	124
7.1 The Comparison Between Different Composites Prepared by Fenton Reaction	124
7.2 Preparation of Composite of Fe ₂ O ₃ /MWCNTs and Their Application as Anode in LIBs	125
7.3 Preparation of NiFe LDHs/MWCNTs Composites and Their Application as Electrocatalyst in OER.....	125
7.4 Further Work.....	126
Bibliography	128

List of Figures

- Fig. 2-1 Schematic diagram of the lithium intercalation-de-intercalation reaction mechanism in a rechargeable lithium-ion battery containing solid electrodes and a liquid electrolyte. Cited from ref (Qi et al. 2017).8**
- Fig. 2-2 (a) Schematic of the synthesis of Fe₂O₃/SWCNT membrane, (b) photograph of the flexible membrane obtained after oxidation; (c) SEM images of the Fe₂O₃/SWCNT membrane and corresponding EDS spectrum (inset unit: KeV) Cited from Ref (Zhou et al. 2012) (d) Preparation procedures of Fe₂O₃ nanoparticles/MWCNTs composite film. Cited from Ref (Yang et al. 2015). 11**
- Fig. 2-3 (a) Formation mechanism of H-Fe₂O₃/MWCNTs microspheres, Electrochemical properties of β-FeOOH/ MWCNTs microspheres, H-Fe₂O₃/MWCNTs microspheres and dense Fe₂O₃ nanorods: (b) cycling performance along with columbic efficiencies at 1A/g; (c) rate capability at various current densities. Cited from Ref (Park, Park and Kang 2018). 13**
- Fig. 2-4 (a) Schematic illustration of preparation of carbon coated α-Fe₂O₃ hollow nano-horns on MWCNTs backbones; (b) TEM images of carbon coated MWCNTs@ Fe₂O₃ hierarchical structures; Cited from Ref (Wang et al. 2012) (c-e) schematic of α- Fe₂O₃ nanorods/MWCNTs-GF fabrication stage: (c) GF, (d) MWCNTs-GF, (e) Fe₂O₃ /MWCNTs-GF, (f-h)the corresponding SEM images. Cited from Ref (Chen et al. 2014). 16**
- Fig. 2-5 (a) Schematic of recyclable process for scalable controlled assembly of α-Fe₂O₃ nanocrystals on flexible CTs; (b) patterns of FeOOH@CTs and Fe₂O₃@CTs obtained at different CBD temperature. (c) schematic of crack and exfoliation of**

α - Fe₂O₃ with large mass loading on the CTs; SEM images of (d, e) Fe₂O₃@CTs-70 and (f, g) α - Fe₂O₃ @CTs-80 after 100 cycles at 0.5C in the voltage range from 0.01 to 3.0 V; (h) schematic of the enhanced stability and electronic interconnections of ultrathin α - Fe₂O₃ nanocrystals onto the CTs; SEM images of (i, j) Fe₂O₃ @CTs-90 and (m, n) Fe₂O₃@CTs-100 after 100. cited from Ref (Xiong et al. 2018). 24

Fig. 2-6 Polarization curves for HER (left) and OER (right). The η_c and η_a are the overpotentials for cathode and anode at the same current (j), respectively. Cited from Ref (Suen et al. 2017). 29

Fig. 2-7 The OER mechanism for acid (blue line) and alkaline (red line) conditions. The black line indicates that the oxygen evolution involves the formation of a peroxide (M-OOH) intermediate (black line) while another route for direct reaction of two adjacent oxo (M-O) intermediates (green) to produce oxygen is possible as well. Cited from Ref (Suen et al. 2017). 31

Fig. 2-8 (a) Schematic illustration of preparation procedure for flexible OER electrocatalyst based on polymer@MWCNTs composite membranes, (b) a photograph of the flexible free-standing PEMAs@MWCNTs 90 membrane. Cited form Ref (Zhang et al. 2017b). 46

Fig. 2-9 Schematic illustration of the preparation procedure of the Ni₃Fe/N-C sheets. Cited from Ref (Fu et al. 2017). 48

Fig. 2-10 Schematic defect structures of (a)D-NiFeZn LDHs and (e) D-NiFeAl LDHs; (b), (f) Ni 2p and (c),(g) Fe 2p XPS results of the as-synthesized LDHs (the distinct negative shift of the signals indicates modified electronic structures); and

electron paramagnetic resonance spectra of (d)NiFe, NiFeZn, and D-NiFeZn LDHs and (h) NiFe, NiFeAl, and D-NiFeAl LDHs. Cited from Ref (Xie et al. 2018).

..... 53

Fig. 2-11 (a) FESEM image (cited from Ref (Dinh et al. 2018); (b), (c) TEM image and sketch of NiFe-LDHs HMS; Cited from Ref (Zhang et al. 2016a); (d) scheme of formation of hierarchical NiFe-LDHs hollow nano prisms by a self-templated strategy, and (e), (f) FESEM and TEM images of Ni-Fe LDHs hollow prisms obtained after the hydrolysis reaction. Cited from Ref (Yu et al. 2018a).55

Fig. 2-12 Schematic illustration of the fabrication procedures of the self-standing 3D core-shell Cu@NiFe LDHs electrocatalysts. (RT represents for room temperature) Cited from Ref (Yu et al. 2017b).57

Fig. 2-13 Schematic representation of materials structures. (a) Layered hydroxides, d_1 is the interlayer distance. (b) LDHs with interlayer anions and water molecules; d_2 is the interlayer distance, $d_2 > d_1$. (c) Exfoliated LDHs monolayers dispersed in a colloidal solution. Each single layer is composed of edge-sharing octahedral MO_6 moieties (M denotes a metal element). Metal atoms: purple spheres; oxygen atoms: red spheres; interlayer anions and water molecules: grey spheres. Hydrogen atoms are omitted. Cited from Ref (Song and Hu 2014).

.....59

Fig. 2-14 (a)SEM image of NiFe LDHs nanoplate grown on a network of mildly oxidized MWCNTs. (b), (c) TEM images of NiFe-LDHs/ MWCNTs hybrid. (d) XRD spectra of NiFe-LDHs/ MWCNTs hybrid (black) and a control β -Ni(OH)₂/ MWCNTs sample (red). The lines correspond to standard XRD patterns of α -

Ni(OH) ₂ (black, JCPDS card No.38-0715) and β-Ni(OH) ₂ (red, JCPDS card No.14-0117). (e) Schematic showing the hybrid architecture and LDHs crystal structure. Cited from Ref (Gong et al. 2013).	61
Fig. 2-15 (a) Schematic illustration of the fabrication of NiFe LDHs-NS@DG nanocomposite. (b) LSV curves of different electrocatalysts in 1 M KOH solution (the inset is the overpotential required at a current density of 10 mA/cm ²), Cited from Ref (Jia et al. 2017). (c) ORR and OER LSV curves (at 1600 rpm) of Ni ₂ CoFe-LDHs+GO, Ni ₂ CoFe-LDHs, Ir/C, and Pt/C-20%. (d) Schematic of the in-situ growth of LDHs nanosheets on nitrogen doped GO (N-GO). Cited from Ref (Zhou et al. 2018).	63
Fig. 2-16 Schematic for the fabrication process of SSM-NCs/Ni(Fe)O _x H _y via acid corrosion and nickel (oxy)hydroxide deposition. Cited from Ref (Shen et al. 2018).	66
Fig. 4-1 Schematic illustration of preparing composite of Fe(OH) ₃ and carbon materials (graphene nanosheet and MWCNTs).	80
Fig. 4-2 TG curves of EG and EG-F obtained under different pH.	81
Fig. 4-3 SEM of EG-F with (a) pH=2.7, (b) pH=9 and (c) pH=11.	81
Fig. 4-4 CV curves of EG-F with (a) pH=2.7, (b) pH=9 and (c) pH=11 at 20 mV/s in 1 M KOH.	82
Fig. 4-5 SEM images of (a) EG and (b)AEG.	83
Fig. 4-6 CV curves of (a) EG, AEG and (b) EG-F, AEG-F at a scan rate of 20 mV/s in 1 M KOH, and (c) GCD curves of EG-F and AEG-F in the same electrode system at 1A/g.	85

Fig. 4-7 CV curves of (a) EG-F and (b) AEG-F in 1M KOH at a scan rate of 20mV/s. (Pt wire as counter electrode).	86
Fig. 4-8 SEM images of (a) EG-F and (b) AEG-F.	86
Fig. 4-9 CV curves of sample EG-F, EG-F-H, MWCNTs-F, MWCNTs-F-H in 1M KOH at 20 mV/s (Pt wire as counter electrode).	87
Fig. 4-10. SEM images of (a) MWCNTs-F and (b) MWCNTs-F-H.	88
Fig. 4-11 CV curves of (a) MWCNTs, MWCNTs-F, MWCNTs-F-H and (b) CV curves of MWCNTs in 1M KOH at 20 mV/s (Pt wire as counter electrode).	89
Fig. 4-12 GCD curves of MWCNTs and MWCNTs-F in 1M KOH at 1A/g (Pt wire as counter electrode).	89
Fig. 4-13 CV curves of the first cycle and the 300cycle of MWCNTs-F prepared at different sonication time 2h, 3h, 4h, 5h, 6h, 7h.	90
Fig. 4-14 CV curves of the first cycle of MWCNTs-F prepared at different sonication time 2h, 3h, 4h, 5h, 6h, 7h, 8h.	91
Fig. 4-15 The ratio of different CV characteristic of the 300th cycle to the 1st cycle in different sonication time.	92
Fig. 5-1 (a)SEM image, (b) TEM image and (c) high resolution TEM image of Fe₂O₃/MWCNTs (the inset is the corresponding SAED pattern).	95
Fig. 5-2 XRD pattern of Fe₂O₃/MWCNTs and Fe₂O₃.	96
Fig. 5-3 FT-IR spectrums of Fe₂O₃/MWCNTs and MWCNTs after Fenton reaction washed by acid.	97
Fig. 5-4 N₂-adsorption/desorption isotherms of Fe₂O₃/MWCNTs and MWCNTs.	98

Fig. 5-5 XPS spectrum of (a) Fe₂O₃/MWCNTs and high-resolution spectra of (b) Fe 2p, (c) C 1s and (d) O 1s.	99
Fig. 5-6 (a) CV curves of Fe₂O₃/MWCNTs and (b) Fe₂O₃ at 0.05 mV/s.	101
Fig. 5-7 GCD curves of (a) Fe₂O₃/MWCNTs and (b) Fe₂O₃ at 100 mA/g.	102
Fig. 5-8 Cycling performance of (a) Fe₂O₃/MWCNTs at 500mA/g (activated at first 6cycles under 100mA/g) and (b) rate capacity of Fe₂O₃/MWCNTs and Fe₂O₃ at different charge-discharge rate from 0.1C to 2C, each rate was used for 6cycles.	104
Fig. 5-9 Nyquist plots of Fe₂O₃/MWCNTs before charge-discharge and after 500 cycles charge-discharge (a) and Nyquist plots of Fe₂O₃/MWCNTs and Fe₂O₃ without charge-discharge (b).	105
Fig. 6-1 (a) SEM image of F(3-1)3, (b) TEM image of F(3-1)3 (the inset is the SAED patterns), (c) HRTEM image of F(3-1)3 with different scales and (d) EDS element mapping images of F(3-1)3.	109
Fig. 6-2 XRD patterns with different molar ratio of Ni: Fe and different total molar.	110
Fig. 6-3 N₂-adsorption/desorption isotherms of (a) F(1-1)3, (b) F(2-1)3, (c) F(3-1)1, (d) F(3-1)2, (e) F(4-1)3and (f) F(3-1)3 and raw material of MWCNTs.	112
Fig. 6-4 XPS spectrum of (a) F(3-1)3 and high-resolution spectra of (b) Ni 2p, (c) Fe 2p, (d) C 1s and (e) O 1s.	114
Fig. 6-5 (a) LSV curves of the NiFe LDHs with different molar ratio and different total molar ratios in 1M KOH at a scan rate of 5 mV/s (95% iR-correction) and the corresponding (b) Tafel plots calculated by Tafel equation.	116

Fig. 6-6 (a) Multi-step CP curve of F(3-1)3 in 1M KOH, the current density started from 10 mA/cm² and ended at 80 mA/cm² with an increment of 10 mA/cm² every 500 s without iR correction.(b) CP curve of F(3-1)3 in 1M KOH with an current density of 10 mA/cm² for 40 h without iR correction and the inset is the CP curve of F(3-1)3 collected in the first 1h. 118

Fig. 6-7 CV curves and corresponding slopes of capacitive current densities at 1.29V vs.RHE against different scan rates of samples of (a), (b) F(1-1)3, (c), (d) F(2-1)3, (e),(f) F(3-1)1, (g), (h), F(3-1)2, (j), (k) F(3-1)3and (m), (n) F(4-1)3. 121

Fig. 6-8 XPS spectra of (a) Ni 2p, (b) Fe 2p, (c) C1s and (d)O1s of product of F(3-1)3 before activation and after activation. 122

List of Tables

Table 2-1. Elemental reaction steps in OER in acidic and alkaline media. (Zhang et al. 2017a).	31
Table 3-1(I) Chemicals used in this work	68
Table 3-1(II) Chemicals used in this work	69
Table 3-1(III) Chemicals used in this work	70
Table 3-2 (I) Experimental equipment	70
Table 3-2 (II) Experimental equipment	71
Table. 6-1 S_{BET}, overpotentials at different current densities of 10, 50,100 mA/cm², Tafel slopes, C_{dl} value of materials of F(1-1)3, F(2-1)3, F(3-1)1, F(3-1)2, F(3-1)3, F(4-1)3.	113

List of Abbreviations

Rct: Resistance of charge transfer

AEG: Acid treated expandable graphite

Ag/AgCl: Silver/ Silver chloride

BET: Brunauer-Emett-Teller

CA: Chronoamperometry

CBD: Chemical bath deposition

CC: Carbon cloth

C_{dl} : Double layer capacitance

ClO_4^- : Perchlorate ion

CNF: Carbon nanoframes

CNSs: Carbon nanosprings

CP: Chronopotentiometry

CS: Chitosan

CTs: Carbon textiles

CV: Cyclic voltammetry

CVD: Chemical vapor deposition

DA: Dopamine

DFT: Density functional theory

DG: Defective graphene

DMC: Dimethyl carbonate

DPCNW: Disordered porous carbon nanowire

EC: Ethylene carbonate

ECSA: Electrochemical surface area

EDX: Energy dispersive X-ray spectroscopy

EG: Expandable graphite

EIS: Electrochemical impedance spectroscopy

EPR: Electron paramagnetic resonance

EXAFS: Extended X-ray absorption fine structure

Fe(AcAc)₃: Iron (III) acetylacetonate

FTIR: Fourier-transform infrared spectroscopy

GC: Gas chromatography

GF: Graphene foam

H₂O₂: Hydrogen peroxide

HER: Hydrogen evolution reaction

H-Fe₂O₃/CNTs: Hollow structured ferric oxide/carbon nanotubes

HMS: Hollow microspheres

IrO₂: Iridium (IV) oxide

LDHs: Layered double hydroxides

LIBs: Lithium ion batteries

LiPF₆: Lithium hexafluorophosphate

LSV: Linear sweep voltammetry

MFPF: Multifrequency phase fluorimeter

MNBI: 2-mercapto-5-nitrobenzimidazole

MWCNTs: Multi-walled carbon nanotubes

NCL: Collection efficiency

NCs: Nanocone arrays

NMP: N-methyl pyrrolidone

NPs: Nanoparticles

OER: Oxygen evolution reaction

OH·: Hydroxyl radical

OMCNW: Ordered mesoporous carbon nanowire

ORR: Oxygen reduction reaction

PAA: Poly (acrylic acid)

PAN: Polyacrylonitrile

PDDA: Poly(diallyldimethylammonium) chloride

PDS: Potential determining step

PEI: Polyethylenimine

PEMAc: Poly (ethylene-alt-maleic)

PMMA: Poly (methyl methacrylate)

PVA: Poly (vinyl alcohol)

PVDF: Polyvinylidene fluoride

PVP: Poly vinylpyrrolidone

RDS: Rate-determining step

Rf: Film resistance

rGO: Reduced graphene oxide

RHE: Reversible hydrogen electrode

RRDE: Rotating ring disk electrode

SA: Sodium alginate

SAED: Selected area electron diffraction

SDS: Sodium dodecyl sulfonate

SEI: Solid electrolyte interface

SEM: Scanning electron microscope

SS: Stainless steel

SSM: Stainless steel mesh

SWCNT: Single-walled carbon nanotube

TEM: Transmission electron microscope

TMOs: Transitional metal oxides

TOF: Turnover frequency

XANES: X-ray absorption near edge structure

XPS: X-ray photoelectron spectroscopy

XRD: X-ray diffraction

List of Nomenclature

mAh/g: Milliampere hour per gram

nm: Nano-meter

KeV: Kilo Electron-Volt

mA/g: Milliampere per gram

C: Coulomb

η : Overpotential

i_0 : exchange current density

b: Tafel slope

E: Realistic potential

E_{eq} : Equilibrium potential

E^0 : Formal potential

R: Universal gas constant

T: Absolute temperature

F: Faraday constant

C_O : Concentration of oxidized reagent

C_R : Concentration of reduced reagent

I: Current density

cm^2 : Square centi-meter

α_A : Charge transfer coefficient for anodic reaction

α_C : Charge transfer coefficient for cathodic reaction

mV/s: Millivolt per second

Δj : the difference of current densities between anodic and cathodic

Ω : Ohmic

μm : Micron

min: Minute

λ : Wavelength of beam

wt%: Weight percentage

μL : Microliter

mm: Millimeter

rpm: Revolutions per minute

h: Hour

$^{\circ}\text{C}$: Degree Celsius

mg: Milligram

V: Volt

m^2/g : Square meters per gram

Chapter 1 Introduction

1.1 Research Background

Due to the environmental pollution, global warming, and the urgent need for energy, looking for clean and sustainable energy to alter fossil fuel has become a biggest challenge (Gür (2018)). However, the renewable energy sources such as solar, wind, geothermal heat were usually limited by time and location. Hence, electrochemical EESC are considered as effective ways to meet the need of global energy demand by storing and transportation (Hector D. Abruna 2008, Bruce Dunn 2011).

LIBs as one type of EESC devices commonly has high energy density, high voltage range, low-self discharge. since it was initial commercialization in 1991 by Sony company, it has attracted tremendous attention, especially focused on materials (Huang et al. 2018). However, graphite as commercial anode materials in LIBs has a relative low capacity of 372 mAh/g. Therefore, a great of work have been devoted to develop an effective anode material with high capacity, long-cycling life (Mishra et al. 2018). Transition metal oxides (TMOs) are usually used as anode materials in LIBs, because of their abundance, low cost, and high theoretical capacities. However, the low conductivity and significant volume change during the process of charge-discharge of TMOs limit their practical application in the field of LIBs. To resolve these issues, many useful approaches such as nanosizing, combing with other conductive materials, hierarchical structure designing have been widely studied in the past decades (Roy and Srivastava 2015, Srivastava et al. 2015, Zhang et al. 2018a).

OER as a positive electrode charge reaction in fuel cells and an anode reaction in water splitting have widely application. However, OER is a four electron-proton coupled

reaction, high energy is needed to break the kinetic barrier to promote the reaction. RuO₂ and IrO₂ as the typical OER electrocatalysts are too expensive to use in OER. Oppositely, TMOs or transition metal hydroxides especially layered double hydroxides (LDHs) (Ni, Fe, Co) (Han et al. 2017, Mahala, Sharma and Basu 2018, Zhou et al. 2017, Wu et al. 2018c) have been verified to have excellent electrocatalytic performance for OER. However, the similar problem like TMOs used in LIBs, the low conductivity and unstable structure also hamper their wide application. Hence, combining with conductive substrate, hierarchical structure designing, doping with other atoms, introducing defects are the effective way to enhance their electrocatalytic performance for OER (Wang, Dastafkan and Zhao 2018b, Lu et al. 2017).

Carbon materials, such as graphene, MWCNTs etc. are common substrate used to enhance the conductivity of TMOs. The advantages for carbon materials combined with TMOs are (i) enhance the conductivity of TMOs or LDHs, and further increase the kinetic of reaction, (ii) impede the aggregation of TMOs or LDHs in the reaction process and hence, stabilize the structure change and enhance the stability of reaction, (iii) the synergetic effect between each other promote the uniform disperse of TMOs or LDHs and increase active surface area (Zhou et al. 2011, Du et al. 2014).

The common methods used to synthesize composites of carbon and TMOs or LDHs were categorized into two approaches: post immobilization and in situ binding (Khan et al. 2015). Post immobilization is a method that carbon materials directly mixed with the pre-synthesized TMOs or LDHs, is was combined by surface functionalized groups which added before mixing. However, in this process, the particles of TMOs or LDHs may aggregate together on the surface of carbon which cause low electrochemical

property. In situ binding method is a type method that TMOs or LDHs particles can directly grow on the carbon substrate. And this method with well dispersed TMOs or LDHs product, uniform size structure has gradually replaced post immobilization. because materials prepared by post immobilization exist weak interaction between carbon materials and TMOs or LDHs and the non-uniform dispersion of TMOs or LDHs particles on the carbon substrate caused inferior properties when these materials used as anode materials in LIBs and electrocatalyst catalysts in OER. In-situ binding method such as hydrothermal reaction, solvothermal reaction, chemical bath deposition (CBD), carbon substrates often need to be oxidized by strong acid treatment or plasma treatment. For example, graphene often was oxidized to form graphene oxides by modified Hummers method, and MWCNTs were oxidized by acid treatment in concentrated nitric acid and sulfuric acid, in this process, large amount of acid was generated and the reaction is fierce. Therefore, methods for oxidizing were time consumable, environmentally unfriendly(M. Li 2014). Hence, looking for a green and scalable method for synthesizing composites of carbon and TMOs or LDHs used as anode in LIBs or electrocatalyst in OER is important.

1.2 Aim and Objectives

The aim of this work is to prepare composites of $\text{Fe}_2\text{O}_3/\text{MWCNTs}$ and NiFe LDHs/MWCNTs by a simple way. because most methods used to prepare composite of $\text{Fe}_2\text{O}_3/\text{MWCNTs}$ and NiFe LDHs/MWCNTs include two steps: firstly, MWCNTs are oxidized by strong acid to remove impurities and introduce oxygen functional groups, and then the oxidized MWCNTs react with iron salt to form composites of $\text{Fe}_2\text{O}_3/\text{MWCNTs}$ and NiFe LDHs/MWCNTs. In this work, Fenton reaction is applied

to introduce oxygen functional groups and simultaneously one of Fenton reagents, ferrous sulphate used as iron precursor can form iron hydroxide and form bimetal hydroxides with nickel ions. Sonication was used to assist the reaction to accelerate the reaction.

Fenton reaction usually used to oxidize organic contaminant to inorganic ions, carbon dioxide, water (Enric Brillas 2004). hydroxyl radical ($\text{HO}\cdot$) generated by Fenton reagent-Ferrous salt and hydrogen peroxide ($\text{Fe}^{2+}\text{-H}_2\text{O}_2$), were used to oxidize MWCNTs. The results show some oxygen-containing functional groups such as COOH , OH , and quinone generated in this process (Li et al. 2005). Fenton reaction with the assistant of sonication or photo to fabricate graphene quantum dots (GQDs) were also reported (Parimal Routh 2013, Li et al. 2005, Hao Bai 2014), in this process, graphene oxides with underlying C-C bonding is ruptured into small pieces which was called GQDs, the sonication or ultraviolet irradiation used to accelerate the reaction. It is indicated that the Fenton reaction could oxidize graphene oxide However, no one reported the preparation of composites of carbon materials (e.g., Carbon nanotube, graphene nanosheets,) and metal oxide by this method.

In this work, one simple method was used to fabricate composites of $\text{Fe}_2\text{O}_3/\text{MWCNTs}$ and $\text{NiFe LDHs}/\text{MWCNTs}$. In the process of reaction, based on mechanism mentioned in Li's work (Li et al. 2005), hydroxyl radical generated in the process of Fenton reaction was recognized as one of the most active oxidants, and can introduce some OH , COOH and quinone oxygen containing groups on the plane and edge of carbon materials, and hence, after oxidizing, $\text{Fe}_2\text{O}_3/\text{MWCNTs}$ or NiFe LDHs can be formed by electrostatic interaction between positive metal ions and negative oxygen groups.

1.3 Structure of the Thesis

The structure and content of thesis are briefly introduced in the following:

Chapter 1: briefly introduce the background of this research, aim and objectives, and the structure of this thesis.

Chapter2: introduce a review of research on LIBs and OER, including the preparation method for synthesizing composite of carbon materials with metal oxide or metal hydroxides, the progress in LIBs and OER using composites as anode materials or electrocatalysts, the problem now still need be solved.

Chapter 3 the chemicals and equipment are listed in detail, the detailed preparation procedure and characterization method are introduced.

Chapter 4 compare different carbon materials combined with $\text{Fe}(\text{OH})_3$ by Fenton reaction, and compare the as-synthesized product by SEM images and electrochemical properties.

Chapter 5 introduce the characterization and electrochemical measurements of composite of $\text{Fe}_2\text{O}_3/\text{MWCNTs}$ material used as anode materials in LIBs.

Chapter 6 introduce the characterization and electrochemical test of composites of NiFe LDHs/MWCNTs material used as electrocatalysts in OER.

Chapter 7 conclusion for this work and recommendation for future work are concluded.

Chapter 2 Literature Review

2.1 Basic Introduction

Due to a great deal of consumption on fossil fuels, Energy crisis and environmental pollution have become critical and hampered the progress of economy and society. Hence, it is urgent to development of sustainable and cleanable energy, like wind, solar energy, hydro etc.. However, these energies are usually limited by time and position. Hence, looking for a useful device to store and convert energy is necessary. EECS have attracted tremendous attention. The convenient portable energy-storage devices, such as fuel cells, batteries, supercapacitors have been widely used in mobile phones, laptops, electric vehicles *etc.* (Gür 2018).

LIBs with high energy density, good cycling stability, high voltage range has been recognized as the most promising battery system. It was widely used in various field from portable electronic devices to transportation-electric vehicles, solar energy, etc. and in the section 2.2, LIBs is introduced in details, especially on the anode materials composed of metal oxide and carbon materials.

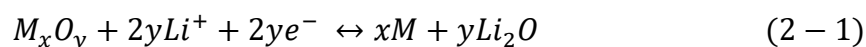
OER as a half reaction in metal-air battery or water splitting for hydrogen generation have been attracted tremendous attention. However, the sluggish kinetic of OER has limited their practical application. Hence, electrocatalyst such as RuO₂ have been used to overcome the energy barrier and increase the reaction. But the scarcity of noble metal oxide promotes the study on TMOs or LDHs. The study can help accelerate the reaction rate in metal-air battery or water splitting and further promote the development

of cleanable energy. It is introduced in section 2.3 focused on the electrocatalyst composed of carbon materials and metal hydroxides.

2.2 Overview for LIBs

2.2.1 Introduction

LIBs usually were composed by five main parts: electrode (cathode and anode), electrolyte, separator, current collector and shell (Qi et al. 2017). Based on the reaction, LIBs store charges by three different mechanisms (Xueying Li 2018): (i) intercalation-deintercalation, such as graphite, which has layered structure and could make Li ions reversibly intercalate into the lattice without ruining their structure, (ii) alloying-dealloying, such as Si, which can form alloy with Li metal, (iii) conversion reaction, which could store charge by electrochemical reactions with transitional metal oxides (TMOs) (See Eq. 2-1 and Fig. 2-1). And the reduction and oxidation reaction process involve multi-electron transfer, and hence TMOs have high theoretical specific capacitance (usually >600 mAh/g) which are 2 or 3 times than that of graphene (372 mAh/g).



In the reaction, M represents metal, Li ions reduces metal oxide to metal.

However, the application of TMOs as anode in LIBs was limited by their low conductivity, high volume change in the reaction process. Hence, to solve these issues, numerous studies have been done. One of the effective way is combining with conductive materials, such as carbon nanotubes (CNTs), graphene, carbon fibers, etc.,

carbon materials not only provide a high electric conductive substrate for TMOs, but also offer a volume buffer for the volume change of TMOs (Srivastava et al. 2015). Among these TMOs materials, Due to the abundance on earth, multiple valence states, low cost and easy preparation of Fe_2O_3 , Fe_2O_3 has been investigated by lots of research groups. In this review, Fe_2O_3 with different carbon materials as anode materials in LIBs will be discussed in following sections (Keppeler et al. 2016, Jun Liu 2016, Ma et al. 2018).

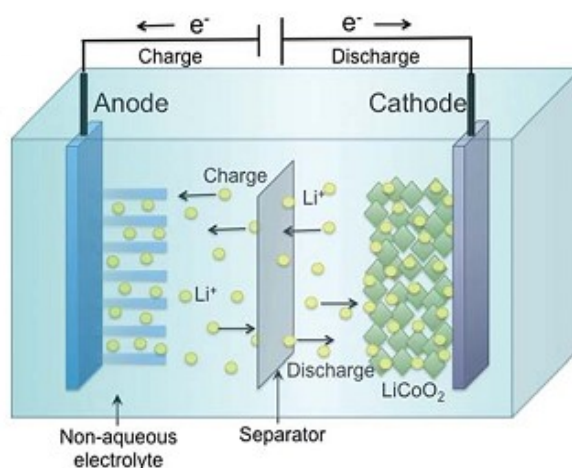


Fig. 2-1 Schematic diagram of the lithium intercalation-de-intercalation reaction mechanism in a rechargeable lithium-ion battery containing solid electrodes and a liquid electrolyte.

Cited from ref (Qi et al. 2017).

2.2.2 Fe_2O_3 with Carbon Materials

Carbon materials commonly include CNTs, graphene, carbon fibers, carbon cloths, based on their structures, they are generally divided into 1dimension (1D) structure, 2D

structure, 3D structure. Composites of different carbon materials with different structure and Fe₂O₃ used in LIBs were summarized in the following section.

2.2.2.1 1D carbon materials with Fe₂O₃

CNTs with one-dimensional tubular and porous structure, has high electrical conductivity (5×10^5 S/m), good strength and high surface area. It was divided into single walled CNT (SWCNT) and MWCNTs. Due to the high reported reversible lithium ion capacities of CNTs-based materials which were higher than 1000 mAh/g based on the experimental factors (Brian J. Landi 2009). It was believed that CNTs is the most promising material for hybrids of Fe₂O₃/CNTs in LIBs. There are some advantages for CNTs as substrates in Fe₂O₃/CNTs composites: (i) the conductive matrix could enhance the conductivity and improves reaction kinetics to increase rate capability, (ii) the porous structure ensures uniform dispersion of Fe₂O₃ which further buffers the volume expansion/extraction of Fe₂O₃ in the process of lithium insertion/extraction and improves the cycling performance. Hence, enormous efforts have been devoted to prepare composites of Fe₂O₃/CNTs and investigate their properties as anode materials in LIBs (Zainab Karam 2018, Min Hong 2019).

A flexible binder-free and current collector free Fe₂O₃/ SWCNT was prepared by oxidizing assembled Fe/SWCNT membrane (See Fig. 2-2 a, b, c) (Zhou et al. 2012). Firstly, Fe/SWCNT was synthesized by floating catalyst Chemical Vapor Deposition (CVD) at 1100°C with sulfur and CH₄ as promoter and carbon sources, respectively. Interestingly, for obtaining a paper-like film, a stainless steel (SS) wire mesh was used as substrate for the growth of SWCNT, and it transported to the outlet in the process of

preparing SWCNT and was considered as Fe sources. This material shows a high reversible capacity of 1243 mAh/g at a current density of 50 mA/g and an outstanding cycling stability over 90cycles at 500 mA/g. It is ascribed that the high conductive SWCNT network promotes the fast electron transition and impedes the volume change of Fe₂O₃ nanoparticles. Cao *et al.* also synthesized Fe₂O₃/SWCNT macro film by a simple heat treatment approach (Zeyuan Cao 2013). It was believed that SWCNT macro-film with high conductivity and flexibility could enhance the electrochemical kinetics and the thickness of film which compare to the characteristic Li diffusion length of 300-500nm facilitates the diffusion of Li ions. Hence, Fe₂O₃/SWCNT film has a high specific capacity of 1000 mAh/g and excellent cycling stability over 100 cycles. SWCNT as a substrate for composites of Fe₂O₃/SWCNT films has been demonstrated that the flexible conductive network is beneficial for composite of Fe₂O₃/SWCNT using as an anode for LIBs. MWCNTs also show excellent electric property and they could provide an inner electron pathway for electron transport due to their inner wall which is not easily destroyed in the reaction process. Yang et al. prepared Fe₂O₃ nanoparticles (NPs)/MWCNTs films by two steps (See Fig. 2-2d) (Yang et al. 2015). Firstly, a CVD gas flow reaction was applied to prepare Fe NPs/MWCNTs films with ferrocene and ethanol as catalyst and carbon precursor, respectively, and then an annealing process in air under temperature of 500°C was applied to convert Fe NPs/MWCNTs films into Fe₂O₃ NPs/MWCNTs films. The as-synthesized material performs an initial reversible capacity of 985.8 mAh/g at a current density of 30 mA/g and an excellent cycling performance with a reversible capacity of 375.5 mAh/g at 3 A/g after 800cycles. The high columbic efficiency implies rapid

lithium ion and electron transportation due to the porous structure of MWCNTs. The small size of Fe_2O_3 nanoparticles (5-10 nm) could increase the contact area between the electrode and electrolyte and further decrease the distance of Li diffusion.

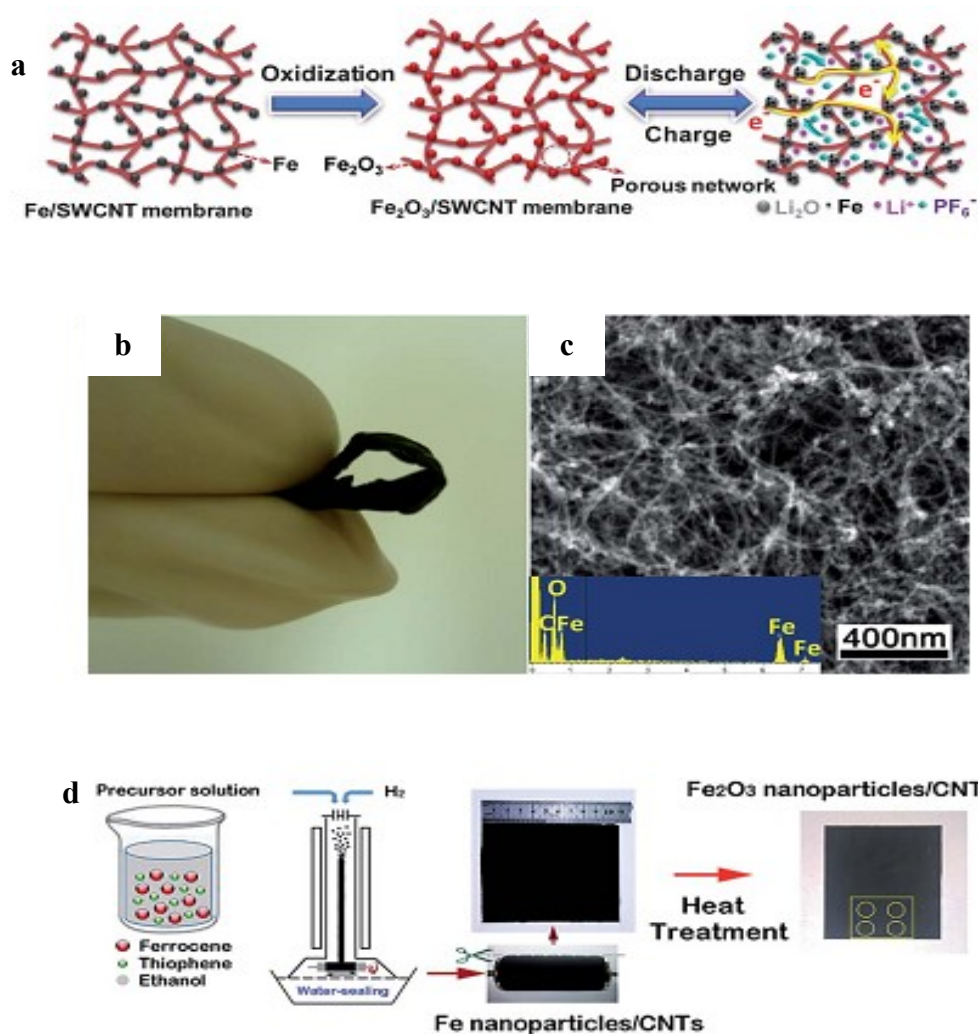


Fig. 2-2 (a) Schematic of the synthesis of $\text{Fe}_2\text{O}_3/\text{SWCNT}$ membrane, (b) photograph of the flexible membrane obtained after oxidation; (c) SEM images of the $\text{Fe}_2\text{O}_3/\text{SWCNT}$ membrane and corresponding EDS spectrum (inset unit: KeV) Cited from Ref (Zhou et al. 2012) (d) Preparation procedures of Fe_2O_3 nanoparticles/MWCNTs composite film. Cited from Ref (Yang et al. 2015).

Except nanoparticles, Fe_2O_3 with other various morphologies combined with CNTs were also prepared by different methods. Such as nanobelt, nanorod *etc.* Wu *et al.* synthesized bundle-like Fe_2O_3 (width:10 nm) nanobelts on MWCNTs by a homogeneous precipitation and thermal annealing method (Wu et al. 2014). The as-prepared composite shows an initial charge and reversible capacity of 847.5 mAh/g at a current density of 100 mA/g and displays good cycling performance with a reversible capacity of 865.9 mAh/g at 100 mA/g. The high electrochemical performance is due to the MWCNTs network structure which offers an effective electron pathway and buffers the volume change of Fe_2O_3 during the lithium insertion/extraction. A hollow nanorod Fe_2O_3 with inner voids grafted on MWCNTs (H- Fe_2O_3 /MWCNTs) were fabricated by Park and coworkers (See Fig. 2-3a) (Park et al. 2018). In this work, microsphere and porous structure of MWCNTs were made by ultrasonic spray pyrolysis, and then a bottom up deposition of $\beta\text{-FeOOH}$ followed with oxidation was used to obtain hollow Fe_2O_3 nanorods / MWCNTs microspheres. During the process of thermal treatment, $\beta\text{-FeOOH}$ were transformed into hollow Fe_2O_3 nanorods by dihydroxylation and shrinkage, hence, Fe_2O_3 has a unique porous structure. The porous hollow structure enhances the accessibility of electrolyte and the microsphere structure provides a conductive pathway for electron in the reaction. Hence, the prepared material displays a high discharge capacity of 1307 mAh/g at 1 A/g after 300 cycles with a capacity retention of 84% and delivers high reversible discharge capacity of 1159, 1073, 989, 944, 907, 828, and 703 mAh/g at current densities of 0.5, 1.0, 3.0, 5.0, 7.0, 10.0 and 15.0 mA/g (See Fig. 2-3b, c). The excellent rate capability is due to the introduction of

voids on the Fe_2O_3 nanorod during the process of heat treatment, which buffer the serious volume change and also shorten the distance of ion and electron transportation.

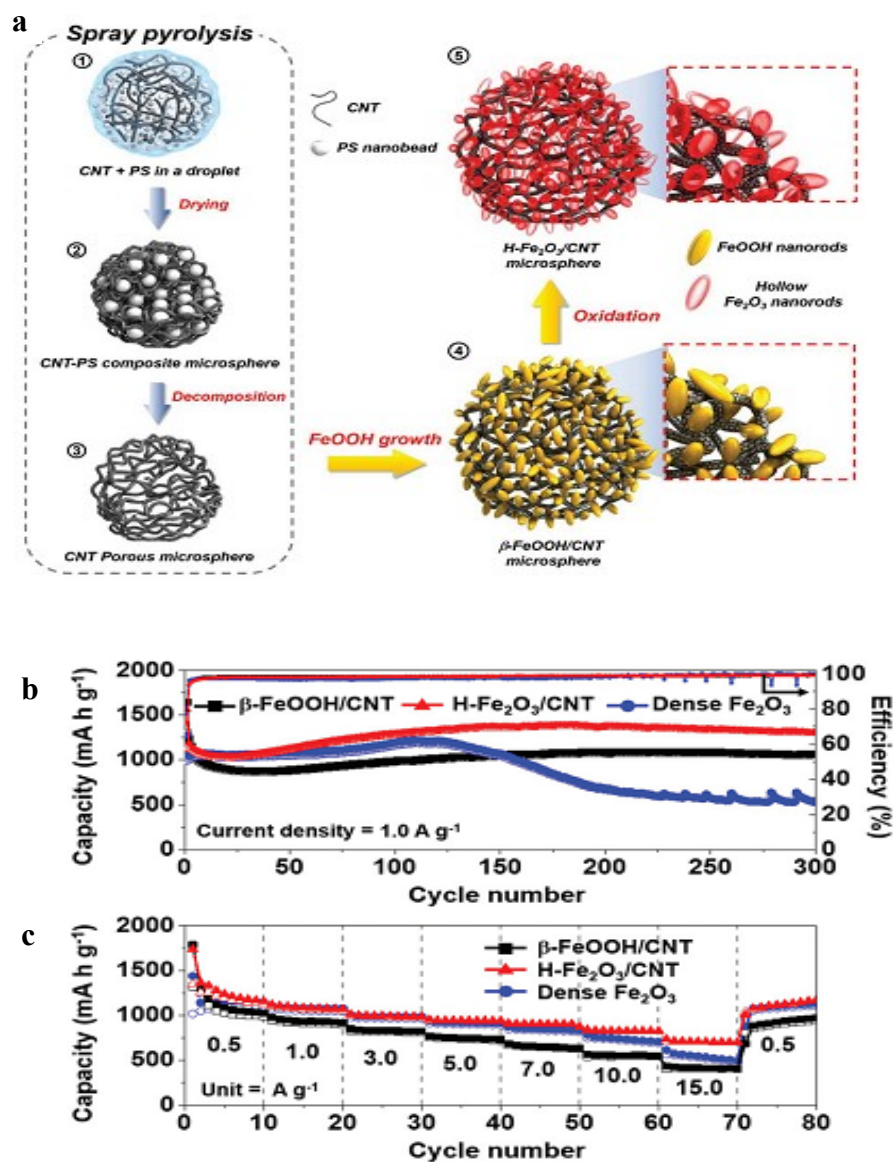


Fig. 2-3 (a) Formation mechanism of H- Fe_2O_3 /MWCNTs microspheres, Electrochemical properties of β -FeOOH/ MWCNTs microspheres, H- Fe_2O_3 / MWCNTs microspheres and dense Fe_2O_3 nanorods: (b) cycling performance along with columbic efficiencies at 1A/g; (c) rate capability at various current densities. Cited from Ref (Park, Park and Kang 2018).

Apart from directly combining with CNTs, ternary composites by combining carbon layer, graphene and reduced graphene oxide (rGO) *etc.* with MWCNTs and Fe₂O₃ are also investigated (Jiang et al. 2018, Liu et al. 2015b). For instance, Wang *et al.* prepared a carbon coated Fe₂O₃ hollow nano-horns on MWCNTs by a bottom up assemble method (Wang et al. 2012). MWCNTs was firstly oxidized by acidic reflux to introduce carboxylic and hydroxyl functional groups for surface nucleation. And then β-FeOOH which was formed by the hydrolysis of FeCl₃ anchored on the oxidized MWCNTs, and followed with transformation of β-FeOOH into α-Fe₂O₃ by thermal dihydroxylation and lattice shrinkage. Finally, an amorphous carbon layer was coated on the surface of MWCNTs / Fe₂O₃ by hydrothermal carbonization of glucose (See Fig. 2-4a, b). The as-prepared material shows a high reversible capacity of 800 mAh/g at a current density of 500 mA/g after 100 cycles and exhibits excellent rate capability, the capacities are maintained around 420-500 mAh/g even at a high rate of 1000-3000 mA/g. It is attributed to the unique three layer structure: (i) the inner porous conductive MWCNTs network increases electron transfer and enhances kinetics of electrochemical reaction and further improves rate capability, (ii) the hollow structure of α-Fe₂O₃ nano-horns in the middle layer of composite and the small size increase the surface area between electrode and electrolyte, (iii) the outer carbon layer buffer the volume change of Fe₂O₃ and prevent Fe₂O₃ from falling down on the electrode.

The properties of carbon used for coating on the Fe₂O₃ are thin with few nanometers and flexible. Graphene or rGO also have similar properties, and thus were applied as a constituent part. Liu *et al.* synthesized a 3D rGO/MWCNTs/ Fe₂O₃ ternary hybrids via a simple one-step urea-assisted hydrothermal method (Jinlong Liu 2013). The material

exhibits initial discharge and charge capacities of 1692 and 1322 mAh/g at a current density of 100 mA/g, respectively and shows excellent cycling performance with a reversible discharge capacity of 1118 mAh/g at 100 mA/g after 50 cycles. It is believed that 3D porous hierarchical structure of as-prepared ternary composite enhances the conductivity and increases the surface area and shortens the Li diffusion. The electrochemical properties of anode material are related not only to the intrinsic nature of material, but also to the structure, morphology, hence graphene foam (GF) as another conductive substrate with hierarchical structure are also attracted much attention of researchers. Chen *et al.* reported a 3D porous lightweight α -Fe₂O₃ nanorods/MWCNTs-GF composite (Chen et al. 2014). MWCNTs were directly grew on the surface of micropore of GF to further increase the surface area of GF. And MWCNTs-GF hybrid material was used as a substrate for Fe₂O₃ growing by a bottom-up method. The direct bottom-up growth method enhances the rigid contact and thus ensures the structural stability of material during the repeated lithium insertion/extraction (See Fig. 2-4c-h)). This design is beneficial for the electrochemical performance of as-synthesized material. Hence, it has good columbic efficiency and performs high rate capability of 900 mAh/g at 200 mA/g to 450 mAh/g at 3000 mA/g and excellent cycling performance with a reversible capacity about 1000 mAh/g at 200 mA/g up to 300 cycles.

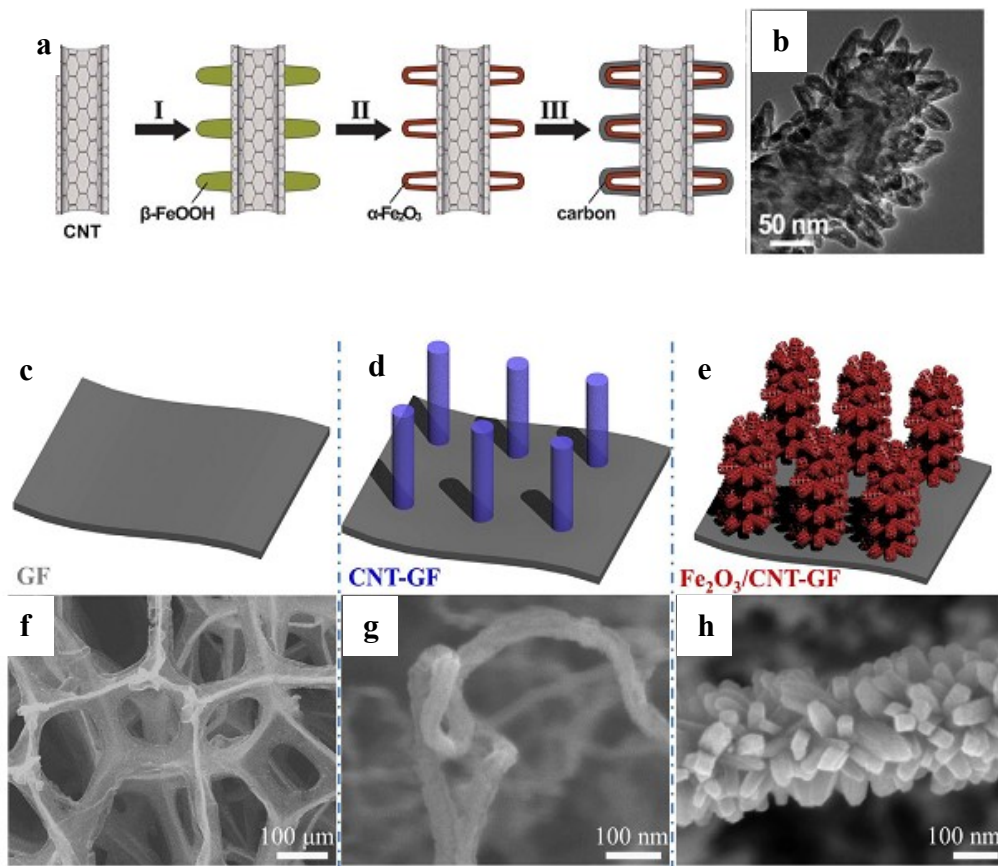


Fig. 2-4 (a) Schematic illustration of preparation of carbon coated α - Fe_2O_3 hollow nano-horns on MWCNTs backbones; (b) TEM images of carbon coated MWCNTs@ Fe_2O_3 hierarchical structures; Cited from Ref (Wang et al. 2012) (c-e) schematic of α - Fe_2O_3 nanorods/MWCNTs-GF fabrication stage: (c) GF, (d) MWCNTs-GF, (e) Fe_2O_3 /MWCNTs-GF, (f-h)the corresponding SEM images. Cited from Ref (Chen et al. 2014).

In addition to CNTs, carbon fibers also have 1D structure and usually are used as carbon matrices in the composites of carbon materials and Fe_2O_3 . Electrospinning as the main preparation method for carbon fibers is also the dominant method for fabricating Fe_2O_3 /carbon fiber composites (Yuta Kobayashi 2018, Xueyan Huang 2018). For example, a quasi 1D Fe_2O_3 /carbon nanofibers hybrid was synthesized by electrospinning method (Xiang Zhang 2014). In this paper, polyacrylonitrile (PAN) as

carbon sources and iron (III) acetylacetonate ($\text{Fe}(\text{AcAc})_3$) as Fe_2O_3 precursor, after electrospinning and post heat treatment, Fe_2O_3 -C nanofibers were obtained. This material used as anode material in LIBs exhibits a good cycling performance with a reversible capacity of 820 mAh/g at 0.2 C after 100 cycles, and the capacity is 262 mAh/g even at high current density of 5 C. The outstanding electrochemical performance is due to the unique fiber structure which improves the conductivity and hampers the pulverization and aggregation of Fe_2O_3 in the process of reaction. Although carbon fiber as a conductive matrix has performed its merits on enhancing the electrochemical performance of Fe_2O_3 as anode in LIBs, a great deal of efforts still needs to be done to further improve the cycling performance and rate capability of Fe_2O_3 . For instance, a porous carbon nanofibers was prepared by electrospinning with PAN as carbon sources and poly (methyl methacrylate) (PMMA) as a sacrificial pore-forming agent, and then γ - Fe_2O_3 was in-situ embedded into the carbon matrix (Yujie Chen 2018). The composite of γ - Fe_2O_3 /C nanofiber with optimal weight ratio 1.5:1:1 of γ - Fe_2O_3 , PAN and PMMA displays a superior cycling performance with a high discharge capacity of 1088 mAh/g at 0.2 C after 300 cycles and excellent rate capability and long-life span when the capacity reach to 600 mAh/g (600 cycles) and 400 mAh/g (1000 cycles) scanned at 0.5 C and 2 C respectively. The excellent electrochemical performance is attributed to the porous carbon matrix and well dispersed γ - Fe_2O_3 . The porosity in carbon matrix accommodates the volume change of γ - Fe_2O_3 in the process of lithium insertion/extraction and carbon matrix provides fast electron pathway and increases the kinetics of reaction. In addition to electrospinning method, hydrothermal method is also used to synthesize Fe_2O_3 /carbon fiber composite with direct carbon fiber

sources. Wu investigated properties of Fe₂O₃ nanorods on carbon fibers as anode for LIBs (Chunyu Wu 2014). The composite was fabricated with carbon fiber by a simple hydrothermal method with poly vinylpyrrolidone (PVP) as dispersant. The synergistic effect of Fe₂O₃ nanorods and carbon fibers facilitates cyclic stability and initial discharge capacity since carbon fibers offers an electronic network for high electron transportation and also buffers the volume fluctuation, 1D Fe₂O₃ nanorod increases the surface area between electrode active materials and electrolyte.

Carbon nanosprings (CNSs) as 1D carbon material is also studied as a matrix for Fe₂O₃/CNSs. Shao et al. (Shao et al. 2011) prepared α - Fe₂O₃/CNSs by a precipitation and post heat treatment method. The optimal α - Fe₂O₃/CNSs with weight ratio 1:4 delivers high charge capacity of 527.6 mAh/g at 0.2 C with 96.9% capacity retention after 50 cycles, and capacity keeps around 343.3 mAh/g at the rate of 5 C. The uniformly dispersed Fe₂O₃ and conductive carbon network play a crucial role on improving cyclic stability and rate capability.

2.2.2.2 2D carbon materials with Fe₂O₃

2D carbon materials especially graphene and its derivative like graphene oxide (GO), rGO have played a vital role in the hybrids of Fe₂O₃/ graphene (GO, rGO). Since graphene was mechanically exfoliated by Novoselov in 2004 (K. S. Novoselov 2004), a number of articles about graphene and its derivative have been published . Ideal graphene is composed of a monolayer of Sp² carbon atoms with a hexagonal structure. Graphene has a large theoretical specific surface area (2620 m²/g), brilliant thermal conductivity (5000 W/mK) and good Young's modulus (1.0 TPa) (Rao et al. 2009).

Graphene, due to the lack of functional groups, is usually oxidized by Hummer method, modified Hummer method to introduce oxygen groups for easily reacting with other metal salts to form metal oxide/GO composites (Georgakilas et al. 2012). After oxidization, the oxidized graphene oxide (GO) is reduced to rGO with few oxygen functional groups. It is believed that the high surface area of graphene and its derivative (rGO) could offer an ideal matrix to combine with Fe₂O₃ due to the following reasons: (i) graphene and rGO could enhance the conductivity of Fe₂O₃ and further increases reaction kinetics and reduces the resistance of composites, and hence improves rate capability, (ii) the 2D flexible layer could strain the volume change of Fe₂O₃ during the charge-discharge and as a result of increasing the reversible capacity and cycling performance (Chen et al. 2012, Bai et al. 2012).

Hydrothermal method is the common method for preparing Fe₂O₃/rGO composite. Liu *et al.* fabricated α -Fe₂O₃ nanoplates/rGO by a simple hydrothermal method with water and glycerol as hydrothermal solvents (Liu et al. 2014). In this work, GO was well dispersed into the solution and adsorbed Fe²⁺ ions onto their surface, after hydrothermal reaction, the formed FeO(OH) was transformed into α -Fe₂O₃ nanoplates with the help of glycerol. GO was simultaneously reduced to rGO by Fe²⁺ and glycerol. The composite exhibits an outstanding rate performance with different reversible capacities of 1149, 1041, 986.5 and 899.4 mAh/g at different current densities of 0.1, 0.5, 1 and 2 C. and an excellent cycling performance with a capacity of 896mAh/g still remained after 200 cycles at 5 C. The high electrochemical performance is ascribed to the unique nanoplate structure and the synergistic effect. The nanoplate structure with (001) planes could decrease the way of Li ion diffusion and facilitate the kinetics of reaction. Li et

al. reported that α -Fe₂O₃ nanoaggregates/rGO with core-shell structure was synthesized by a hydrothermal method (Li et al. 2015). And herein, α -Fe₂O₃ nanoaggregates with a high surface area of 47.8 m²/g and a small crystalline size of 10 nm are wrapped by rGO to form a core-shell structure. The small size, high surface area and core-shell structure are the main reasons for composite of α -Fe₂O₃ nanoaggregates/rGO with high electrochemical performance. It delivers an enhanced specific capacity of 1787.27 mAh/g after 90 cycles at 0.1 A/g. Interestingly, different structures, such as nanoplate, nanoaggregate etc. have different electrochemical performances when using as anode in LIBs. and the different morphology of Fe₂O₃ with graphene oxide also show various properties in LIBs. 1D porous α - Fe₂O₃ nanorod arrays on the both side of rGO was reported by Kong via a scalable seed-assisted hydrothermal method (Kong et al. 2016). Although lots of efforts have been done on investigating the relationship between structure, morphology of Fe₂O₃/RGO and their electrochemical performance as anode materials in LIBs , the relationship is still a challenge and need further deep research with the help of advanced in-situ testing instruments to check the evolution of morphology of composites in the process of reaction, especially in the charge-discharge process (Hao et al. 2016).

Besides the common hydrothermal method, other preparation approaches also have been studied. For example, Xiao and coworkers utilized direct self-assembly route to prepare Fe₂O₃/rGO nanocomposite (Xiao et al. 2015). And with a high iron oxide mass loading of 63%, the composite performs a high reversible specific capacity of 600 mAh/g at 0.1 A/g and a superior rate capability of 180 mAh/g at 10 A/g for 300 cycles. Cai also used an electrostatic self-assembly method to synthesize a core-shell structure

of Fe₂O₃ fiber/rGO nanocomposite (Cai et al. 2017a). Inspiring by a corn-like structure, the Fe₂O₃ nanofiber firstly was fabricated by an electrospinning route, and the negatively charged rGO was wrapped on the positively charged Fe₂O₃ nanofiber to form composite of Fe₂O₃/rGO. The unique nanofiber structure with high surface area and unlocked channels are in favor of rapid diffusion of Li ion, hence, the composite delivers a high initial capacity of 1085.2 mAh/g at 0.1 A/g and has high cycling performance with 407.8 2 mAh/g at 5 A/g after 1500 cycles.

Zhu and coworkers synthesized α -Fe₂O₃/rGO nanocomposite via a facile and rapid microwave approach with Fe(OH)₃ as precursor of α -Fe₂O₃ and hydrazine hydrate as a reductant (Zhu et al. 2015). Unlike hydrothermal method which is time-consuming, microwave method is rapid and simple. The Fe(OH)₃ sol was converted into α -Fe₂O₃ nanoparticles anchored uniformly on rGO surface. The as-synthesized material shows a high reversible specific capacity of 650 mAh/g at 1.0 A/g after 50 cycles and the rate capability is superior with different specific capacities of 720, 670, 610, 520 and 400 mAh/g at different current densities of 0.5, 1.0, 2.0, 5.0 and 10.0 A/g. The superior electrochemical properties are due to the nanosized α -Fe₂O₃ nanoparticles with 30-50 nm diameter which could shorten the Li ion diffusion length and minimize the volume change of Fe₂O₃ during the process of charge-discharge.

Kirkendall effect caused by the differences in diffusion directions and speed between various ions in the preparing process was used to manufacture a core-shell structure of γ -Fe₂O₃/graphene at room temperature (Hu et al. 2015). The as-prepared core-shell nano-hollow γ -Fe₂O₃/graphene demonstrates an excellent rate capability with high

reversible capacity of 1095, 833, 551 mAh/g at the current densities of 0.1 C, 1 C and 2 C. It is recognized that the core-shell structure with high surface area and protective graphene shell is beneficial for the brilliant electrochemical performance.

Xu and coworkers applied a simple and eco-friendly way to prepare γ -Fe₂O₃/rGO composite (Xu et al. 2018a). In this route, iron metal was used to reduce GO under acidic conditions and in the meantime, Fe²⁺ ions and electrons were released from iron metal and then interacted with oxygen functional groups on GO by electrostatic reaction. The composite delivers a stable capacity of 830 mAh/g after 300 cycles at 500 mA/g, and it also shows good rate performance with average reversible discharge capacities of 650, 520, 460, 320, 250, and 200 mAh/g at various current rates of 0.1, 0.5, 1, 2, 5, 10 and 15 A/g. Because of the generation of Fe₂O₃ and rGO happened at the same time which ensure the uniform dispersion and stabilization of Fe₂O₃ in the rGO layers, and avoid the aggregation of Fe₂O₃.

As a 2D carbon material, carbon cloth (CC) is also used as carbon substrate for combining with Fe₂O₃. For instance, Li *et al.* prepared pomegranate-like Fe₂O₃@C nanoparticles on CC by dip-coating method followed with hydrothermal treatment (Li et al. 2018c). The chelate compound formed by sodium alginate (SA) and Fe³⁺ was converted into Fe₂O₃@C by hydrothermal treatment. The formed hierarchical pomegranate-like structure of Fe₂O₃@C with primary particles (118 nm) and secondary nanoparticles (13.7 nm) on CC is beneficial for improving the electrochemical performance. Due to the pomegranate-like structure which not only increases the accessible surface area for electrolyte but also buffers the volume change during the

charge-discharge process, and the CC provides a conductive matrix for further hampering the structural cracks. Hence, the as-synthesized composite exhibits a remarkable cycling performance with a high reversible discharge capacity of 1091 mAh/g after 100 cycles at 0.2 A/g. The rate performance is good when the current density is not beyond 0.5 A/g with discharge capacities of 1008 and 943 mAh/g at current densities of 0.1 and 0.2 A/g. In the meantime, Xiong *et al.* also used flexible carbon textiles (CTs) as carbon matrix to prepare Fe₂O₃@CTs via controllable CBD route (See Fig. 2-5a) (Xiong et al. 2018). The mass loading and crystal size of α -Fe₂O₃ could be controlled by adjusting the reaction temperature without the use of auxiliary substances. The experiment demonstrates that large mass loading and crystal size of α -Fe₂O₃ cause a large damage of the CTs which decrease the electronic interconnections between α -Fe₂O₃ nanocrystals and CTs, while the optimized mass loading of α -Fe₂O₃ on Fe₂O₃@CTs-90 and Fe₂O₃@CTs-100(90, 100 mean the temperature of CBD) minimize the damage of the CTs and improve the electronic interactions (See Fig. 2-5b). And especially the optimized Fe₂O₃@CTs-100 displays a high initial discharge capacity of 1159 mAh/g and charge capacity of 1032 mAh/g, but the charge/discharge capacity of Fe₂O₃@CTs under other three temperature of 70-90 are not good as that of Fe₂O₃@CTs-100. The enhanced initial capacity of Fe₂O₃@CTs-100 is ascribed to the formation of α -Fe₂O₃ with smaller crystal size and 3D interconnected porous structures which enlarge the active surface area between electrolyte and electrode, and also reduce diffusion distance of Li ions and electrons.

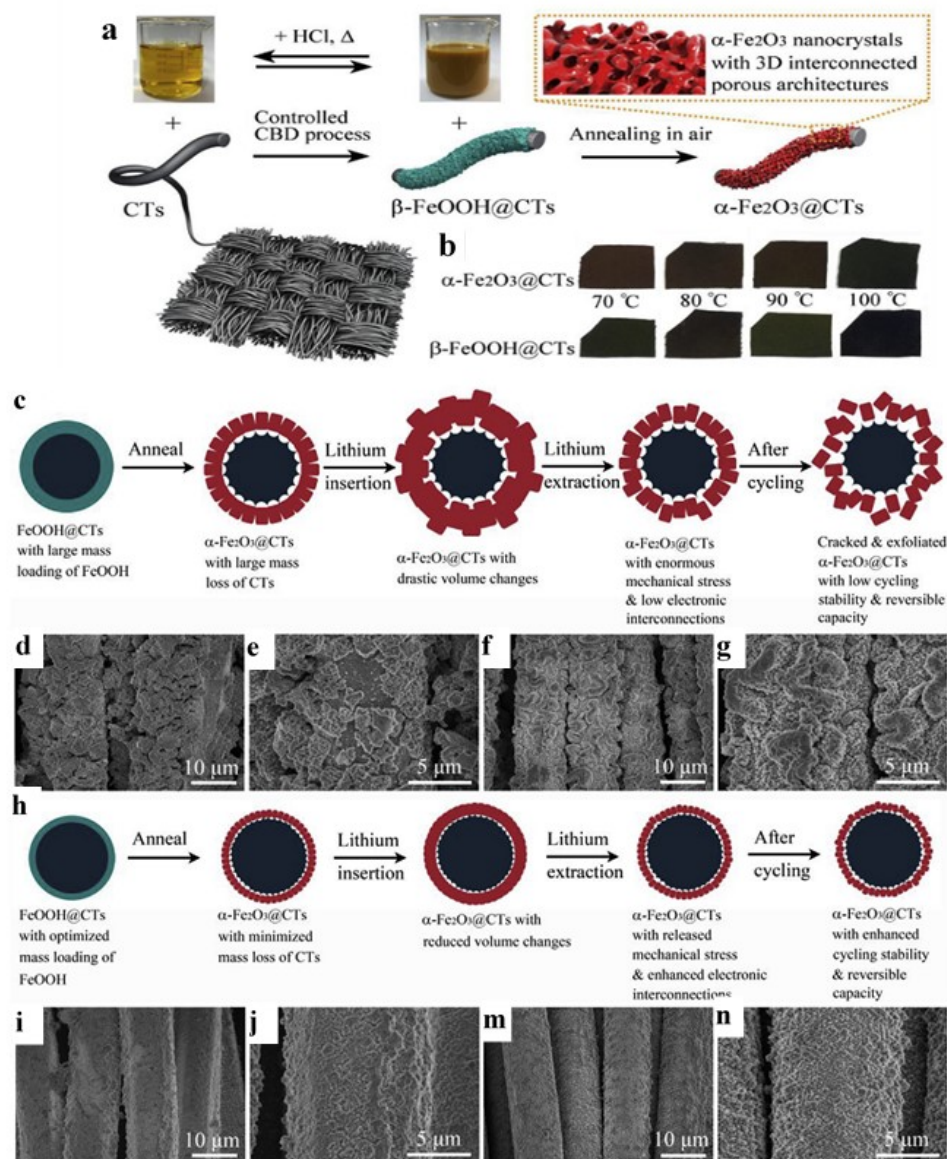


Fig. 2-5 (a) Schematic of recyclable process for scalable controlled assembly of α - Fe_2O_3 nanocrystals on flexible CTs; (b) patterns of $\text{FeOOH}@CTs$ and $\text{Fe}_2\text{O}_3@CTs$ obtained at different CBD temperature. (c) schematic of crack and exfoliation of α - Fe_2O_3 with large mass loading on the CTs; SEM images of (d, e) $\text{Fe}_2\text{O}_3@CTs$ -70 and (f, g) α - $\text{Fe}_2\text{O}_3 @CTs$ -80 after 100 cycles at 0.5C in the voltage range from 0.01 to 3.0 V; (h) schematic of the enhanced stability and electronic interconnections of ultrathin α - Fe_2O_3 nanocrystals onto the CTs; SEM images of (i, j) $\text{Fe}_2\text{O}_3 @CTs$ -90 and (m, n) $\text{Fe}_2\text{O}_3@CTs$ -100 after 100. cited from Ref (Xiong et al. 2018).

2.2.2.3 3D and other carbon materials with Fe₂O₃

Except the common carbon material, such as CNTs, GO, carbon aerogel (CA) as 3D carbon are also used as carbon matrix to provide a porous conductive structure. Coating carbon layer on Fe₂O₃ is also an useful method to protect Fe₂O₃ from stacking during the charge-discharge process (Liu et al. 2018c).

CA as a carbonaceous material was used to prepare composite of CA and Fe₂O₃ by a sol-gel process (Yan et al. 2017). Firstly, CA was obtained from resorcinol-formaldehyde with a thermal process, and then it was simply added into Fe(NO₃)₃ solution followed with an annealing process. The result shows that composite of Fe₂O₃/CA-60 show a high capacity of 818 mAh/g at 100 mA/g. it also exhibits a remarkable capacity retention with 617 mAh/g after 100th cycles and still remain a high capacity of 500 mAh/g when scanned at high current density of 800 mA/g.

Carbon coating as a useful strategy usually was applied to prevent the volume expansion of Fe₂O₃ in the process of reaction in LIBs. Ma et al. prepared γ -Fe₂O₃/carbon composite by a hydrothermal method followed with CVD in an acetylene atmosphere (Ma, Ji and Lee 2011). After hydrothermal process, disk-like Fe₂O₃ was obtained. The research indicates that different CVD treatment time influence the morphology of Fe₂O₃ and thickness of carbon layer. When the time is 5 min, a nanocarbon (thickness: 2-3 nm) coated porous γ -Fe₂O₃ microparticles was generated and it shows an optimized electrochemical performance. While the time is 3 or 8 min, uncoated γ -Fe₂O₃ and C/Fe₃O₄ (the thickness of carbon layer: 6-8 nm) were obtained, respectively. The optimal γ -Fe₂O₃/C demonstrates a high cycling performance with a

relative high capacity of 900 mAh/g after 40 cycles at 100 mA/g. Cheng et al. synthesized pseudo-cubic α -Fe₂O₃/C nanocomposites by in situ carbonization of surfactant in Ar atmosphere with oleic acid capped α -Fe₂O₃ nanoparticles as precursor (Cheng et al. 2011). The thickness of thin carbon layer is around 1-2 nm, the composite shows an outstanding cycling performance with a reversible capacity of 688 mAh/g after 50 cycles at 0.2 C. In the above-mentioned method, Fe₂O₃ was prepared firstly and then coated by carbon layer by carbonization or CVD method. Xu *et al.* prepared nanoporous Fe₂O₃@C composite by a one-pot solvothermal method (Xu et al. 2015). In this method, iron salt and glucose as precursors were mixed at the same time, and after solvothermal treatment, annealing process at 600 °C under inert atmosphere was applied to make carbon layer graphitized. Compared to bare nano porous Fe₂O₃ without carbon coating and commercial Fe₂O₃ nanoparticles, it is indicated that an inward expansion happened for Fe₂O₃@C during the cycling process while bare nano porous Fe₂O₃ nanoparticles undergo both inward and outward expansion and commercial Fe₂O₃ nanoparticles only expand to outside. And the reason is that the thin carbon layer (6 nm) buffers the outward expansion, and the porous structure of Fe₂O₃ provides voids which can buffer the volume expansion. Hence, Fe₂O₃@C delivers a high discharge capacity of 1195 mAh/g with a high coulombic efficiency of 70% at the first two cycles, the composite shows remarkable cycling performance with a reversible capacity of 767 mAh/g after 100 cycles at 500 mA/g and good rate capability with different capacities of 940, 776, 715, 545 at the current densities of 0.2, 0.5, 1, 2 A/g. The excellent electrochemical test results are traced to the porous structure of Fe₂O₃ which facilitates the Li insertion and extraction and against the volume change, the thin carbon layer

hampers the outward expansion and make solid electrolyte interface (SEI) film more stable in the reaction process.

In addition to hydrothermal method, sol-gel method, template method (Lim, Sun and Suh 2013, Li et al. 2014), self-assembly method (Yan et al. 2017), and spray pyrolysis method (Chou et al. 2010) have also been applied to prepare Fe₂O₃@C composites. Hu *et al.* synthesized ordered mesoporous carbon nanowire (OMCNW)/ Fe₂O₃ by a soft-hard dual template method (Hu et al. 2016). In this method, three types of OMCs which were named as FDU-15, CMK-8, and OMCNW were prepared with disordered porous carbon nanowire (DPCNW) by soft, hard and soft-hard dual template approaches, respectively. The electrochemical measurements indicate that OMCNW/Fe₂O₃ has excellent cycling performance with a stable capacity of 774 mAh/g after 1200 cycles at a current density of 0.5 A/g.

2.2.3 Conclusion

Due to low cost, earth abundance, environment-friendly, Fe₂O₃ has been used as anode materials for LIBs. To solve the issues of low conductivity, easy cracking during lithiation and de-lithiation of Fe₂O₃, combining with conductive materials such as carbon materials, conductive polymers, metal materials have become an effective approach, especially carbon materials because it has different structures which could stabilize the structure of Fe₂O₃, and impede the aggregation of Fe₂O₃ in the process of charge-discharge and high conductivity which could enhance the electron transportation, increase the rate capability. However, some barriers are still on the way

of achieving composites with high cycling performance and rate capability. Hence, (i) looking for low-cost, scalable preparation method for fabricating Fe_2O_3 @composites should be further studied, (ii) the relationship between the morphology/structure and electrochemical properties are also needed be investigated with advanced techniques in further, (iii) the effect of crystalline or amorphous structure of Fe_2O_3 on the electrochemical performance as an anode should be investigated.

2.3 Overview for OER

2.3.1 Introduction

The fast development of advanced technologies, especially in energy field caused large consume in natural energy, such as coal, natural gas, and polluted environment seriously. Hence, searching for sustainable energy conversion and storage system is one of the most important factors which limited the long-term development of society. Electrocatalysts, usually used in water electrolysis, fuel cell and metal-air batteries have attracted tremendous attention due to their electrocatalytic function in the above field. because the half reaction of oxygen reduction reaction (ORR), OER, in the fuel cell or water electrolysis are four-electron process. HER as the half reaction is just a two-electron reaction. Therefore, a higher overpotential is needed when OER or ORR happened compared with that in HER (see Fig. 2-6).

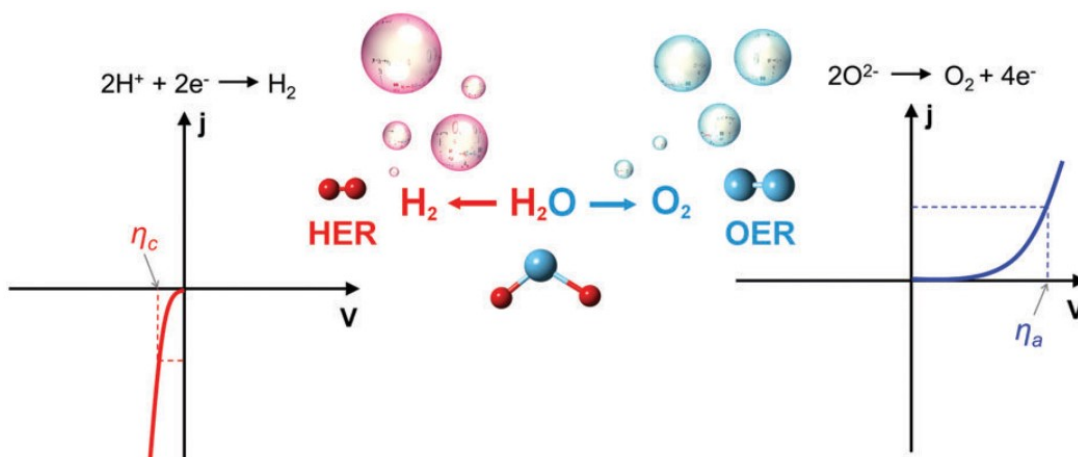


Fig. 2-6 Polarization curves for HER (left) and OER (right). The η_c and η_a are the overpotentials for cathode and anode at the same current (j), respectively. Cited from Ref (Suen et al. 2017).

OER, as an essential half reaction in the water electrolysis or metal air batteries, has been widely studied in the past few decades. RuO_2 and IrO_2 , which have excellent OER catalytic ability in a large pH arrange, are considered as benchmark electrocatalysts for OER. However, due to their high cost and unstable conditions which could easily be oxidized, some carbon material, transition metal elements or their derivatives are investigated to meet the current requirement in electrocatalysis, like carbon materials, TMOs, metal hydroxides. In Zhang's work (Zhang et al. 2017b), pure MWCNTs wrapped by electrochemically inert polymers (i.e. poly (vinyl acetate)) with polar oxygen functional groups $-\text{COOH}$, $-\text{OH}$ and $-\text{O}-$ shows high OER activity. Experimental and computational studies expose that the synergistic effect of intrinsic topological defects in CNTs as active centres and polar oxygen groups in the polymer chains as a 'kinetics accelerator' successfully boost the OER activity of metal free MWCNTs. To the metal hydroxides, LDHs are the common materials used as OER

catalysts. For instance, NiFe LDHs hollow microspheres were fabricated by one-step in situ growth method with SiO₂ as sacrificial template (Zhang, 2016). And the special hierarchical hollow structure discloses the active sites and increases the surface area which result in superior OER electrocatalytic performance.

2.3.2 Mechanism and Electrocatalytic Kinetic of OER

2.3.2.1 Mechanism of OER

In the oxygen evolution reaction, it involves four-electron-proton transfer and hence high overpotential is needed to overcome the energy barrier. It is commonly believed that the intermediate MOH and MO exist in the first step, however, to the subsequent step, two viewpoints about the intermediate and reaction are proposed, as shown in Fig. 2-7, one approach is that O₂ is directly generated by combination of 2MO (the green line), another is the decomposition of MOOH intermediate to O₂ (the red one).

In alkaline solution, hydroxide ions were adsorbed and reacted on the active sites of catalysts to form OH*, O*, OOH* and finally formed O₂ illustrated by red line in Fig. 2-7 (Fabbri et al. 2014). The blue line represents OER in acidic solution, the intermediates are same with that in alkaline solution except for the other products, like H* and electron (see Table.2-1 and Fig. 2-7). Based on the theoretical calculation, it was commonly believed that the decisive step is constrained by the slowest kinetic step, and this step is defined as the rate-determining step (RDS). However, potential determining step (PDS), based on the step with maximum change of Gibbs free chemisorption energy of adsorbed intermediates, has replaced the central position of RDS, because PDS could emphasize more the thermochemical aspects of the OER potential.

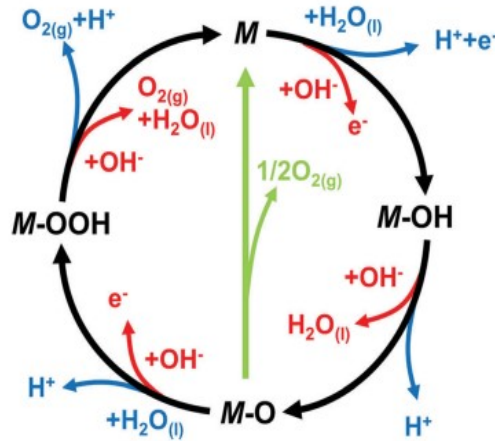


Fig. 2-7 The OER mechanism for acid (blue line) and alkaline (red line) conditions. The black line indicates that the oxygen evolution involves the formation of a peroxide (M-OOH) intermediate (black line) while another route for direct reaction of two adjacent oxo (M-O) intermediates (green) to produce oxygen is possible as well. Cited from Ref (Suen et al. 2017)

Table 2-1. Elemental reaction steps in OER in acidic and alkaline media. (Zhang et al. 2017a).

Acid	Alkaline
$H_2O(l) + * \rightarrow OH^* + (H^* + e^-)$	$OH^- + * \rightarrow OH^* + e^-$
$OH^* \rightarrow O^* + (H^* + e^-)$	$OH^* + OH^- \rightarrow O^* + H_2O(l) + e^-$
$O^* + H_2O(l) \rightarrow OOH^* + (H^* + e^-)$	$O^* + OH^- \rightarrow OOH^* + e^-$
$OOH^* \rightarrow * + O_2(g) + (H^* + e^-)$	$OOH^* + OH^- \rightarrow * + O_2(g) + H_2O(l) + e^-$

In this table, (l) and (g) represent for liquid and gas phases, and * stands for active sites of catalyst, and O*, OH*, and OOH* are adsorbed intermediates.

2.3.2.2 Evaluation parameters of OER

The electrocatalytic performance of an electrocatalyst is usually evaluated by some basic parameters which include overpotential (η), exchange current density (i_0) Tafel slope (b), Faradic efficiency, and electrochemical surface area (ECSA), *etc.* These parameters not only measure the performance of electrocatalyst, but also provide insightful information related to the mechanism of OER. Hence, a brief introduction about these concepts is necessary.

2.3.2.2.1 Overpotential (η)

In physical chemistry, the potential used to drive the happen of reaction is usually same with the potential of the reaction in equilibrium under the ideal conditions. However, an energy barrier needed to be overcome by using higher potential under realistic condition. The difference between the realistic potential (E) and equilibrium potential (E_{eq}) is defined as overpotential (η), which is expressed in Eq. 2-2 and 2-3)

$$E = E^{0'} + \frac{RT}{nF} \ln \frac{C_O}{C_R} \quad 2 - 2$$

$$\eta = E - E_{eq} \quad 2 - 3$$

In the equation 2-2, E is the applied potential and the real potential, $E^{0'}$ represents the formal potential of the whole reaction. R is the universal gas constant and T is absolute temperature. n represents the number of transferred electrons in the reaction and F is the Faraday constant. C_O and C_R mean the concentrations of the oxidized and reduced reagents, respectively. In the electrocatalytic reaction, η is the most common evaluation criterion. For OER, η (OER) = $E_{RHE} - 1.23$ V (RHE means reversible hydrogen electrode),.

In McCrory's work (Charles C. L. McCrory^{*†‡} 2015), η usually was achieved at the desired current density of 10 mA/cm² per geometric area as the benchmark. However, a serious problem about IR-compensation is still exist. The overpotential in most publications was corrected with 95% IR compensation, and only few articles show uncorrected overpotential followed the corrected potential (Anantharaj et al. 2018). If the catalyst is used as a part in water splitting, it is obviously to know, no IR compensation can be used, hence, an uncorrected overpotential is necessary to test. For IR compensation, three ambiguities are emphasized in Anantharaj's review (Anantharaj et al. 2018). Firstly, the resistance for IR compensation, compensated IR was usually thought to be solution resistance (R_s) in traditional three electrode cell which is often neglected in two electrodes. What is more, two factors such as ionic strength of the electrolyte and the distance between the reference and counter electrode, influence the magnitude of R_s . For the ionic strength of electrolyte, the common electrolyte frequently used is 1M H₂SO₄ or 1M KOH which provides high ionic conductivity. Hence, the distance between the reference and counter electrode are the main influence factor needed to be considered. Because the separation distance between reference and counter electrode influences the R_s value which subsequently causes iR drop. To solve this problem, it was found that Luggin capillary configuration is a useful tool to increase the distance between the reference and counter electrode and as a result of decreasing the magnitude of R_s . Although this specialized configuration effectively reduces R_s , R_s are still affected by other factors like various hetero-junctions. Hence, uncompensated resistance (R_u) now take the place of R_s . In the equation (2-4), iR drop compensated overpotential is calculated for an electrocatalyst in OER and HER electrocatalysis.

$$iR \text{ drop free } \eta_{\text{OER}} = E_{\text{RHE}} - 1.23\text{V} - E_{iR} \quad (2 - 4)$$

Based on the above equation, if 100% iR drop compensation was used for an electrocatalyst, the R_s still exists in a two-electrode system. Therefore, it must be emphasized that iR drop uncompensated overpotential is more meaningful than the iR drop compensated overpotential at a defined current density. Secondly, the percentage of iR drop compensation and its influence on overpotential at a defined current density are also important. There are two methods used to attain the iR drop compensation. One is achieved by the electrochemical workstation itself and another way is to use equation (2-5) to calculate.

$$\eta \text{ (iR (\%) drop compensation)} = E - IR_u \quad (2 - 5)$$

In this equation, E is the overpotential versus RHE at a defined current density without iR compensation, I is the defined current density, and R_u represents the observed resistance. It is obviously known that the overpotential after iR drop compensation is smaller than the overpotential without compensation, and the overpotential will decrease if increasing the percentage of iR drop compensation. Hence, description the percentage of iR drop compensation is more accurate and persuasive to readers to evaluate the electrocatalytic properties of electrocatalysts. However, when the R_u is higher than 6 ohms and current density is higher than 100 mA/cm², the iR compensated overpotential cannot truly response the overpotential in realistic cell, especially in a two-electrode system. Therefore, choosing suitable substrate electrode with high conductivity and low intrinsic resistance which reduce the R_u value to lower than 6 ohms is necessary. For instances, carbon fibre, Ni foam and foil, and Cu foam and foil

are commonly used as substrate. If the current density is higher than 100 mA/cm², the possible unacceptable linear sweep voltammetry (LSV) curves maybe achieved (Sengeni Anantharaj 2017). Therefore, an appropriate percentage of iR drop compensation should be chosen and citing the percentage in article is important for a research. Thirdly, two methods mentioned above are used to get iR drop compensation overpotential, but the consequences obtained by two methods have some distinction, The difference between the one obtained from electrochemical workstation and the one obtained from manual iR drop compensation is ascribed that the overall current density will increase followed with the reduction of overpotential at a defined current density when using electrochemical workstation to obtain iR drop compensation. The choice about which one is the suitable method using for achieving iR drop compensation overpotential is still not resolved. Hence, the method used for iR compensation should be emphasized for readers to ensure the accuracy of data in the articles.

2.3.2.2.2 Tafel slope and exchange current density

Tafel analysis is applied to determine kinetics of the electrocatalyst in the OER. Tafel equation from the well-known Butler-Volmer equation is listed below:

$$I = I_0 \left[\exp\left(\frac{\alpha_A n F}{RT} \times \eta\right) - \exp\left(-\frac{\alpha_C n F}{RT} \times \eta\right) \right] \quad (2 - 6)$$

In equation 2-6, I and I₀ represent current and exchange current, respectively, and α_A and α_C denote the charge transfer coefficients for anodic and cathodic reactions, respectively, n is the number of electron transferred, F means the Faraday constant which equals to 96485 C, R is the ideal gas constant when T is the absolute temperature, η expresses the overpotential. In the OER, there is an anodic polarization which could

neglect the cathodic contribution, hence the equation 2-6 can be simply changed into equation 2-7, as given below:

$$I = I_0 \left[\exp \left(\frac{\alpha n F}{RT} \times \eta \right) \right] \quad (2 - 7)$$

When Eq. (2-7) was translated into the logarithm form as shown in Eq. (2-8), it can be obviously noted that current density (i_0) and Tafel slope (b) can be calculated accordingly and Tafel slope (b) can be expressed as Eq. (2-9)

$$\log(i) = \log(i_0) + \frac{\eta}{b} \quad (2 - 8)$$

$$b = \frac{2.303RT}{\alpha F} \quad (2 - 9)$$

From Eq.2-8, it could be understood when the slope (b) is smaller, the current increases faster, the value of slope (b) is influenced by the transfer coefficient (α). Hence, Tafel slope (b) is usually used to provide insightful information for OER and predict the electrocatalysis properties of electrocatalyst. Exchange current density (i_0) commonly reflects the intrinsic bonding/charge transferring interactions between the electrocatalyst and reactant. It is achieved by extrapolating the Tafel plot to the interception at the reversible potential of electrocatalytic study (for OER, it is 1.23 V vs. RHE).

In Ananthraj's review (Anantharaj et al. 2018), it is summarized that Tafel slope is received by three methods, including electrochemical techniques of voltammetry, chronoamperometry (CA)/chronopotentiometry (CP) and electrochemical impedance spectroscopy (EIS). Among them, voltammetry is the common method which was widely used to obtain Tafel slope in the published articles. However, one point needed

to be noticed that the sweep scan rate should be no more than 5 mV/s, because if the scan rate over 5 mV/s, a high capacitive current generates and causes a high external potential drop. To decrease the influence of current generated by faradic and capacitive, Burke and co-workers averaged the forward and reverse sweeps ahead of plotting on the semi-log plots and extracting the Tafel slope (Burke et al. 2015). Due to the demerits of voltammetry-derived Tafel plots, a steady-state polarization curves should be obtained by static electrochemical techniques, such as amperometry or potentiometry, because enough time was provided for a steady state and no capacitance was generated in this method. Thus, the Tafel slope obtained by this technique could reflect the intrinsic catalytic activity of the catalyst. Compared to the voltammetry method, it seems that static electrochemical method is accurate when getting rid of the influence of capacitance current, however, other resistances such as intrinsic resistance of catalyst, the resistance of interface between electrode and catalyst, solution resistance, etc., are still exist. To further solve this issue, EIS is used to determine the Tafel slope. In Heron and co-workers' work (Heron Vrubel 2013), EIS was proposed and performed at different overpotentials with intervals in the activity range of catalyst. Two points should be emphasized in Tafel analysis process, one is the potential selected during Tafel analysis should be larger than 120mV compared to the onset overpotential of OER, another is that two or three decades should be included within the linear portion where the slope is measured.

2.3.2.2.3 ECSA

It is commonly believed that high ECSA implies high catalytic activity of electrocatalyst. Hence, ECSA is also an important factor used to reflect the activity of

electrocatalyst. Based on the Eq. 2-10, ECSA is calculated from the double layer capacitance (C_{dl}), and two methods used for receiving C_{dl} are cyclic voltammetry and impedance spectroscopy (Stevens et al. 2016).

$$ECSA = \frac{C_{dl}}{2} \quad 2 - 10$$

When using the former method to obtain C_{dl} , a series of cyclic voltammetry (CV) cycles at different scan rates in a range of potential without faradic reaction happened were scanned by electrochemical workstation, the difference of anodic and cathodic current densities ($\Delta j = j_a - j_c$) measured at a potential point were used to estimate the ECSA. The slope of the plot of Δj versus scan rates is C_{dl} , as shown in Eq. 2-11.

$$C_{dl} = \frac{dQ}{dE} = \frac{i_{dl}}{v} \quad 2 - 11$$

Because the C_{dl} is calculated in an appropriate region without faradic reaction happened, many catalysts which are not conductive until they are oxidized are not suitable for using CV method to obtain C_{dl} . Therefore, EIS is applied to obtain C_{dl} in where C_{dl} can be extracted from EIS with an equivalent circuit (Boettcher 2015).

Although C_{dl} was used to determine electrocatalytic activity of electrocatalyst, it only can be used to compare a series of materials with similar chemical and physical properties in one study and cannot be used to compare different material in various studies. It will be more accurate to combine EIS and C_{dl} method together to measure ECSA than that obtained by just using one single method.

2.3.2.2.4 Faradic efficiency

Faradic efficiency was used to measure the efficiency of the power of electron participated in an electrochemical cell. It can be calculated as the ratio of the number of electrons generated from experimentally collected amount of O₂ to the number of electrons observed theoretically in the process of charge transfer. There are two common methods used to calculate Faradic efficiency based on the above definition. The first one is drainage method in which the evolved gas was collected and translated into the moles by Avogadro's law, and the theoretical moles calculated by the Faraday's second law (Jia et al. 2017). In most papers, the faradaic efficiency is nearing 100%. The second method is gas chromatography (GC), GC is applied to test the amount of experimentally generated O₂. Compared to the first method, GC could test the O₂ in regular time intervals while long time should be needed to collect enough O₂ to fill the cylindrical measuring jar in the first method. When using the first method, a large deviation easily caused during the process of collecting gas (Dinh et al. 2018). Except above two methods, fluorescence spectroscopy is also applied to test the amount of O₂. For example, Song *et al.* used ocean optics multifrequency phase fluorimeter (MFPPF-100) with a FOXY-OR 125 probe to test the generated O₂ (Song and Hu 2014). In these three methods, H-shape cell are necessary to separate the anodic and cathodic generated gases, and it is clearly observed that the volume ratio of oxygen and hydrogen is 1: 2.

Rotating ring disk electrode (RRDE) is a special electrode which could be used to test and reduce the oxygen when oxygen generated in the disk glassy carbon electrode at a lower scan rate of 5 mV/s, the Pt ring could test and reduce the oxygen to water at a constant potential. Hence, RRDE is also a technique applied to obtain FE. Part of the generated oxygen is tested and reduced by the Pt ring in the testing process, a parameter

of collection efficiency (N_{CL}) should be noticed before starting the test (Jin Suntivich 2011).

2.3.2.2.5 EIS

EIS is a useful electrochemical analytic tool for investigating the kinetics of electrocatalytic reaction. EIS was usually used with other techniques to test the properties of electrocatalyst or the reaction happened on the interface of electrode and electrolyte. Chakthranont and co-workers (Chakthranont et al. 2017) applied EIS and in situ X-ray adsorption spectroscopy to reveal the resistance between catalyst film and Au substrate and the high number of electrochemically active metal sites. Choosing a common and suitable circuit to fit for EIS should be considered. Three parameters were discussed in this article: R_f , R_{ct} , C_{dl} , these three parameters reflect the ohmic loss in the catalyst layer, the rate of charge transfer and the electrochemical surface area, respectively. Swierk and co-workers (Swierk et al. 2015) used EIS and activation energy measurements to find that the $Fe_xNi_{1-x}OOH$ are most active and the pure $NiOOH$ and $FeOOH$ catalyst have higher faradic resistance and activation energy than that of $Fe_xNi_{1-x}OOH$. Hence, EIS was usually accompanied with other techniques to test the kinetic of electrocatalyst and mechanism of OER under in-situ condition.

2.3.3 The Design Strategies

2.3.3.1 Strategies for improving OER

Based on the mechanism of OER for catalyst, it is widely believed that the intrinsic activity of an electrocatalyst is decided by the adsorption or desorption of some intermediates with a volcano-shape plot related with the activity and surface adsorbing

property. Hence, to improve the electrocatalytic activity, changing the surface adsorption is a directly route. In Zhang’s review (Tang, Wang and Zhang 2018), they attempted to summarize and suggest multiscale principles from the aspect of electronic structure, hierarchical morphology, and electrode interface. It is obviously known that electronic structure directly influences the intrinsic activity of individual active sites. To change electronic structure, heteroatoms (N, S, P, B) doping or defects are considered as effective ways for enhancing the electrocatalytic activity of metal free carbon materials, and the doping of cations (e.g., Ni, Fe, Co) or anions (e.g., O, S, OH) is also a promising method for high electrochemical performance of transition metal materials, TMOs or hydroxides. From the multiscale principles, hierarchical morphology and electrode interface are also two aspects that researchers should concern. Lu *et al.* reviewed the first-row transition metal for OER (Lu et al. 2017). It is summarized that three parts, Gibbs free energy, electronic conductivity and electrocatalytic active surface, play an important role on the whole overpotential used for OER. Hence, to achieve a lower overpotential, the consideration and design strategies should around these tree points. It is pointed out that the total overpotential equals to the sum of the overpotentials caused by the above three points, as shown in Eq. 2-12

$$\eta_{tot} = E_{app} - E^0 = \eta_{\Delta G} + \eta_{con} + \eta_{surf} \quad 2 - 12$$

In this equation, η_{tot} represents the total overpotential for the catalyst at a given current density. E_{app} is the applied potential. E^0 signifies the thermodynamic equilibrium potential for water oxidation. $\eta_{\Delta G}$ is the overpotential caused by Gibbs energy and it is

influenced by the intrinsic electronic structure of catalyst. η_{con} corresponds to the potential drop between the active sites and the external circuit, which is related to the resistance between catalyst and electrode substrate. η_{surf} stands for amount of surface active sites of the catalyst which is commonly related to the surface area of the catalyst. The similar view on enhancing OER properties are also reviewed in Wang's work (Wang et al. 2018b). And in the following section, different material used for OER catalyst was summarized and discussed from the above aspects: (i) tuning the electronic structure for improving intrinsic properties, (ii) increasing surface area or active sites, (iii) enhancing the conductivity by combing conductive supporting materials, (iv) constructing hierarchical porous structure.

2.3.4 Materials Used in OER

It is widely known that IrO_2 and RuO_2 are the commonly electrocatalysts used in OER. They are considered as the benchmark of the catalytic activity due to the high performance especially in acidic solution which is more stable than TMOs or LDHs. Although the excellent performance on electrocatalytic activity of OER, the prohibitive cost of noble metal oxides hampers its practical application when largely using in industry. Hence, looking for alternatives such as carbon materials, transition metal, TMOs or LDHs have attracted tremendous attention in recent years. The following sections focus on these materials and it should be emphasized that the pH of solution discussed in the following section is alkaline, because transition metal, TMOs or LDHs are unstable in acid solution.

2.3.4.1 Carbon material

Carbon materials (graphene, CNTs, carbon fibre) usually exist poor electrocatalytic properties. However, when doping with other atoms or non-covalently adsorbing certain polymer, the electrocatalytic activity of carbon materials have obvious improvement. When doping with some atoms (i.e. N, O, S), the adjacent carbon materials are positive charged due to intra-molecular charge transfer. The surface electronic structure is tuned by incorporating with other atoms and further the ability of adsorption to the reactants (OH^- or O_2) or intermediates generated in the process of OER is modified which finally determine the rate of OER based on the mechanism of OER. Zhang believed that the multiple atoms-doping carbon electrocatalyst has better electrocatalytic performance than single heteroatom-doping carbon materials (Zhang et al. 2017a). For the single atom doped-carbon materials, N is the common atom for doping with carbon materials used in the OER. As discussed above, N could change the electronic structure of carbon layer by adjusting the electron density near the N atom, and this phenomenon facilitates the performance of electrocatalysts in OER. Li reported that a free-standing N-doped carbon nanotubes (NCNTs) arrays was synthesized by a directed growth method (Li et al. 2017). And NCNTs shows a high activity and stability with an overpotential of 265 mV at 10 mA/cm^2 and a low Tafel plot of 19.5 mV/dec, due to the unique cactus-like hierarchical porous structure and lower charge transfer resistance. As a high surface area monolithic, 3D N-doped porous carbon cloth was fabricated by Balogun and co-workers (Balogun et al. 2016). This catalyst has a low overpotential of 360 mV at a current density of 10 mA/cm^2 . The outstanding electrocatalytic performance is ascribed that N-doping, high surface area and 3D porous structure improve the electrocatalytic activity of the catalyst in OER.

Except N atom, S and P are also used as doping atoms to improve the electrocatalytic properties of carbon materials. They usually connected with N to form multiple heteroatoms-doping carbon material. Qu studied the N, S-codoping mesoporous carbon nanosheets prepared by a high efficiency and environmentally-friendly method with dopamine (DA) covered on the graphene oxide in the form of a uniform layer and then reacted with α -mercaptoethanol (Qu et al. 2016). After then, the N, S-codoping carbon nanosheets obtained by pyrolysis of GDS with a high S-doping efficiency. This catalyst shows admirable bifunctional ORR and OER electrocatalytic activity. It is believed that the high content of N, S and O provides high concentration of active sites and the synergetic effect between doping atoms and carbon material increases active sites of C, the oxygen functional groups provide by O atom make the catalyst more hydrophilic and are easily reacted on the interface of electrolyte and electrocatalyst. In addition, the mesoporous structure, the crinkles of carbon nanosheets, and the high conductivity are also the main reason to facilitate the reaction of OER. A macro-porous carbon fibre doped with N, F, P was fabricated by electrospinning method following with thermal annealing process (Wu et al. 2018a). It is found that the carbon fibres with uniform dispersed heteroatoms show excellent ORR and OER electrocatalytic performance.

Apart from doping with heteroatoms, defect engineering for carbon materials to enhance the surface area is also an effective way to improve the OER performance of carbon materials. A facile H_2 etching method was applied to prepare coaxial cable-like carbon fibre coated with nanostructured porous- and defect-rich graphene material (Wang et al. 2018a). This material exhibits excellent dual electrocatalytic performance for OER and ORR.

Apart from the above doping or defect method, a polymer assisted strategy is utilized to form electrocatalytic carbon materials wrapped with polymers. Unlike the doping method which commonly obtained by high temperature with high energy consumption, the polymer assisted method is facile and simple. Zhang prepared a series of polymer (*i.e.* poly (ethylene-alt-maleic) (PEMAc), poly (acrylic acid) (PAA), poly (vinyl alcohol) (PVA)) assisted MWCNTs catalyst (see Fig. 2-8) (Zhang et al. 2017b). The best PEMAc@MWCNTs electrocatalyst displays a low overpotential of 298mV at 10 mV/cm² and a small Tafel plot of 52 mV/dec. It is noticed the carbon material is not destroyed and the topological Stone-Wales defects of MWCNTs are still the main active sites and the functional groups on the wrapped polymer is used as a “kinetics accelerator” to facilitate and stabilize the OER intermediates and adjust the adsorption energies, and finally enhance the OER activity of polymer assisted MWCNTs. Mo and co-workers also synthesized MWCNTs wrapped with poly (diallyl dimethylammonium chloride) (PDDA) by the similar method (Mo et al. 2018). A homogeneous dispersion of MWCNTs and polymer were obtained by dispersing and sonicating the purified MWCNTs and polymer in a desirable solution (*i.e.* acetone, water) and then the solution was evaporated or vacuum-filtered to form the polymer wrapped MWCNTs. It is found that PDDA with electron withdrawing property could lead a p-type “doping”, while the electron-donating polyethyleneimine (PEI) causes a n-type “doping”. The previous PDDA/MWCNTs electrocatalyst has more effective electrocatalytic ability than PEI/MWCNTs in water oxidation reaction. The directional interfacial electron charge transfer between MWCNTs and PDDA brings more carbon sites with positive charge, and the quaternary ammonium cations adsorb more OH⁻ ions by electrostatic interaction

at the electrode/electrolyte interface, both of above two functions improve the MWCNTs electrocatalytic performance.



Fig. 2-8 (a) Schematic illustration of preparation procedure for flexible OER electrocatalyst based on polymer @MWCNTs composite membranes, (b) a photograph of the flexible free-standing PEMAs @MWCNTs 90 membrane. Cited from Ref (Zhang et al. 2017b).

2.3.4.2 Transition metal or TMOs

In addition to carbon materials, transition metal and TMOs with low cost, highly active and long-term stability are extensively investigated by tremendous researchers during the past years to replace the expensive precious metals or precious metal oxides (Song et al. 2018, Han, Dong and Wang 2016).

Transition metals as abundant elements on the earth were investigated by many researchers in electrocatalytic field, especially Ni, Fe, Co. However, although transition metal usually have electrocatalytic performance, the drawback of aggregating in the process of electrocatalytic reaction, lacking of high conductivity limit their wide application. Hence, most metal materials usually composited with carbon materials, or 3D metal substrate to increase the active sites, enhance the conductivity and hamper the aggregation of metal atoms during the process of electrocatalytic reaction. For example,

Han *et al.* synthesized FeN_x/C catalysts by pyrolysis of thiourea and agarose with α -Fe₂O₃ as Fe precursor (Han et al. 2018). When the pyrolysis temperature was 700°C and the mass ratio of urea and α -Fe₂O₃ was 20, the catalyst exhibits a better OER performance than that of 20% Pt/C, although its OER performance is not good as that of IrO₂. The outstanding OER performance is due to the positively charged carbon and N atom rounded Fe which could adsorb OH⁻ and thus further facilitate the transfer of O₂²⁻ and O²⁻ generated in the process of OER. Except single metal element, bi- or tri-metallic materials show more advantages than mono-metallic materials. NiFe/C electrocatalyst was prepared by a simple method with Fe doped Ni(OH)₂ as precursor and glucose as carbon source, after annealing at high temperature, a sandwiched-like NiFe material coated by graphene sheets on the both sides was obtained (Feng et al. 2015). The unique structure with conductive graphene sheets promotes the transfer of electron and OH⁻ and impedes the aggregation of NiFe nanoparticles. Besides, the porous structure could increase the contact surface area between active sites and electrolyte and further improve the OER electrocatalytic activity of NiFe/C material. Ni₃Fe/N-C sheets was synthesized by an effective dissolution-recrystallization-pyrolysis method (see Fig. 2-9) (Fu et al. 2017). In this process, NH₃ was used to provide N sources and increase the porosity of the materials, chitosan (CS) could form a porous carbon during pyrolysis. Ni₃Fe sheets embedded into the carbon nanosheets, thus avoiding the aggregation of Ni₃Fe, the N doped carbon sheets also improve the electric conductivity of metal material, promoting the transfer of electron and improving the electrocatalytic activity of material. A bifunctional electrocatalyst of Ni₃FeN/Co,N-CNF (carbon nanoframes) was synthesized and studied by Wang, *et al.*

(Wang et al. 2017a). And a lower overpotential (270mV) and lower Tafel slope are obtained compared with that of Ni₃FeN and IrO₂. The reason is that the size of Ni₃FeN nanoparticle as a part of hybrid material is smaller which could expose more active sites. The carbon materials with high conductivity could improve the electrochemical kinetics.

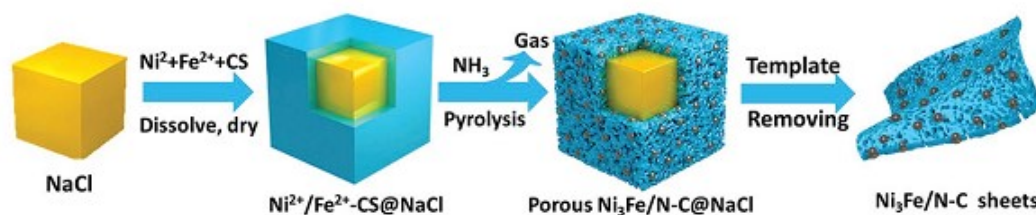


Fig. 2-9 Schematic illustration of the preparation procedure of the Ni₃Fe/N-C sheets. Cited from Ref (Fu et al. 2017).

Carbon materials such as graphene, CNT, CC used as substrate is a good choice due to its high conductivity and porous structure and chemical stability. Ni foam is also a common three-dimensional substrate used as supported material. For instance, Xu founded that amorphous NiFe nanotube arrays on Ni foam synthesized by electrodeposition method have excellent OER performance in 1M KOH solution with small overpotential of 216 mV at 50 mA/cm² (Xu et al. 2018b). They claimed that the excellent electrocatalytic activity is due to their intrinsic advantages: (i) the composition of Ni, Fe has a synergistic effect with strong electron reaction which could increase more active sites, more mass and charge transport competence, (ii) the amorphous phase is favourable for high charge transfer rate and increasing the exposed active sites, (iii) the high surface area, abundant active sites are beneficial for enhancing the electrocatalytic performance for composite of Ni foam and NiFe nanotube arrays.

In addition to Ni and Fe, Co is also a common metallic element used as electrocatalyst (Chen et al. 2018). Cai fabricated a 3D Co-N-codoped hollow carbon sphere materials with dopamine as nitrogen and carbon source and PMMA as template by a simple vacuum-assisted impregnation method (Cai et al. 2017b). The catalyst shows good OER performance with an overpotential of 490 mV at 10 mA/cm² in 0.1M KOH. X-ray photoelectron spectroscopy (XPS) verifies the existence of N and C elements. It is accepted that carbon materials doped with N have high charge mobility which could enhance the catalytic activity. Although, XRD and XPS also confirm the presence of Co-O bond. There is no clear evidence to prove that the excellent OER performance is attributed to the existence of metal oxide in this work. However, in Tong's work (Tong et al. 2018), it is pointed out that the real active sites to facilitate the formation of O₂ from OH⁻ is CoOOH/Co-N catalyst which formed by partially oxidized Co atoms on the surface of Co-N species, Hence, a confusion that the real catalytic active sites for metal material is the metal itself or metal oxides existed on the surface or generated during the reaction is still need to be further investigated. In Liu's work, XRD, XPS and X-ray adsorption fine structure (X-ray absorption near edge structure, XANES) and extended X-ray absorption fine structure (EXAFS) spectroscopy were applied to indicate the presence of cobalt oxides (Liu et al. 2018b). And it is concluded that the superior OER electrocatalytic activity of Co/NBC-900 is due to the high content of conductive pyridinic C-N and C-B structures and also the existence of surface oxides on the outer layer of metallic cobalt which could increase the electron transport capability and supply more electrocatalytic active sites for easy access of electrolyte. The result and discussion show that the existence of cobalt oxide on the surface could

make the catalyst film more hydrophilic which is beneficial for the access of electrolyte. Fu *et al.* discussed more details about the surface composition and improvement of OER of NiCo alloy nanoparticles on N-doped carbon nanofibers synthesized by electrospinning and post-calcination method (Fu *et al.* 2018). The results of XPS show that Co^{2+} , Co^{3+} , Ni^{2+} , Ni^{3+} located on the surface of sample, and Co^{3+} , Ni^{3+} have been hydroxylated during the OER process which is beneficial for enhancement of OER performance of product. Mentioned metal oxides, many efforts on preparing metal/metal oxides composite also attract tremendous attention. It is believed that metal/metal oxide composite displays a higher catalytic activity when comparing with single metal oxides materials. The metal in the material contributes to improve the electrical conductivity of composites and the different metal generated lattice strain is responsible for different redox potential and structural ordering, and this improves the electrocatalytic performance of sample (Wu *et al.* 2018b, Liu *et al.* 2015a).

2.3.4.3 LDHs

LDHs have layered structure with metal ions formed host layer and anions intercalated into the layer to balance the positive charge caused by partially trivalent metal ions which in the place of bivalent metal ions. Up to now, due to the adjustability of metal compositions, exchange of interlayered anions and various of derivatives, such as oxide(hydroxides), phosphides, nitrides, selenides *etc.*, a great of effort have focused on the research of LDHs, especially NiFe LDHs which have indicated that they have outstanding OER performance (Wang *et al.* 2018c, Gong and Dai 2014). However, the low conductivity, small active sites on bulk LDHs limited their further application. Hence, design and efficient solutions have been done by many workers. The effective

strategy includes decreasing Gibbs energy by adjusting electronic structure, increasing surface area to exposed more active sites, enhancing the conductivity of LDHs by combing with conductive materials, *etc.*.

2.3.4.3.1 Electronic structure changing

It was verified that doping with other elements such as V, Cr, Au, Co could adjust the electron structure and improve the oxidation potential of Ni or Fe to influence the electron density and enhance OER activity (Dinh et al. 2018).

For instance, NiFeCr LDHs was directly grown on the carbon paper by one-step hydrothermal reaction (Yang et al. 2018). It is found that the electrocatalyst has a low overpotential of 225 mv at 25 mA/cm² and a small Tafel slope of 69 mV/dec. The results of XPS and X-band electron paramagnetic resonance spectroscopy (EPR) indicate that Cr has changed the electronic structure of Ni compared to bimetallic NiFe and NiCr LDHs, and partially substitutes for Fe in the M(OH)₂ layer. The excellent OER performance is attributed to not only the introduction of Cr which adjusts the electronic structure and influences the intrinsic activity, but also the utilization of hydrophilic carbon paper with high surface area and the strong interaction between LDHs and carbon paper which facilitates the high electrocatalytic performance and long-term durability. V as an earth abundant element is also studied to dope with NiFe LDHs. Li *et al.* synthesized V doped NiFe LDHs on Ni foam by a hydrothermal method with low overpotential of 195mV at 20 mA/cm² and low Tafel slope of 42 mV/dec (Li et al. 2018a). The electrochemical analysis and density functional theory (DFT)+U show that the doping of V enhances the electrocatalytic activity of Fe by electronic

interaction and decreases bandgap between the valence and conduction bands which modulate the electronic structure. Hence, NiFeV LDHs performs an outstanding OER electrocatalytic activity. Excepting for directly fabricating trimetallic LDHs by hydrothermal method, electrodeposition is an easily method to introduce metal ions to the host layer of NiFe LDHs. Zhu *et al.* integrated electronegative Au uniformly on the surface of arrayed NiFe LDHs on Ni foam (Zhu et al. 2017). The small content of Au influences the structure of LDHs, and XPS demonstrates that electronegative Au could adsorb electron and promote the formation of Ni³⁺ cation and thereby enable the OER performance of LDHs. Zhang and co-workers also used hydrothermal and electrodeposition method to synthesize ¹⁹⁷Au/NiFe LDHs on Ti mesh (Zhang et al. 2018b). They used DFT+U+vdW (van der Waals effects) to prove that the single atom Au could decrease the free energy and improve the OER performance. The *in-situ* Raman spectroscopy indicates that the in situ formed oxyhydroxide act as active sites in OER. In addition to cation doping, defect engineering strategy is another effective method to tune electronic structure. Xie and co-workers introduced base-soluble Zn (II) and Al(III) NiFe-LDHs, when the Zn (II) and Al(III) were selectively etched, atomic M(II)/M(III) defects formed (Xie et al. 2018). The results show a low overpotential of 200 mV at 20 mA/cm² and a small Tafel slope of 34.9 mV/dec. It is believed that the electronic state of metal sites rounded the atomic defects would balance the change of charge when atomic defects generated after selectively etched. The XPS and EPR demonstrate that M(II) defects generate unsaturated O-coordination of Ni(II)-O-Fe(III) couple sites and Ni, Fe sites are shifted to a lower valence in the D (defect)-NiFeZn LDHs, which is beneficial for OER (See Fig. 2-10). DFT +U calculations elucidate that

the defect sites of Ni(II)-O-Fe(III) in the M(II) defect structures have a lower OER overpotential than Ni(II)-O-Ni(III) defect sites in the M(III) defect structures, Hence, D-NiFeZn LDHs shows a better OER performance than D-NiFeAl LDHs.

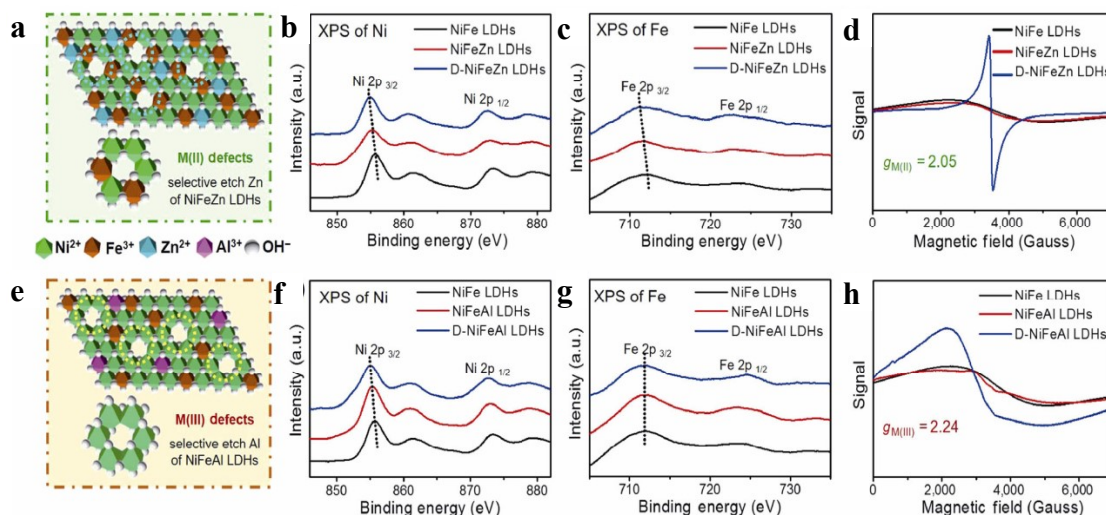


Fig. 2-10 Schematic defect structures of (a)D-NiFeZn LDHs and (e) D-NiFeAl LDHs; (b), (f) Ni 2p and (c),(g) Fe 2p XPS results of the as-synthesized LDHs (the distinct negative shift of the signals indicates modified electronic structures); and electron paramagnetic resonance spectra of (d)NiFe, NiFeZn, and D-NiFeZn LDHs and (h) NiFe, NiFeAl, and D-NiFeAl LDHs. Cited from Ref (Xie et al. 2018).

2.3.4.3.2 Morphology and structure control

It is commonly accepted that ultrathin and hierarchical LDHs with high specific area usually have more exposed active sites than bulk LDHs. Decreasing the size of LDHs or constructing hierarchical structure or 3D structure of LDHs could increase the specific area and hence generate more active sites, facilitate the penetration of electrolyte, these merits are beneficial for improving the OER performance. For example, Dinh and co-workers fabricated porous ultrathin NiFeV LDHs on Ni foam

(Dinh et al. 2018). The thickness of LDHs is about 10 nm, and these porous nanosheets assembled to form a flower-like structure on Ni foam (See Fig. 2-11a). It is believed that the porous structure provides more space for electrolyte penetration and diffusion. Hence, the high specific area with more exposed active sites and the porous structure with fast electrolyte penetration and diffusion are favourable for improving OER performance. Similarly, Hierarchical NiFe LDHs hollow microspheres (HMS) was also prepared by one step in situ growth method with SiO₂ as a sacrificial template (See Fig. 2-11b and 11c) (Zhang et al. 2016a). N₂-adsorption/desorption analysis reveals that NiFe-LDHs HMS has a larger specific surface area of 155.4 m²/g than that of NiFe-LDHs nanoparticle (NP) (22.9 m²/g). The ECSA results also show that the value of C_{dl} of NiFe-LDHs HMS is 4.6 times higher than that of NiFe-LDHs NP. Hence, the enhancement of OER electrocatalytic activity of NiFe-LDHs HMS with a small onset overpotential of 220 mV is ascribed to the high surface area and hollow structure with mesopore (3-5 nm) which could increase the exposed active sites, enhance the transportation of charge and mass. The hard templates usually were used to prepare the hollow structure, but the removal of template not only increase the cost of preparing, but also may destroy the structure which have been formed. Hence, in David's work, a self-templated method was used to synthesize hierarchical NiFe-LDHs hollow nanoprisms (see Fig. 2-11d-f)) (Yu et al. 2018a). Ni precursor as the template and Ni source, was dissolved and transformed into the active component of electrocatalyst. Due to the hierarchical and porous structure, NiFe LDHs hollow nanoprisms has a high OER electrocatalytic activity with overpotential of 280 mV at 10 mA/cm² and a small Tafel slope of 49.4 mV/dec. It is concluded that the high OER performance is

influenced by the porous nanoprisms structure which could facilitate the electrolyte penetration and diffusion, and increase the contact area between electrode and electrolyte.

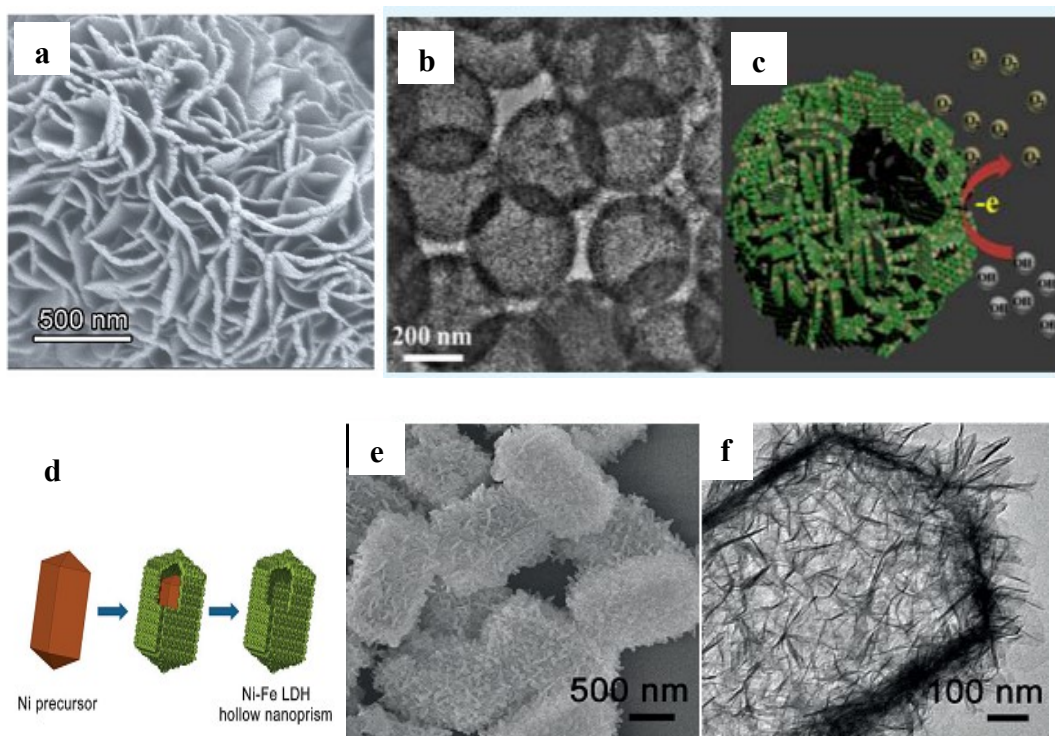


Fig. 2-11 (a) FESEM image (cited from Ref (Dinh et al. 2018); (b), (c) TEM image and sketch of NiFe-LDHs HMS; Cited from Ref (Zhang et al. 2016a); (d) scheme of formation of hierarchical NiFe-LDHs hollow nano prisms by a self-templated strategy, and (e), (f) FESEM and TEM images of Ni-Fe LDHs hollow prisms obtained after the hydrolysis reaction. Cited from Ref (Yu et al. 2018a).

Except for direct synthesizing LDHs with hierarchical structure, 3D conductive metal used as substrate in the process of preparing LDHs can increase specific surface area with more exposed active sites, enhance the electronic conductivity with fast electron transfer, the 3D dimensional structure with more space promotes the fast release of oxygen gas generated in the process of reaction. Hence, constructing hierarchical

structure on 3D conductive substrate is an effective pathway for achieving high OER performance for electrocatalyst. Ni foam, Cu foam as typical 3D conductive substrate have attracted a great deal of attention. Ni foam as common substrate in electrochemical field was used as substrate for synthesizing NiFe LDHs nanoplates in Duan' work (Lu et al. 2014). The NiFe LDHs nanoplates vertically grown on the Ni foam and formed 3D porous film, the results indicate that the NiFe LDHs nanoplate exhibits outstanding OER performance with a low overpotential (280 at 30 mA/cm²) and a small Tafel slope (50 mV/dec).

Cu as a high conductive metal also used as a substrate for preparing LDHs. For instance, a core-shell structured Cu@NiFe LDHs was obtained by a facile and safe approach (see Fig. 2-12) (Yu et al. 2017b). It is believed that the NiFe LDHs nanosheets have a strong interaction with Cu nanowires which ensure high electronic transportation, and the vertically NiFe LDHs ultrathin nanosheets on Cu nanowires have many exposed active sites. Hence, an excellent result is achieved with overpotential of 199 mV and 281 mV at current density of 10 and 100 mA/cm², respectively. And this electrocatalyst also shows outstanding HER performance and is used as bifunctional in water splitting. Similar work about Cu@CoFe LDHs also has been investigated (Yu et al. 2017a). When the electrodeposition time is 90s, the hierarchical Cu@CoFe LDHs exhibits overpotential of 252 mV and 318 mV at 10 and 100mA/cm², respectively, and a Tafel slope of 44.4 mV/dec.

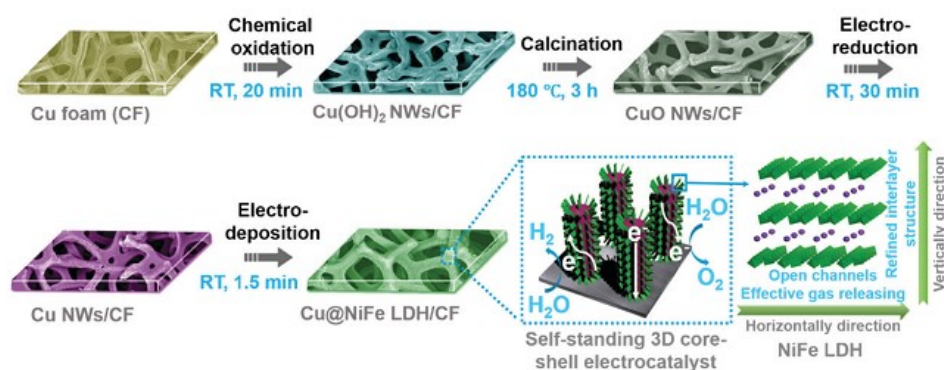


Fig. 2-12 Schematic illustration of the fabrication procedures of the self-standing 3D core-shell Cu@NiFe LDHs electrocatalysts. (RT represents for room temperature) Cited from Ref (Yu et al. 2017b).

Due to the unique layer structure of LDHs, the anion in the layer could be exchanged by a series of anions, such as NO_3^- , ClO_4^- etc. and LDHs can also be exfoliated into few layers or single layer. The increased interlayer distance or the ultrathin nanosheet of LDHs have large specific area and expose more active centres. Hence, by enlarging or exfoliating the structure of LDHs, the OER electrocatalytic properties of LDHs have been improved. Zhong *et.al.* prepared Ni_2Fe -LDHs with interlayered anion of sodium dodecyl sulfonate (SDS) on carbon fiber (Zhong et al. 2017). They summarized the outstanding OER performance is attributed to the enlarged interlayer distance which could accelerate the electrolyte diffusion. However, it contradicted to the research about the investigation of NiFe LDHs with different anion intercalation (Hunter et al. 2016). The study demonstrates that LDHs with different anions will be quickly replaced by carbonate in alkaline electrolyte under ambient air, and in the virtually carbonate free alkaline electrolyte, the activity is related to the function of anion basicity, and they suggested that nitrite species bound to the edge site of Fe in the pre-catalyst influenced

the water oxidation activity. Hence, for LDHs with the intercalation of SDS which expand the distance of LDHs, when it is dispersed in alkaline solution without protecting by inert atmosphere, the SDS might quickly be replaced by carbonate. Hence, the product should be analysed in detail to check the existence of SDS or CO_3^{2-} for further discussion. In addition to the method of increasing interlayer distance of LDHs, the exfoliation of LDHs into few layers or single layer is also an useful approach to achieving electrocatalyst with high OER activity (Tingting Wang 2019). Because the few layer or single layer LDHs usually have more exposed active site, and form numerous edges and corner sites which could accompany with more dangling bonds and decrease coordination number of active sites and promote the adsorption of intermediates generated in OER process. All these results will reduce the overpotential and enhance the OER activity. Song and Hu prepared a series of exfoliated LDHs by using liquid method to study their OER performance (Song and Hu 2014). Firstly, NiFe LDHs with carbonate as intercalated anions was prepared by hydrothermal method while NiCo and CoCo LDHs with Br were fabricated by topochemical way. Then the interlayer distance of as-prepared LDHs will be expanded by exchanging the anions by ClO_4^- for NiFe LDHs and NO_3^- for NiCo and CoCo LDHs. After dispersing and stirring vigorously in formamide for 24h, the clear solution was collected, the bulk LDHs formed into single layered tested by XRD and SEM and AFM (see Fig. 2-13). Finally, the electrochemical analysis demonstrates that the single layer of LDHs display enhanced OER electrocatalytic activity which is shown by LSV, turnover frequency (TOF), *etc.* It is concluded that the increased high surface area is the main contributor for the significant improvement of OER performance. The reduced size, increased edge

sites with the unchangeable MO_6 network are also the influence factors for the enhancement of OER activity.

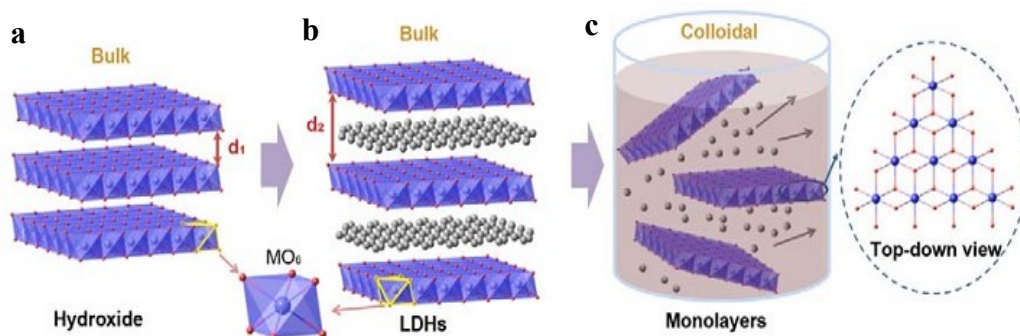


Fig. 2-13 Schematic representation of materials structures. (a) Layered hydroxides, d_1 is the interlayer distance. (b) LDHs with interlayer anions and water molecules; d_2 is the interlayer distance, $d_2 > d_1$. (c) Exfoliated LDHs monolayers dispersed in a colloidal solution. Each single layer is composed of edge-sharing octahedral MO_6 moieties (M denotes a metal element). Metal atoms: purple spheres; oxygen atoms: red spheres; interlayer anions and water molecules: grey spheres. Hydrogen atoms are omitted. Cited from Ref (Song and Hu 2014).

2.3.4.3.3 Enhancing the conductivity of LDHs

The intrinsic conductivity of LDHs is very small and this limits their OER performance and widely applications. Hence, combining with high conductive materials, especially carbon materials have been indicated as an effective approach to improving the OER electrocatalytic activity of LDHs. The common conductive materials usually include Ni foam, carbon materials (CNTs, graphene, carbon nanofiber, carbon quantum dots, CNF), especially carbon materials, due to the various carbon materials and different defective and structure, the hybrid of carbon materials with LDHs as electrocatalysts have been studied by many groups.

MWCNTs with tube structures are considered as an ideal carbon material for improving the OER performance of LDHs. In the composite of LDHs/MWCNTs, LDHs uniformly dispersed on MWCNTs and MWCNTs enhance the conductivity and could impede the growth of size of LDHs which could increase the contact surface area with electrolyte, further enhance the electron transfer and mass transfer. For instance, Gong *et al.* prepared ultrathin NiFe LDHs nanoplates on mildly oxidized MWCNTs by an solvothermal method (Gong et al. 2013). The strong interaction between LDHs and MWCNTs forms interconnected electrically conductive networks which facilitate electron transfer, the tube structure of MWCNTs and the ultrathin LDHs nanoplates increase the active surface area, the tube network of MWCNTs facilitates the electrolyte diffusion and transfer. Hence, the composite of LDHs/MWCNTs displays an excellent OER activity with an overpotential of 250 mV at 10 mA/cm². In this work, mildly oxidized MWCNTs were prepared by a modified Hummer method, which prevent the serious structural destroy of MWCNTs and could keep the tube structure and the high conductivity. Hence, the composite shows a remarkable OER performance.

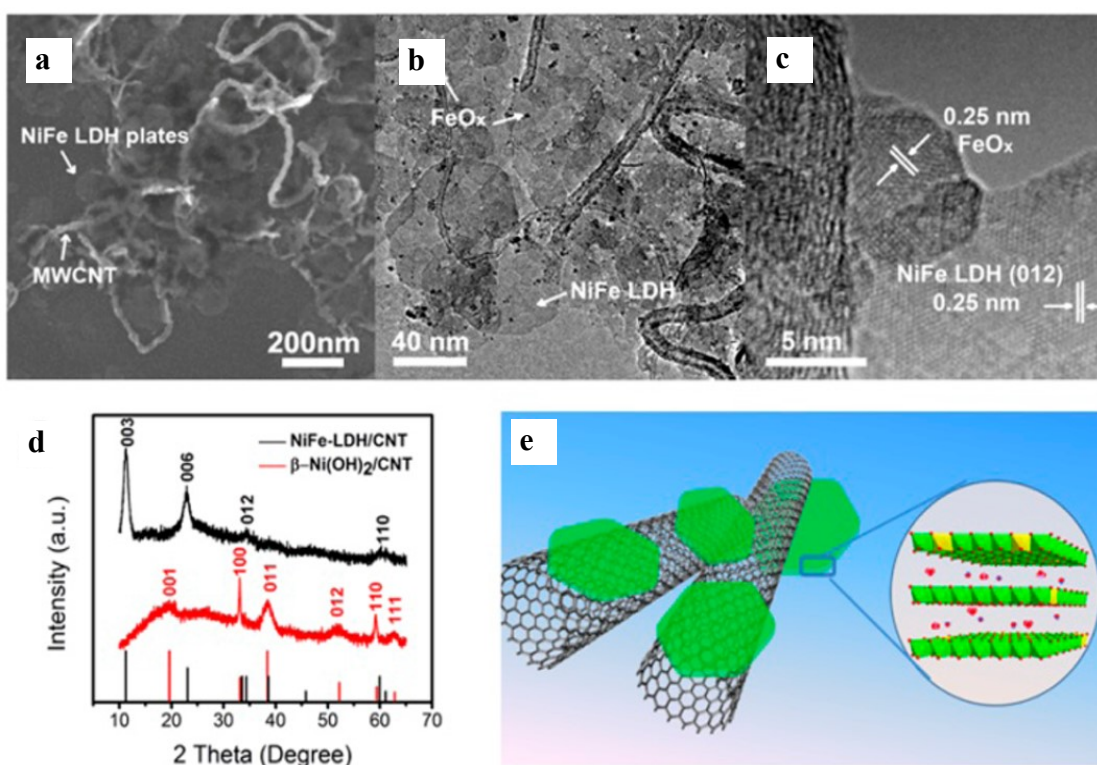


Fig. 2-14 (a) SEM image of NiFe LDHs nanoplate grown on a network of mildly oxidized MWCNTs. **(b), (c)** TEM images of NiFe-LDHs/ MWCNTs hybrid. **(d)** XRD spectra of NiFe-LDHs/ MWCNTs hybrid (black) and a control β -Ni(OH)₂/ MWCNTs sample (red). The lines correspond to standard XRD patterns of α -Ni(OH)₂ (black, JCPDS card No.38-0715) and β -Ni(OH)₂ (red, JCPDS card No.14-0117). **(e)** Schematic showing the hybrid architecture and LDHs crystal structure. Cited from Ref (Gong et al. 2013).

Graphene, a layered carbon material, has attracted tremendous attention due to its unique structure and properties. Combining LDHs with graphene or its derivatives to improve the electrocatalytic performance of LDHs have been verified. NiFe LDHs/rGO, for instance, has been prepared by a facile solvothermal way with the following of chemical reduction (Zhan et al. 2016). Electrochemical results show the NiFe-LDHs/rGO exhibits an overpotential of 240 mV at 10 mA/cm² and a small Tafel slope of 91 mV/dec. It is summarized that the porous structure and strong interaction between rGO and

NiFe-LDHs are beneficial for the fast electron transfer, more exposed active sites and fast release of oxygen. In addition to rGO, heteroatoms doped graphene and graphene with topological defects used as substrate also caused many researchers' attention. Yao et al. produced positively charged NiFe-LDHs and negatively charged defective graphene (DG) by electrostatic interaction (Jia et al. 2017). Fig. 2-15a shows that exfoliated NiFe LDHs nanosheets after exfoliation assemble with negatively charged DG. NiFe-LDHs/DG 10 has outstanding OER electrocatalytic activity with an overpotential of 210 mV at 10mA/cm² and a small Tafel slope of 52 mV/dec (See Fig. 2-15 b). The defects on DG react with metal atoms sites by π - π interaction and form strong interaction between LDHs and DG, facilitating the electron transfer and improving kinetic of OER. The layer and porous structure provides high surface area and enough path for reaction and releasing of produced gas. In another work, defective N-doped graphene oxide as a substrate, NiFeCo LDHs vertically grown on it (See Fig. 2-15c, d) (Zhou et al. 2018a). In this work, three merits for improving OER are summarized: (i) the defects on N-GO provide active sites for metal ions and enhance the interaction between LDHs and N-GO which promote the electron transfer and stabilizes the composite, (ii) the array-like structure could expose more active sites and facilitate the penetration of electrolyte and release the generated gas quickly, (iii) the high valence state Co^{III} is beneficial for OER by tuning electronic structure of LDHs.

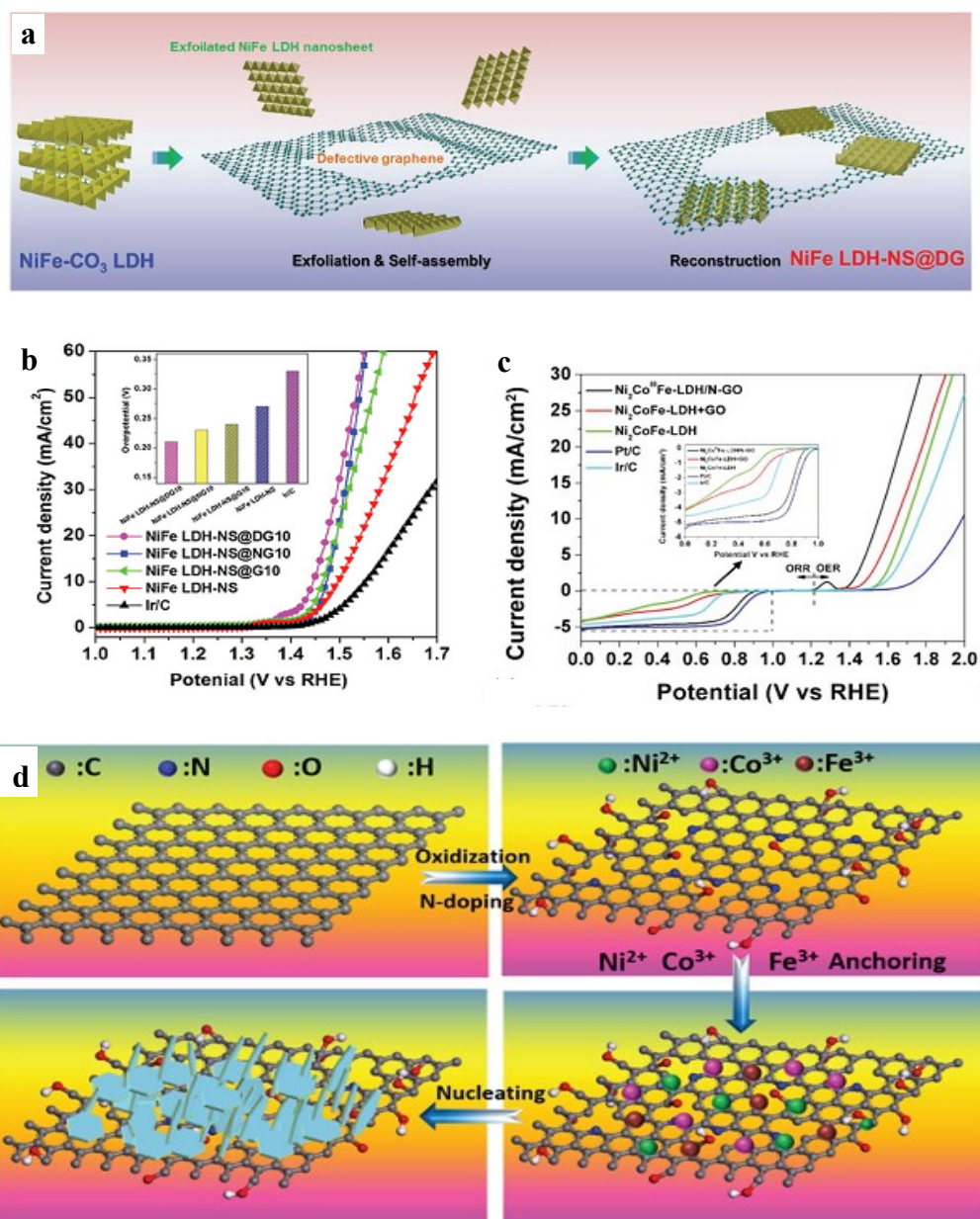


Fig. 2-15 (a) Schematic illustration of the fabrication of NiFe LDHs-NS@DG nanocomposite.

(b) LSV curves of different electrocatalysts in 1 M KOH solution (the inset is the overpotential required at a current density of 10 mA/cm²), Cited from Ref (Jia et al. 2017).

(c) ORR and OER LSV curves (at 1600 rpm) of Ni₂CoFe-LDHs+GO, Ni₂CoFe-LDHs, Ir/C, and Pt/C-20%.

(d) Schematic of the in-situ growth of LDHs nanosheets on nitrogen doped

GO (N-GO). Cited from Ref (Zhou et al. 2018).

In addition to CNTs, graphene or graphene derivatives, carbon fiber, carbon quantum dots (Tang et al. 2014), carbon nanofram (Wang et al. 2017b), porous grahitized carbon (Ni et al. 2017), even graphite foam (Li et al. 2018b), expandable graphite (Guo et al. 2018) also have been investigated. For these carbon materials, the high surface area with more active sites, high electronic conductivity which increase electron transfer and kinetics of OER and defective or heteratom doped sites which maximize the interaction between carbon materials and LDHs, are favorable for OER.

2.3.4.3.4 Amorphous metal oxides or hydroxides

Due to more active sites generated by the short range order of amorphous structure and small clusters exsited in amorphous material, electrocatalysts with amorphous structure usually have outstanding OER performance. Hence, numerous research have focused on amorphous materials, such as metal hydroxides, metal oxides. The common strategies for preparing amorphous materials is electrodepostion and self-assembly (Liu et al. 2017, Xiaomei Wang 2018). For example, Lu and Zhao synthesized amorphous NiFe composite nanosheets on macroporous Ni foam electrode by electrodepostion method (Lu and Zhao 2015). The product shows excellent OER performance due to the hierarchical porous structure generated by Ni foam and small amorphous NiFe particles and high conductivity of Ni foam. These phenomena could increase the sepecific surface area and ehance the electron transportation. It is commonly recognized that combing with conductive materials can not only enhance the conductivity of LDHs, but also impede the growth of particles which downsize the scale of particle and further expose more activce sites. A ultrafine amorphous NiFe LDHs and nanocarbon composite were prepared by one pot solution method (Yin et al. 2018). In this work,

carbon materials came from the N containing carbon source (2-mercapto-5-nitrobenzimidazole (MNBI)) which is considered as a ligand react with metal ions and confine the growth of NiFe LDHs, after solvothermal treatment, organic ligand forms nanocarbon on the amorphous surface of NiFe LDHs. The hybrid of NiFe LDHs and nanocarbon display high OER activity. The overpotentials are 210mV and 260mV at 10 and 100 mA/cm² and Tafel slope is 35mV/dec. It is demonstrated that the amorphous and distorted structure, strong interaction between NiFe LDHs and nanocarbon are responsible for the enhancement of OER performance. Ren *et al.* fabricated a hybrid electrocatalyst of NiFe LDHs and nickel phosphide with a core-shell structure (Yu et al. 2018b). Here, the high conductive nickel phosphide as the substrate provides 3D porous structure for the electrodeposition of amorphous NiFe LDHs.

NiFe(oxy) hydroxide as another high OER electrocatalyst was also studied in its amorphous form (Zhou et al. (2018b)). Liu et al. synthesized NiFeOOH by a facile electrodeposition step on 3D partially exfoliated graphite foil (Ye, Zhang and Liu 2017). The result shows a remarkable overpotential (214 mV at 10 mA/cm²) especially at high current density (251 mV at 500 mA/cm²). The reason is that the 3D graphite foil substrate ensures the formation of hierarchical structure which could promote the diffusion of gas generated in the process of reaction. Shen et al. developed amorphous Ni(Fe)O_xH_y coated nanocone arrays (NCs) on stainless steel mesh (SSM) by a two step approach, i.e., acid corrosion and nickel (oxy)hydroxide deposition (Shen et al. 2018) (See Fig. 2-16). It is demonstrated by EIS that the charge transfer resistance of SSM-NCs/Ni(Fe)O_xH_y is only 0.13 Ω which is the important contributing factor for superior OER performance. It is pointed out that the reasons for lowering charge transfer

resistance listed as: (i) the formation of self-supported nanocone arrays on the wires of SSM substrate decreases the solid surface /surface contact area, (ii) the inner uncorroded SSM wires enhance the electric conductivity, (iii) high surface area between electrode and electrolyte due to the nanocone structure exposes more active sites. In addition to NiFe (oxy)hydroxide, other metals (oxy)hydroxides also have been investigated. Such as CoV(oxy)hydroxide (Liu et al. 2018a). It is summarized that electrodeposition is the common and facile method used for preparing amorphous bimetal (oxy) hydroxides with random ordered structure to provide more active sites and amorphous bimetal (oxy) hydroxides usually combined with 3D conductive substrate to increase the surface area and enhance the conductivity of electrocatalysts.

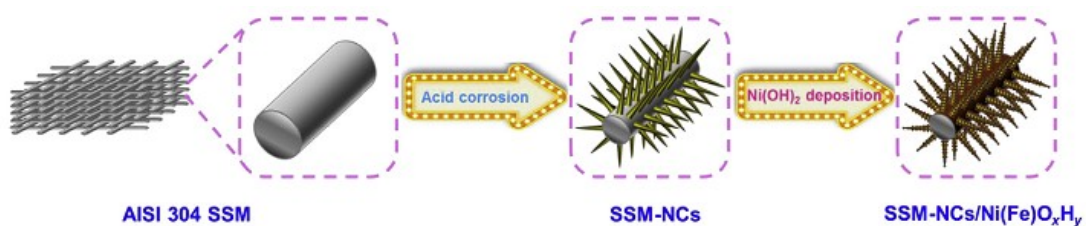


Fig. 2-16 Schematic for the fabrication process of SSM-NCs/Ni(Fe)O_xH_y via acid corrosion and nickel (oxy)hydroxide deposition. Cited from Ref (Shen et al. 2018).

In summary, TMOs or LDHs have attracted much attention as electrocatalyst in OER. However, some disadvantages are still exist, for example, low conductivity hampers the kinetic of reaction, the big size of particles decreases the active surface area. Hence, much research have been studied on how to improve their electrocatalytic activity. There are some common pathway: (i) combing with conductive material to enhance the conductivity of composite and enhance the kinetic of reaction, (ii) downsizing the shape of partices to increase active surface area, (iii) doping with other element for improving

the electronic structure which decreases the energy barrier to promote the happen of reaction.

Chapter 3 Experiment

3.1 Introduction

In this chapter, materials, equipment used in this work are introduced by the following section. Section 3.2 and 3.3 introduce the used materials, chemicals and equipment in detail. Section 3.4 gives the detailed information about characterizing the properties of as-prepared samples. Section 3.5 provides the information about how to assemble a coin cell from active material (anode material) to cell and how to measure their electrochemical performance as anode in LIBs. Section 3.6 gives the information of how to prepare sample and the electrochemical measurements in OER. the detailed preparation methods for different samples are introduced in following chapter 4, 5 and 6.

3.2 Chemicals and Materials

In this research, all chemicals were used without further purification. The chemicals are listed in table 3-1.

Table 3-1(I) Chemicals used in this work

Chemical	grade	supplier
$\text{Fe}_2\text{SO}_4 \cdot 7\text{H}_2\text{O}$	AR	Sinopharm Chemical Reagent Co, Ltd
H_2O_2 (30%)	AR	Sinopharm Chemical Reagent Co, Ltd
KOH	AR	Sinopharm Chemical Reagent Co, Ltd

Table 3-1 (II) Chemicals used in this work

Chemical	grade	supplier
NaOH	AR	Sinopharm Chemical Reagent Co, Ltd
H ₂ SO ₄ (98%)	AR	Sinopharm Chemical Reagent Co, Ltd
HNO ₃ (68%)	AR	Sinopharm Chemical Reagent Co, Ltd
Ni(NO ₃) ₂ ·6H ₂ O	AR	Sinopharm Chemical Reagent Co, Ltd.
Ethanol	AR	Sinopharm Chemical Reagent Co, Ltd.
Nafion® 117 solution	5%	Sigma-Aldrich
NH ₄ OH	GR	Sinopharm Chemical Reagent Co, Ltd.
Alumina powder (0.05μm, 0.3μm, 1μm)	~	CH instruments Inc.
LiPF ₆	EC: DMC=1:1 Vol%	DoDoChem
Lithium plate		Shengzhen Kejing Star Technology Co.Ltd.
Cu foil		Shengzhen Kejing Star Technology Co.Ltd.
Celgard 2300	PP	Shengzhen Kejing Star Technology Co.Ltd.

Table 3-1 (III) Chemicals used in this work

Chemical	grade	supplier
Super P		Shengzhen Kejing Star Technology Co.Ltd.
Expandable graphite (EG)		Qingdao Tianshengda graphite Co.Ltd.
MWCNTs	Industrial grade	Timesnano
N-methyl pyrrolidone (NMP)	anhydrous, 99.5%	Sinopharm Chemical Reagent Co, Ltd.
polyvinylidene fluoride (PVDF)	average Mn ~71,000	Sinopharm Chemical Reagent Co, Ltd.
isopropanol	AR	Sinopharm Chemical Reagent Co, Ltd.

3.3 Instruments for Preparation and Test

The instruments used for preparation and properties test in this work are listed in table 3-2.

Table 3-2 (I) Experimental equipment

Equipment	Manufacture	Model
XRD	BRUKER, Germany	Bruker D8
SEM	Zeiss, Germany	SIGMA
EDX	Oxford Instruments, UK	INCA
TEM	JEOL Ltd., Japan	JEM 2100

Table 3-2 (II) Experimental equipment

Equipment	Manufacture	Model
BET	Micromeritics instrument (Shanghai) Ltd.	ASAP2020 Plus
XPS	Kratos Analytical Ltd., UK	AXIS Ultra DLD
FTIR	BRUKER, Germany	TENSOR-37
CHI	Chinstruments.com	CHI 760E
Autolab	Metrohm	PGSTAT302N
Multi-channel potentiostat/galvanostat	Princeton Applied Research	PARSTATTM MC
Glove box	Mikrouna	UPURE
Ultrasonic Cell Crusher	Scientz Ningbo	JY98-IIIN
Ultrasonic Cleaners	Scientz Ningbo	SB-5200DTDN
Compact Precision Disc Cutter	Shengzhen Kejing Star Technology Co.Ltd.	MSK-T-07
Electric crimper machine	Shengzhen Kejing Star Technology Co.Ltd.	MSK-160E
Hydraulic Disassembling Machine	Shengzhen Kejing Star Technology Co.Ltd.	MSK-110D
Pine modulated speed rotator	Pineresearch	MSR

3.4 Characterization

3.4.1 XRD

XRD (XRD, Bruker D8) was used to study the crystal structure. In this work, A Cu X-ray tube and LynxEye detector was applied. The testing voltage was 40 KV and the current was 40 mA. The measurement was proceeded with Cu K α radiation ($\lambda = 0.1542$ nm) at a speed of 8 °/min in the Bragg angle (2 theta) range from 10 ° to 80 °. Bragg's law (Eq. 3-1) was used to obtain the information about distance of planes in the crystal.

$$2d \sin\theta = n\lambda \quad (3 - 1)$$

Where d is the spacing distance of planes in the crystal, θ represents the incident angle, n stands for any integer and λ is the wavelength of the beam.

3.4.2 SEM

SEM (Zeiss, Germany) was used to study morphology of all the as-synthesized materials. The voltage used in here was arranged from 1 KeV to 10 KeV based on the electronic conductivity of different samples. In-lens detector and Secondary electron detector (SE2) were selected for SEM imaging.

3.4.3 TEM and EDX

A transmission electron microscopy (TEM) measurement was applied to test the inner morphology of samples as prepared in this work on a JEOL JEM 2100 UHR transmission electron microscope. Before the test, the sample was firstly dispersed in ethanol/water solution (Vol.: 1:1) and following with ultra-sonication for 1h and then the ink was dropped onto the carbon-coated copper grid. After drying, the sample was

put into the chamber for TEM analysis. Selected area electron diffraction (SAED) and element mapping were also tested by TEM with assisting of EDX (Oxford Instruments, UK).

3.4.4 FT-IR

The IR spectra were measured by (FT-IR) (TENSOR-37 (Bruker Co.) The wavenumber range is from 4000 to 500 cm^{-1} . 1 mg of dried sample was mixed with 100mg of dried KBr and milled to form homogeneous phase and then it was pressed into a thin wafer before the test.

3.4.5 XPS

XPS could offer the information of element and valence. Hence, here XPS was used to test the element and valence of the as-prepared samples on a Kratos AXIS Ultra DLD (Kratos Analytical Ltd., UK) photoelectron spectrometry. High-Resolution XPS (HRXPS) was also conducted at the same time.

3.4.6 N₂ Adsorption-Desorption Measurement

N₂ adsorption-desorption measurement was utilized to test the specific surface area and pore size distribution etc. N₂ adsorption-desorption isotherm was obtained by testing N₂ adsorption mass under different P/P₀. Brunauer-Emmett-Teller method (BET) was used to calculate the specific surface area of as-prepared samples based on the data of N₂ adsorption-desorption isotherm.

3.5 Electrochemical Measurements for LIBs

3.5.1 Preparation of Electrode Pad and Assembling Coin Cell

The working electrode was prepared by mixing the following materials in NMP solution: 70wt% active material ($\text{Fe}_2\text{O}_3/\text{MWCNTs}$), 20wt% super P and 10wt% PVDF, and the mixture was sonicated for 30min and then stirred for overnight at room temperature in an airtight-bottle. The formed slurry was scraped on a Co foil current collector by a doctor blade, and then it was dried at 60°C for overnight. The dried electrode was cut into disks. Weight the quality of each disk (m_0) to calculate the mass of active material. Put these disks into oven again to dry them at 60°C for 4h to remove the influence of moisture. The mass of each materials was calculated by the following method.

Firstly, weight the quality of 10 Cu foil plates with the same diameter of above-mentioned Cu foil disk to get the average mass of each Cu foil (m_{Cu}). The mass of active material, super P and PVDF were marked with m_1 , m_2 and m_3 , so the weight of active material on every disk can be calculated by Eq.3-2:

$$m_1 = (m_0 - m_{\text{Cu}}) \times 70\% \quad (3-2)$$

The cell was assembled in an argon-filled glove box (moisture and oxygen levels were smaller than 1ppm) with 1M LiPF_6 solution in ethylene carbonate/ diethyl carbonate (EC: DEC, 1:1 by volume) as the electrolyte, Celgard 2300 (PP) as the separator, and lithium foil as the counter electrode.

3.5.2 Land Test

The packaged coin cell was tested by Land test system. The data of the charge-discharge curves, cycling performance, and rate capability were obtained. The voltage was in a range of 0.01-3V and the temperature was kept at room temperature. current densities for testing rate capability were 100, 200, 500, 1000 and 2000 mA/g, six cycles was installed for each current density. and it was well recognized that the higher the current density, the smaller the reversible capacity.

3.5.3 CV and EIS

The CV and EIS data were tested by Autolab, the potential window is from 0.01 V to 3 V with a scan rate of 0.5 mV/s. EIS was tested with a 10mV amplitude signal from 100 kHz to 0.01Hz, and the impedance data were fitted by an equivalent electrical circuit of R(CR)WC.

3.6 Electrochemical Measurement for OER

3.6.1 Preparation of Electrode

Electrocatalyst (4mg) was firstly dispersed in a solution with 780 μ l isopropanol, 200 μ l ultrapure water and then the mixture was sonicated for at least 1h, After sonication, 20 μ l Nafion solution (Nafion, 5 wt%) was added into above suspension and sonicated for 30min. 10 μ l homogeneous ink was dropped onto the glassy carbon electrode (diameter: 5 mm) which have been polished by aluminium oxide (Al_2O_3) suspension. The electrode with active material was dried at room temperature. The mass loading of the catalyst was about 0.2 mg/cm².

3.6.2 Electrochemical Test

All the electrochemical measurements were tested in a traditional three-electrode system by an electrochemical workstation (CHI 760e), Ag/AgCl filled with saturated KCl solution and Pt plate were applied as reference electrode and counter electrode, respectively. The electrolyte was 1M KOH. All potentials measured were calibrated to the RHE by the following equation: $E_{RHE} = E_{Ag/AgCl} + 0.059 \times pH + 0.197$ (where $pH = 13.8$ in 1M KOH). High purity O_2 gas was bubbled through the electrolyte for 30min before electrochemical test to removal the air and ensure the stable environment during the whole test process. The working electrode was rotated at 1600rpm to removal the oxygen generated on the surface of working electrode.

LSV was measured at a scan rate of 5 mV/s with 95% iR-compensation and Tafel slop was calculated based on Tafel equation. Before the LSV test, 15 cycles of CV were performed for activation. Overpotential was calculated by the following equation: $\eta = E_{RHE} - 1.23$. EIS was measured by using an AC voltage with a 5 mV amplitude in a frequency range from 100 KHz to 0.1 Hz. The ECSA was expressed by C_{dl} . CV curves with different scan rate were sweeping. The differences $\Delta j = j_a - j_c$ at 1.29V vs. RHE divide the corresponding scan rates to obtain the slope which was twice of C_{dl} and C_{dl} stands for ECSA. CP and multistep CP measurements were carried out without iR compensation. An airtight H shape cell was used for testing Faradaic efficiency, and it was tested by basic drainage method and the current density used for the test was 50 mA/cm².

Chapter 4 Preparation of Composites of Fe(OH)₃/EG Nanosheets and Fe(OH)₃/MWCNTs and Their Electrochemical Performance

4.1 Introduction

In this chapter, composites of Fe(OH)₃/EG nanosheets, Fe(OH)₃/AEG nanosheets and Fe(OH)₃/MWCNTs were prepared by Fenton reaction. EG-F-H, MWCNTs-F-H were also synthesized by hydrothermal method reacted with EG, AEG, MWCNTs after Fenton reaction. SEM was used to characterize the morphology of as-synthesized composites. And CV and galvanostatic charge discharge (GCD) were used to test their electrochemical properties. The results show AEG-F has higher capacity compared with EG-F, because AEG treated by acid has more oxygen functional groups which easily reacted with iron ions. MWCNTs-F has higher capacity than that of EG-F, EG-F-H, MWCNTs-F-H, due to the network structure. In the preparation process, sonication was applied as an assistance to promote Fenton reaction, and considering the reaction time and electric energy consumption, the optimized sonication time was 3h.

4.2 Experimental Section

4.2.1 Preparation of Composites

4.2.1.1 Acid Treatment to EG

Weighted 150mg EG and added it into round-bottom flask, concentrated sulfuric acid (H₂SO₄) was dropped into the flask. after continuously stirring the mixture at room temperature for 1h, concentrated nitric acid (HNO₃) was added into the above suspension. Then, the mixture was heated to 120°C for 1h with a reflux. After cooling down to room temperature, the acid treated EG was repeatedly washed with deionized

water and ethanol until the pH of solution was 7. The product treated by concentric HNO_3 and H_2SO_4 was named as AEG

4.2.1.2 Fenton Reaction

Weighted 150mg EG, dispersed it into 150mL ethanol solution and sonicated for 1h at room temperature to try to obtain a well dispersed EG suspension, then the mixture was filtrated with DI water. The obtained EG was then dispersed into 300mL DI water (0.5mg/mL), 705.6mg Fe_2SO_4 were added into the suspension with continuously stirring for 30min to ensure iron ions uniformly contact with the surface of EG. Hydrogen peroxide (H_2O_2 30%, 80mL) was dropwise added into the previous solution and stirred for 30min. After stirring, 1M NH_4OH was used to control the pH around 7-8 or 10-11 and pH is about 2-3 without adding NH_4OH solution, and then the mixture was sonicated for 4h. After sonication, the product was washed with DI water and ethanol until the pH to 7. The sample was dried in a vacuum oven at 60°C for 12h. The products obtained from AEG or MWCNTs were also prepared by the same approach. The products obtained by Fenton reaction were named as EG-F, AEG-F, MWCNTs-F, respectively.

4.2.1.3 Hydrothermal Reaction

After Fenton reaction, the products (EG-F and MWCNTs-F) were washed by water and ethanol and then were dispersed in water to form a mixture, respectively. After adjusting the pH of suspension with NH_4OH to 9-10, the mixture solution was transferred to Telfon-lined autoclaves and hydrothermally treated at 180°C for 12 h. Then the products were filtrated by water and ethanol and dried in a vacuum oven at 60°C overnight. The products were named as EG-F-H, MWCNTs-F-H, respectively.

4.2.2 Electrochemical Test

Three electrode-system with a graphite electrode as working electrode (diameter: 6mm), Ag/AgCl as a reference electrode (filled with saturated KCl) and Pt plate as a counter electrode were used to test electrochemical properties of sample. The graphite electrode should be polished firstly by using Al₂O₃ powder with different size on a polishing cloth, then washed by DI water and sonicated just for 1min in ethanol. The electrode active material was prepared by mixing the electroactive material (94wt.%), poly(tetrafluoroethylene) (5 wt.%) binders in NMP solution and sonicated to form a homogeneous slurry, and then the suspension was dropped onto the polished graphite electrode and dried at 40°C for overnight. The dried electrode was tested in 1M KOH solution.

4.3 Characterization

As illustrated in Fig. 4-1, the preparation process of composites was divided into two steps. In first stage, Fenton reaction was used to introduce oxygen functional groups on carbon material, due to the existence of hydroxyl radical (HO·) generated by the reaction of hydrogen peroxide and ferrous ion which acted as a catalyst. After introducing oxygen functional groups on the surface of carbon material, the carbon material with negatively charged oxygen functional groups will reacted with the positive charged iron ions by electrostatic interaction effect. Finally, composites of Fe(OH)₃/carbon material were produced after washing and filtrating.

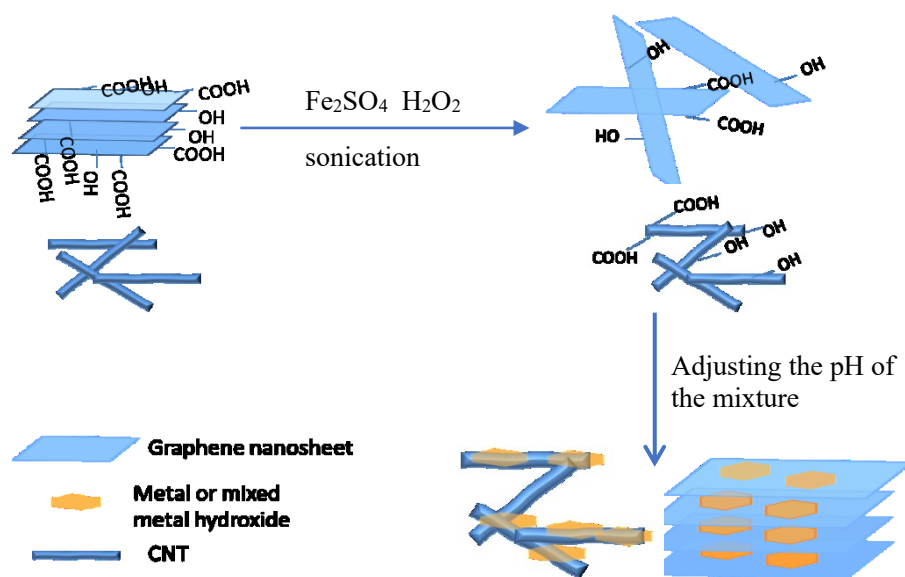


Fig. 4-1 Schematic illustration of preparing composite of Fe(OH)₃ and carbon materials (graphene nanosheet and MWCNTs).

4.3.1 pH Control

Fig. 4-2 shows TG curves for EG and EG-F prepared under different pH. Two steps of loss of mass are observed with the increase of temperature. The first weight loss around 200°C is ascribed to the loss of adsorbed water. And the second weight loss around 400°C -500°C is the removal of oxygen functional groups. From the curves, it can be seen, the series of EG-F exhibit less weight loss at around 200°C due to the existence of Fe(OH)₃ which has a tight attachment with -COO⁻ groups on EG surface. With the increase of pH, the weight loss become smaller and smaller, due to more generation of Fe(OH)₃ on EG surface. Which can also be seen in Fig. 4-3.

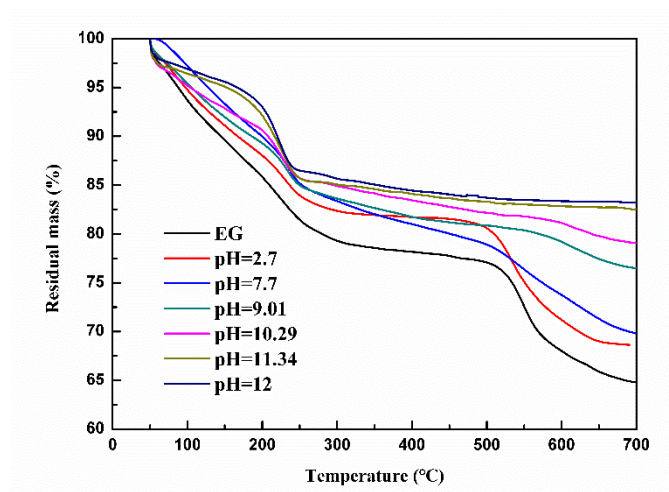


Fig. 4-2 TG curves of EG and EG-F obtained under different pH.

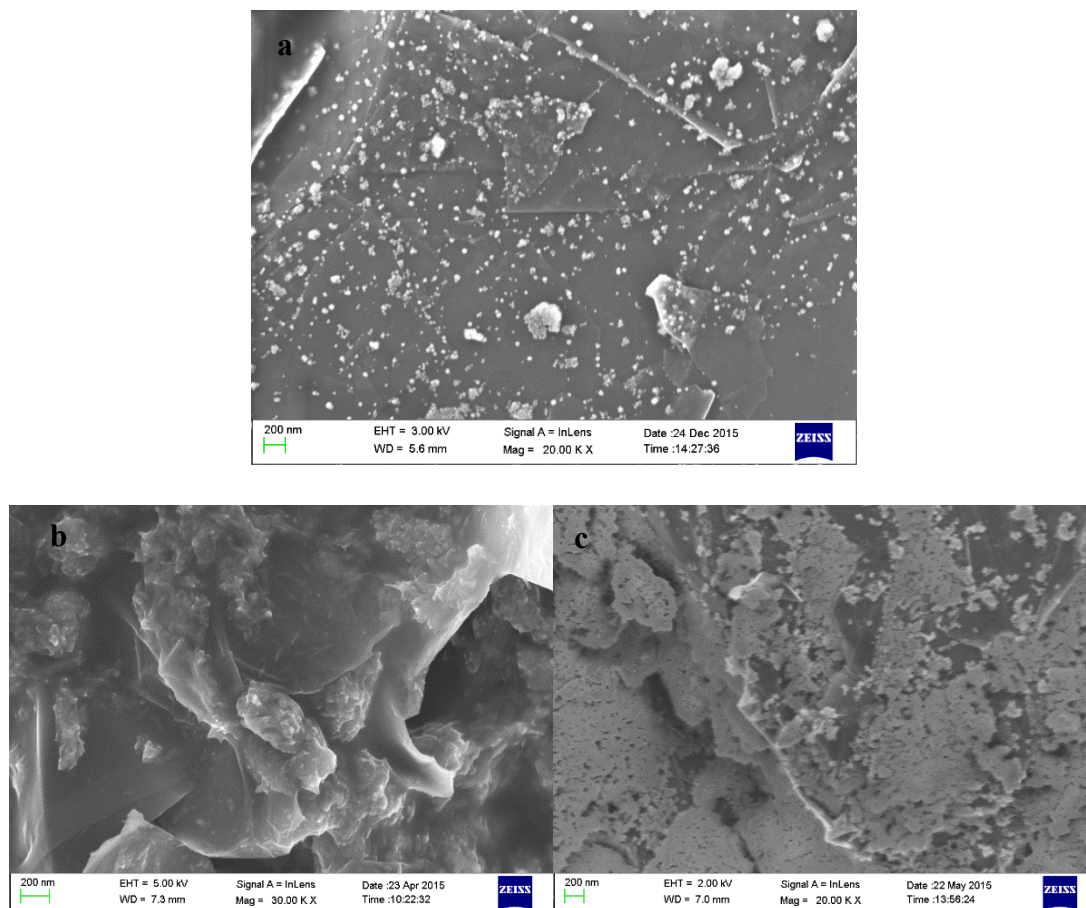


Fig. 4-3 SEM of EG-F with (a) pH=2.7, (b) pH=9 and (c) pH=11.

The SEM images in Fig. 4-3 show that the number of $\text{Fe}(\text{OH})_3$ particles increase with the increase of pH, and when $\text{pH}=11$, the particles almost cover the surface of EG. The size and shape of $\text{Fe}(\text{OH})_3$ particles on EG with different pH have no obvious change. This demonstrates alkaline solution is helpful for the generation of $\text{Fe}(\text{OH})_3$ particles.

From the CV curves in Fig. 4-4, it can be seen EG-F with pH around 2-3 shows a good cycle stability compared with other EG-F ($\text{pH}=9, 11$). Because more $\text{Fe}(\text{OH})_3$ particles cover on the surface of EG when $\text{pH}=9$ and 11 (Fig. 4-3). It is easy for $\text{Fe}(\text{OH})_3$ particles to enter electrolyte without the cover of carbon layer. For EG-F with pH around 2-3, the number of $\text{Fe}(\text{OH})_3$ particles are smaller and the layered structure of EG could prevent most of them from dropping down on surface of EG.

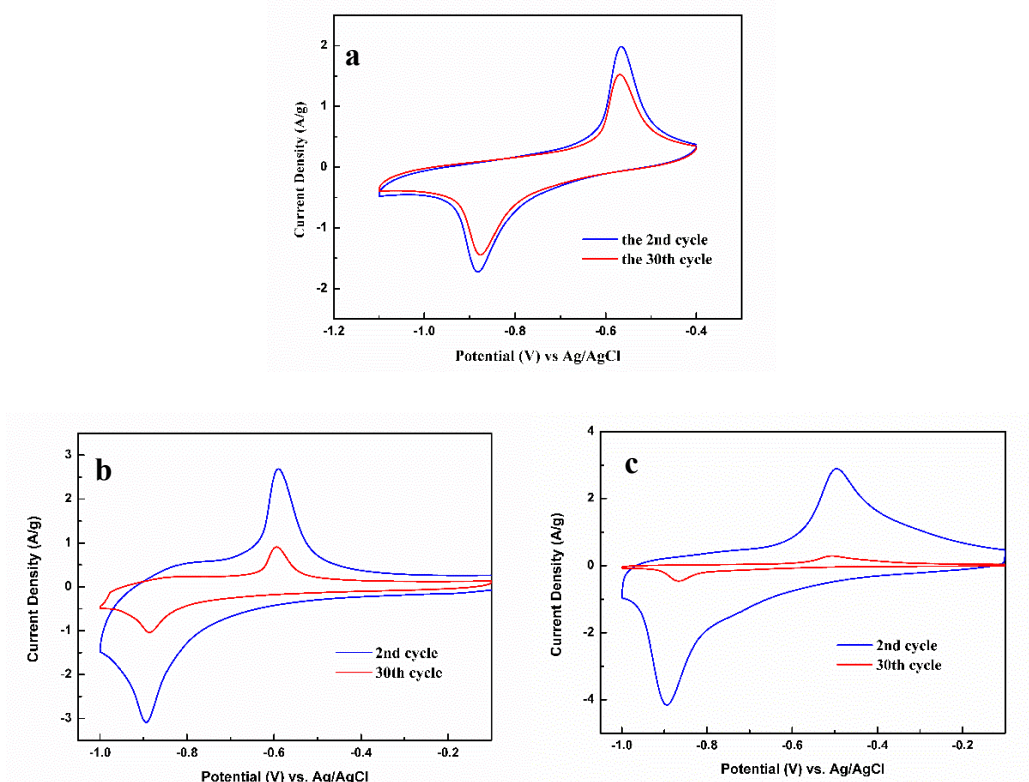


Fig. 4-4 CV curves of EG-F with (a) $\text{pH}=2.7$, (b) $\text{pH}=9$ and (c) $\text{pH}=11$ at 20 mV/s in 1 M KOH .

4.3.2 Comparison of EG and AEG

Fig. 4-5 shows SEM images of EG and AEG, it indicates that the worm-like structure of EG was separated into layered structure with thickness of 40-50nm. Because the acid treatment with concentrated sulfuric and nitric acid introduced more oxygen groups by oxidation effect of strong acid, like O=C-OH, C-OH, especially on the edge of EG, which can enhance the interaction between oxygen functional groups and solution and further separate the worm-like structure to become layered structure as illustrated in Fig. 4-5b.

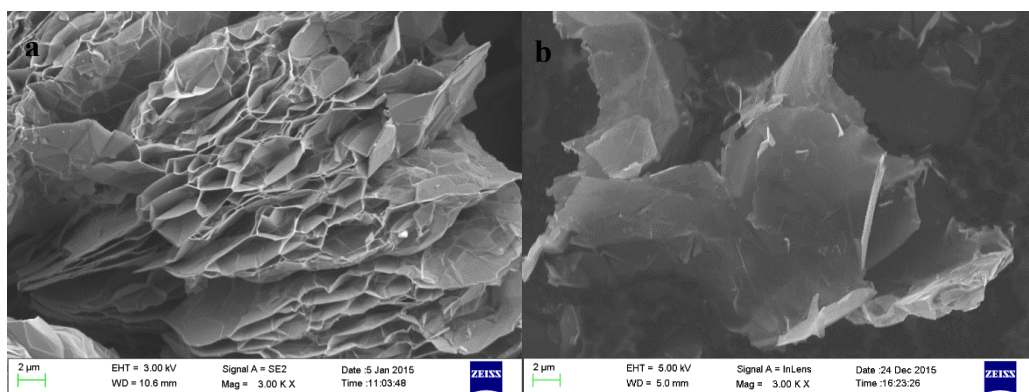


Fig. 4-5 SEM images of (a) EG and (b)AEG.

Fig. 4-6a, b show CV curves of EG, AEG, EG-F and AEG-F. It can be seen that the products of EG-F and AEG-F show obvious redox peaks within the potential window from -0.4 to -1.0V (vs. Ag/AgCl) at a scan rate of 20 mV/s, while EG and AEG only show rectangle-like shape and no obvious sharp peaks are observed. Based on the shape of CV curves, EG and AEG perform capacitor properties while EG-F and AEG-F show visible redox peaks which mean redox reaction happened in the scanning process. The similar peaks also were observed in previous work on iron oxide electrodes (Wang et al. 2014). The redox peaks correspond to the redox reaction between ferrous and ferric

ions which also indicate the existence of iron ions on the surface of EG-F and AEG-F. The GCD curves shown in Fig. 4-6c demonstrates the redox reaction happened due to the plateaus in the corresponded potential range which is match with potential of redox peaks of CV curves. It is well known that the specific capacitance is proportional to the average area of CV curves, the area of CV curves of AEG-F is much larger than that of EG-F. it was believed that AEG was treated by concentrated acid which usually used to oxidize carbon materials could introduce more oxygen functional groups, and EG only have little oxygen functional groups after Fenton reaction, AEG have more negatively charge functional groups and easily reacted with the positively charged iron ions. What is more, the worm-like structure also limited the further contact between EG and iron ions during the Fenton reaction process, while the layered structure of AEG with more oxygen functional groups is easy to react with iron ions. Hence, more $\text{Fe}(\text{OH})_3$ generated on the surface of AEG (Qi et al. 2013). That is the reason that AEG-F have higher capacity than that of EG-F.

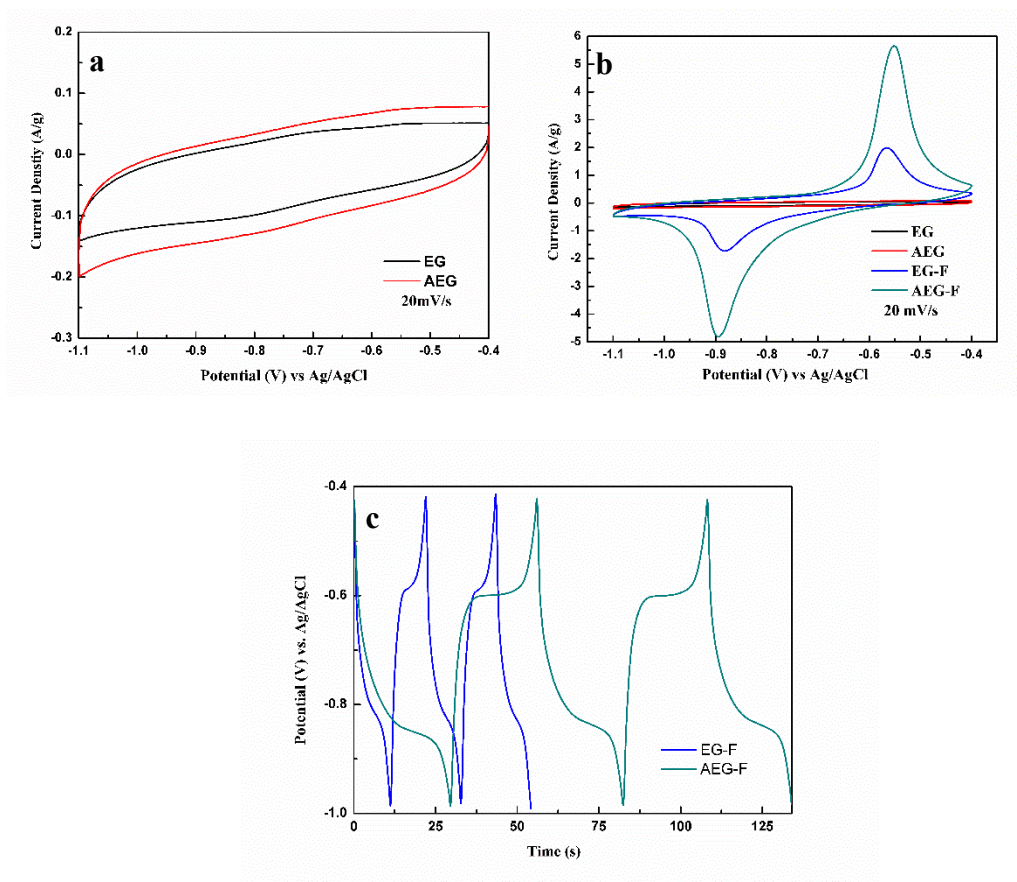


Fig. 4-6 CV curves of (a) EG, AEG and (b) EG-F, AEG-F at a scan rate of 20 mV/s in 1 M KOH, and (c) GCD curves of EG-F and AEG-F in the same electrode system at 1A/g.

As shown in Fig. 4-7, the cathodic and anodic current located in the peaks of CV curves of EG-F and AEG-F are much larger than that for EG-F after 30th cycle and for AEG-F after 50th cycle. The average current of cathodic and anodic current is reduced to 77.94% for EG-F after 30 cycles and 77.63% for AEG-F after 50 cycles. Therefore, the cycling performance of AEG-F is much better than that of EG-F. which is ascribed to that previous acid treatment and layered structure of AEG prevent $\text{Fe}(\text{OH})_3$ nanoparticles from peeling off on the surface of AEG. However, the cycling performance of these two active materials are not good enough, the thickness of graphene nanosheets is still too large, some $\text{Fe}(\text{OH})_3$ nanoparticles just loaded on the

surface of EG and AEG and hardly enter into the layer of graphene nanosheets. Hence, the $\text{Fe}(\text{OH})_3$ nanoparticles easily contact with electrolyte and dissolve into electrolyte and the $\text{Fe}(\text{OH})_3$ nanoparticles also not well uniformly loaded on the surface of EG and AEG (see Fig. 4-8). It is concluded AEG-F shows higher electrochemical properties than that of EG-F, EG-F-H and AEG-F. due to the reason that AEG is oxidized by concentric H_2SO_4 and HNO_3 with more oxygen functional groups after acid treatment, which could reacted with more iron ions and finally formed $\text{Fe}(\text{OH})_3/\text{AEG}$.

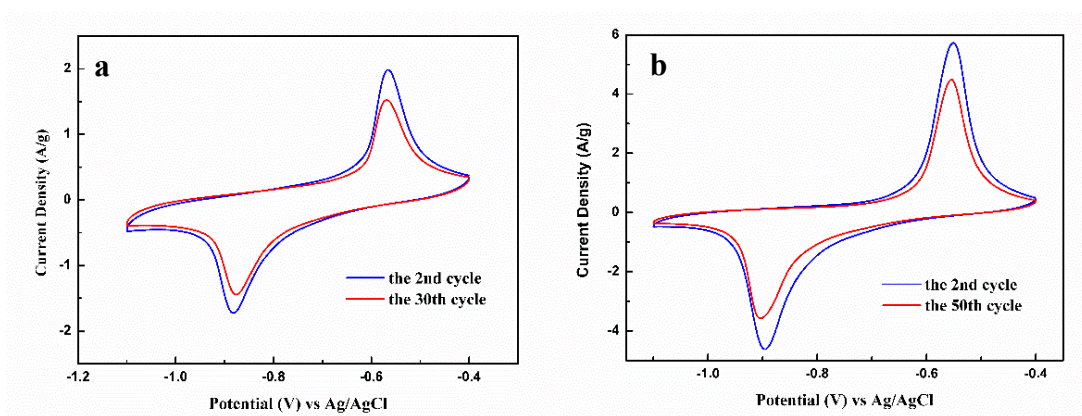


Fig. 4-7 CV curves of (a) EG-F and (b) AEG-F in 1M KOH at a scan rate of 20mV/s. (Pt wire as counter electrode).

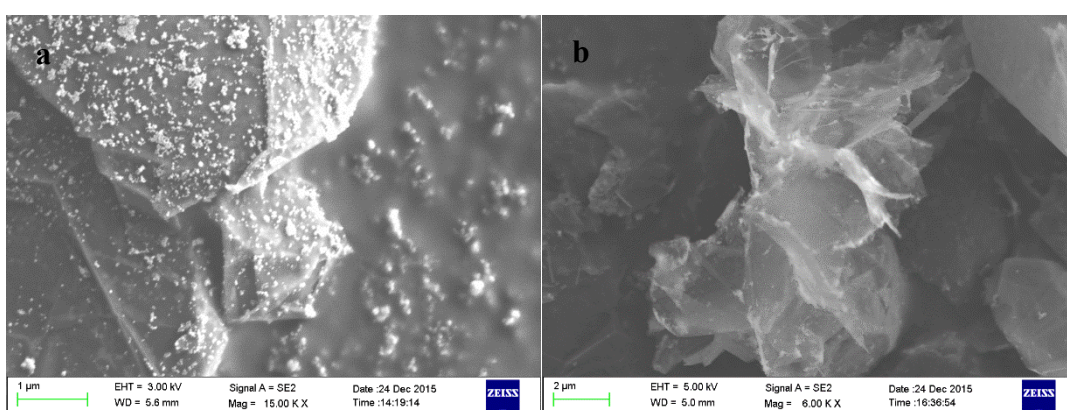


Fig. 4-8 SEM images of (a) EG-F and (b) AEG-F.

4.3.3 Comparison of EG and MWCNTs

As shown in Fig. 4-9, the area of CV curves of MWCNTs-F is much larger than that of MWCNTs-F-H, EG-F and EG-F-H at 20mV/s, indicating that the capacity of MWCNTs-F is higher than that of other three samples. Compared with EG-F, due to the network which not only easily react with Fenton reagent to introduce more oxygen function groups, but also provide an inner electron path way for electron transportation. Hence, MWCNTS-F shows a higher capacity than that of EG-F. In the SEM images in Fig. 4-10, it is noticed that small $\text{Fe}(\text{OH})_3$ nanoparticle with diameter smaller than 100nm on the surface of MWCNTs in the image of MWCNTs-F (Fig. 4-10a), while some well crystallized $\text{Fe}(\text{OH})_3$ particles with diameter around 200nm located between the wrapped MWCNTs in the SEM image of MWCNTs-F-H (Fig. 4-10b). The size of $\text{Fe}(\text{OH})_3$ nanoparticle of MWCNTs-F-H is a little larger than that of MWCNTs-F, indicating the speculation that during the hydrothermal process, $\text{Fe}(\text{OH})_3$ nanoparticles become larger.

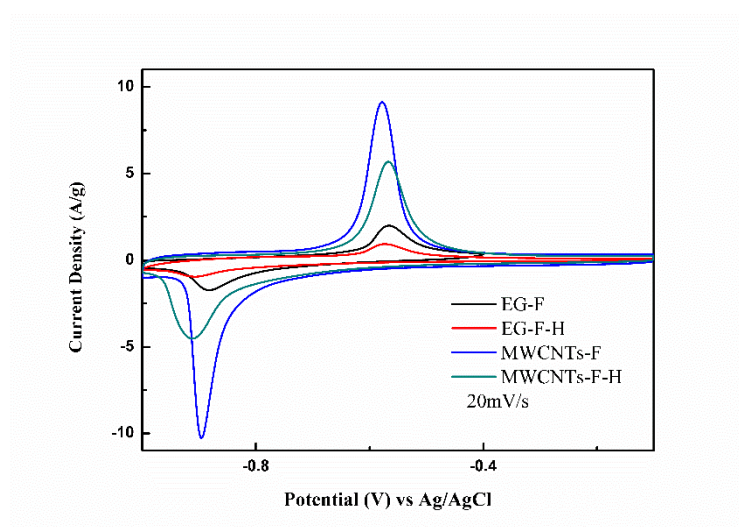


Fig. 4-9 CV curves of sample EG-F, EG-F-H, MWCNTs-F, MWCNTs-F-H in 1M KOH at 20 mV/s (Pt wire as counter electrode).

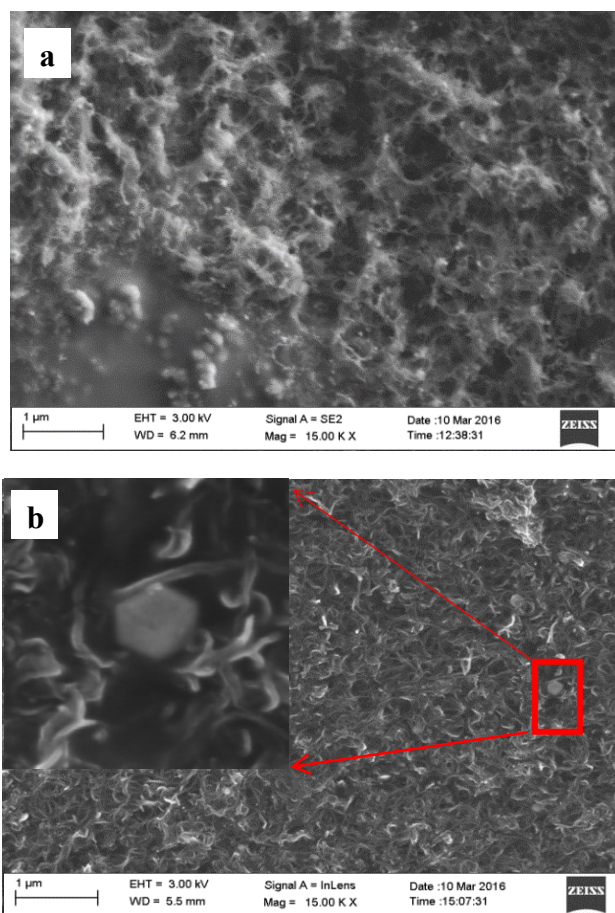


Fig. 4-10. SEM images of (a) MWCNTs-F and (b) MWCNTs-F-H.

As observed in Fig. 4-11, the CV curves of raw MWCNTs show small bumps at -0.6 and -0.89 V (vs. Ag/AgCl), and two sharp redox peaks of MWCNTs-F and MWCNTs-F-H are also located nearby these two positions with a little shift. And the CV curves of MWCNTs and MWCNTs-F are well matched with GCD curves of these two products shown in Fig. 4-12. Because of that the charge and discharge process of MWCNTs is main due to electrostatic phenomenon, that is, the accumulation of the opposite charges on the interface of electrode and electrolyte, which is known as electric double layer capacitance (EDLC). The process of charge and discharge for MWCNTs-F is the combination of redox reaction and double layer charge discharge process, in where a

redox reaction happened. Due to the CV and GCD curves, it is concluded that MWCNTs was oxidized after Fenton reaction, and iron hydroxide was grown on the surface of MWCNTs or wrapped by MWCNTs. And after hydrothermal reaction, partial of iron hydroxide was dissolved into the solution from the surface of MWCNTs and the part of the left iron hydroxide become bigger than that of MWCNTs-F during the hydrothermal process which decreased the surface area between electrode and electrolyte. Hence, MWCNTs-F shows higher capacitance than that of MWCNTs-F-H.

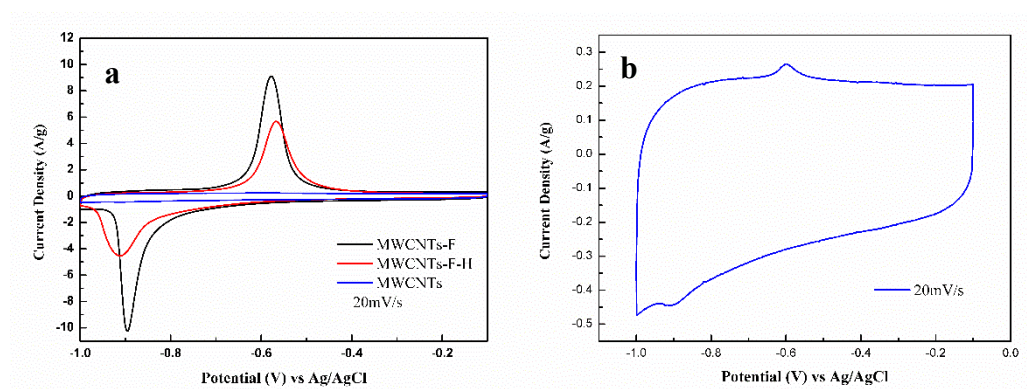


Fig. 4-11 CV curves of (a) MWCNTs, MWCNTs-F, MWCNTs-F-H and (b) CV curves of MWCNTs in 1M KOH at 20 mV/s (Pt wire as counter electrode).

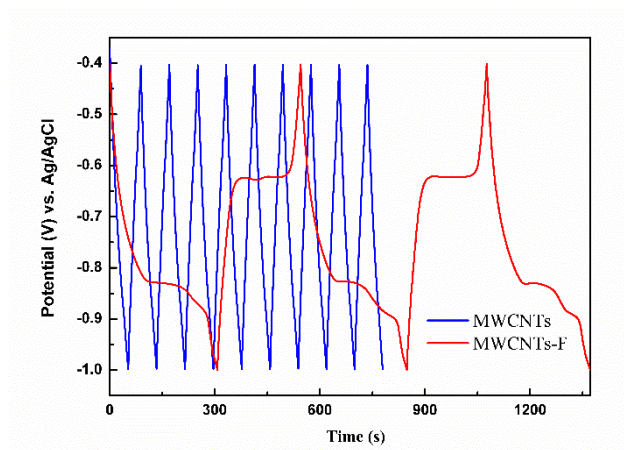


Fig. 4-12 GCD curves of MWCNTs and MWCNTs-F in 1M KOH at 1A/g (Pt wire as counter electrode).

4.3.4 The Sonication Time Influence on Cycling Performance

During the Fenton reaction, sonication was used to assist and promote the Fenton reaction. Here, sonication time was optimized based on the electrochemical stability of products.

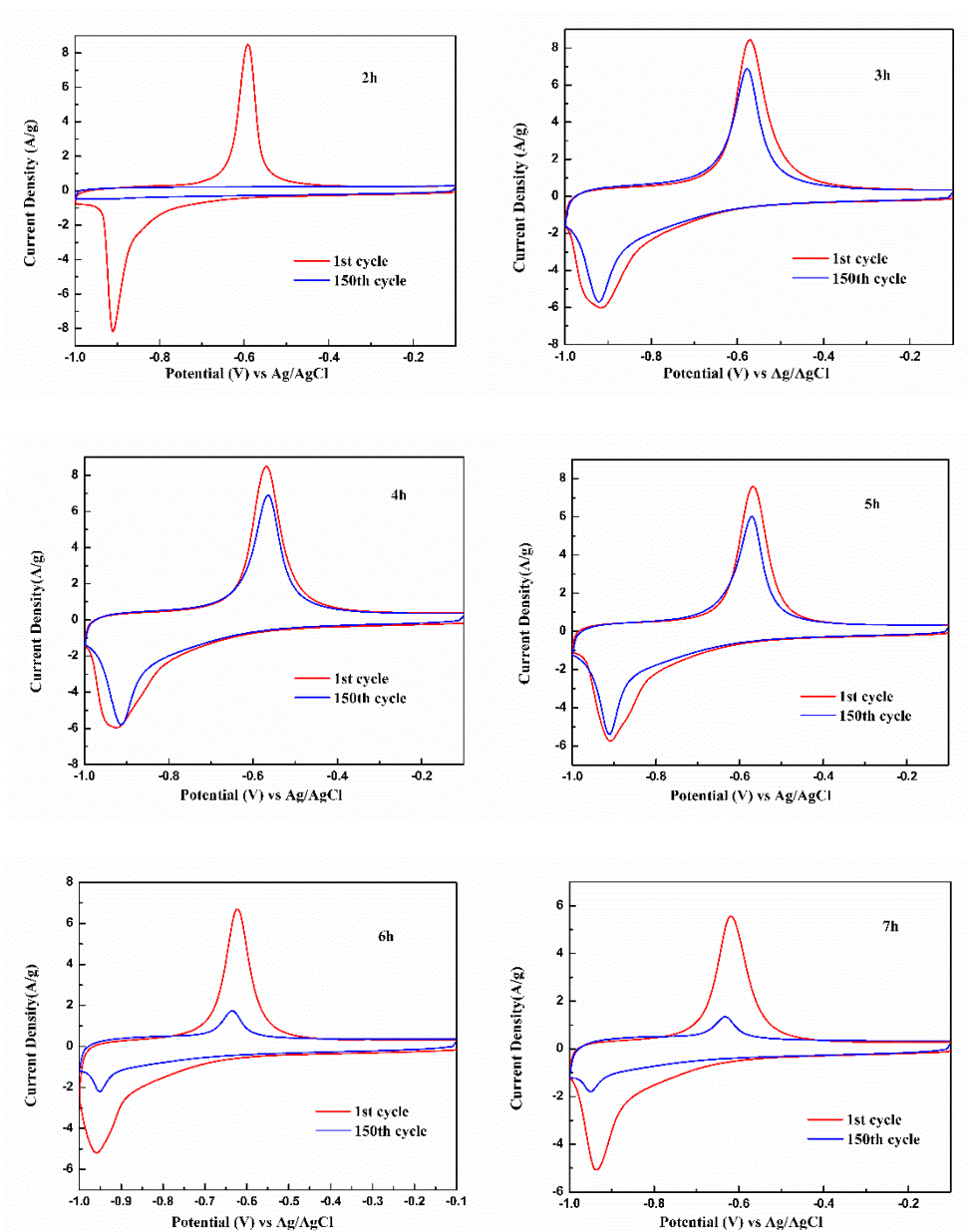
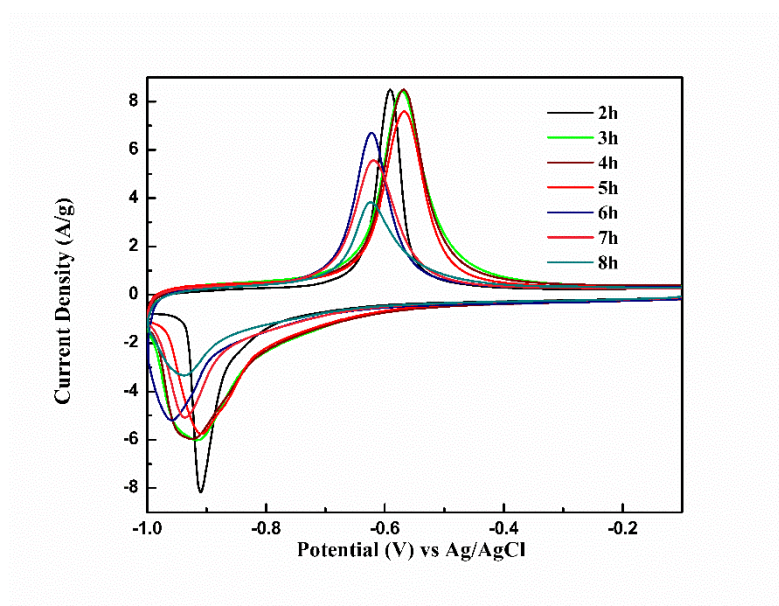


Fig. 4-13 CV curves of the first cycle and the 300cycle of MWCNTs-F prepared at different sonication time 2h, 3h, 4h, 5h, 6h, 7h.



**Fig. 4-14 CV curves of the first cycle of MWCNTs-F prepared at different sonication time
2h, 3h, 4h, 5h, 6h, 7h, 8h.**

In Fig. 4-13 and 4-14, the current densities of MWCNTs-F sonicated at 2h, 3h, 4h are larger than the current densities of MWCNTs-F sonicated at 5h, 6h, 7h, 8h. It is speculated that the long-time sonication breaks the tube structure of MWCNTs and also decrease the length of MWCNTs. The broke structure exposes more active sites, and hence introduce more oxygen functional groups covered on the surface of MWCNTs in the process of Fenton reaction. The decreased length structure of MWCNTs and more oxygen functional groups decrease the conductivity of composite. Therefore, the current densities of MWCNTs-F sonicated at long time are not good as that of MWCNTs-F prepared at short sonication time. However, the cycling performance of MWCNTs-F synthesized at different sonication time is not consistent with the current densities of them. When the sonication time is 3 or 4h, the current densities decrease smaller compared with others. It is ascribed to that the longer MWCNTs could wrap the $\text{Fe}(\text{OH})_3$ nanoparticles, and after long-time sonication, the length of MWCNTs

decreased which cannot protect $\text{Fe}(\text{OH})_3$ nanoparticles from peeling off on MWCNTs. When the sonication time was 2, only few oxygen functional groups generated on the WMCNTs, the MWCNTs cannot have strong interaction with $\text{Fe}(\text{OH})_3$ nanoparticles after many cycles. Hence, the cycling performance of MWCNTs-F sonicated for 2h is the worst. Considering the cycling performance of MWCNTs with different sonication time, the optimized sonication time is 3h.

4.4 Conclusion

In this work, EG, AEG, MWCNTs were used to prepare composites of $\text{Fe}(\text{OH})_3$ /carbon materials by Fenton reaction. After the preparation and electrochemical test, it is concluded that compared with EG-F, AEG-F show high capacitance due to the previous concentrated acid treatment which could introduce more oxygen functional groups reacted with iron ions and hence, more of $\text{Fe}(\text{OH})_3$ nanoparticles loading on AEG and there are strong interaction between of $\text{Fe}(\text{OH})_3$ nanoparticles and AEG. Compared with EG-F, MWCNTs-F exhibits high capacity because the tube and network structure of MWCNTs make it easily to be oxidized to introduce more oxygen functional groups. And the tube structure of MWCNTs provides an inner path way for electron transportation. And the length structure wrapped $\text{Fe}(\text{OH})_3$ nanoparticles could impede the peeling off $\text{Fe}(\text{OH})_3$ nanoparticles from the surface of MWCNTs and improve the cycling performance of MWCNTs-F. Sonication is used to assist and accelerate the Fenton reaction. The optimized sonication time is 3h based on the cycling performance of MWCNTs-F when considering the time and electric energy consumption.

Chapter 5 Scalable Preparation of Fe₂O₃/MWCNTs by Fenton

Reaction and Their Application in LIBs

5.1 Introduction

In this chapter, composite of Fe₂O₃/MWCNTs was synthesized by Fenton reaction with a precipitation process. The detailed preparation process was introduced in the following section. The composite was characterized by XRD, SEM, TEM *etc.*, their electrochemical properties as anode materials in LIBs were measured by land test, CHI, Autolab, *etc.*.

5.2 Experimental Section

5.2.1 Preparation of Material of Fe₂O₃/MWCNTs

Firstly, 150mg MWCNTs were dispersed in 300mL DI water and sonicated for 30min to obtain well-dispersed MWCNTs suspension. Then, 705.6mg FeSO₄·7H₂O was added into the MWCNTs suspension following 30min stirring at room temperature. After that, 80ml H₂O₂ was added into the mixture and sonicated for 3h. Finally, the suspension was filtered and washed by DI water until the pH of the solution was 7 and then the filtered product was dried in an oven at 60°C for overnight. After drying, the product was heated at 200°C for 3h to make sure that Fe(OH)₃ has totally convert to Fe₂O₃.

5.3 Materials Characterization

5.3.1 SEM and TEM

The morphology of Fe₂O₃/MWCNTs was performed by SEM and TEM images (see Fig. 5-1a, b, c). SEM image shows that Fe₂O₃ nanoparticles coated on the surface of MWCNTs and few of Fe₂O₃ nanoparticles aggregated together due to the high surface energy of nanoparticles, but most of them were anchored on the surface of MWCNTs because of the interaction between MWCNTs and Fe₂O₃ nanoparticles caused by the oxygen functional groups which was introduced by Fenton reaction. As shown in Fig. 5-1b, black particles is Fe₂O₃ and the long, curved tube is MWCNTs. It can be observed from Fig. 5-1b and 1 c that partial of Fe₂O₃ nanoparticles locate in the tube of MWCNTs and this demonstrates that the walls of MWCNTs were partially destroyed during the Fenton reaction process. The inset SAED pattern shows a broad diffraction ring which typically indicates that Fe₂O₃ has an amorphous structure (Li et al. 2013). From the high resolution TEM images (Fig. 5-1c), the distance of the layer is 0.34nm corresponding to the (002) of MWCNTs, and the distance in the inner of MWCNTs is 0.184nm which is the lattice plane of (024) of Fe₂O₃ and this implies some iron oxide particles embedded into the tube structure of MWCNTs.

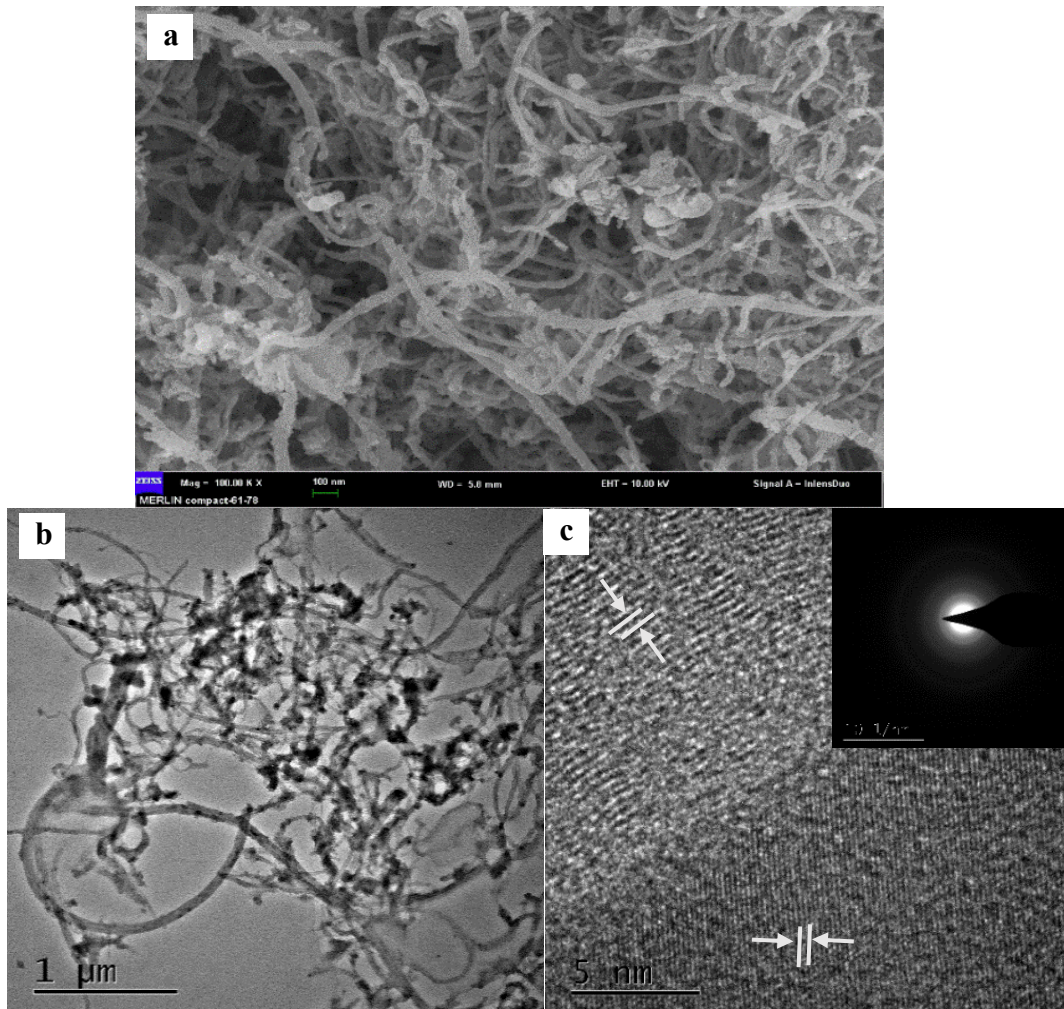


Fig. 5-1 (a)SEM image, (b) TEM image and (c) high resolution TEM image of $\text{Fe}_2\text{O}_3/\text{MWCNTs}$ (the inset is the corresponding SAED pattern).

5.3.2 XRD

XRD pattern shows that the diffraction peaks located at 24.1, 33.1, 35.6, 40.8, 54.1, 62.4 and 63.9 indexed to (012), (014), (110), (113), (024), (116), (214) and (300) are in agreement with the peaks of $\alpha\text{-Fe}_2\text{O}_3$ (JCPDS #33-0664) (Zhang et al. 2013). However, the product $\text{Fe}_2\text{O}_3/\text{MWCNTs}$ only have two peaks related to MWCNTs which positioned at 26, 42 corresponding to the (002), (100), this further prove that the

structure of Fe_2O_3 in the product of $\text{Fe}_2\text{O}_3/\text{MWCNTs}$ is amorphous which is consistent with the result of SAED pattern.

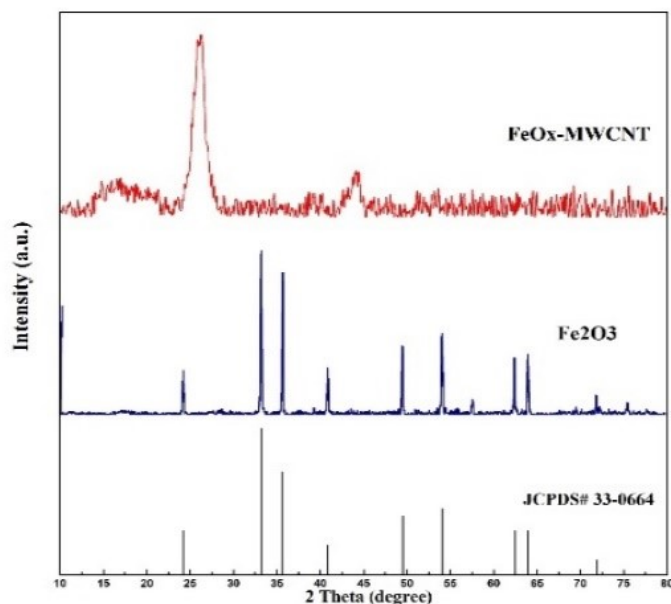


Fig. 5-2 XRD pattern of $\text{Fe}_2\text{O}_3/\text{MWCNTs}$ and Fe_2O_3 .

5.3.3 FT-IR

To investigate the organic functionalities and chemical composition of MWCNTs after Fenton reaction with acid treatment (washed by 1M H_2SO_4 solution and then water), FT-IR was applied to study the oxygen functionalities. Fig. 5-3 is the FT-IR spectrum of MWCNTs after Fenton reaction washed by acid and water and $\text{Fe}_2\text{O}_3/\text{WMCNTs}$. It can be clearly shown that the broad and obvious absorption peak located around 3434cm^{-1} proves the hydroxyl groups (-OH), and the density of that peak of $\text{Fe}_2\text{O}_3/\text{WMCNTs}$ is much larger than that of MWCNTs after Fenton reaction with washing by acid, since the nanoparticles of Fe_2O_3 could adsorb a great of hydroxyl groups on their surface. And the existence of hydroxyl in MWCNTs after Fenton reaction indicates that MWCNTs was oxidized in the process of Fenton reaction. The

absorption peaks located at 1633, 1390 and 1045 cm^{-1} relate to the vibration of C=C, C-H and C-O respectively (Yang et al. 2013, Guo et al. 2013, Lee et al. 2013). The peaks positioned at 667 corresponding to metal-oxygen (Fe-O) stretching indicate the presence of Fe_2O_3 (Ren et al. 2016, Chaudhari and Srinivasan 2012).

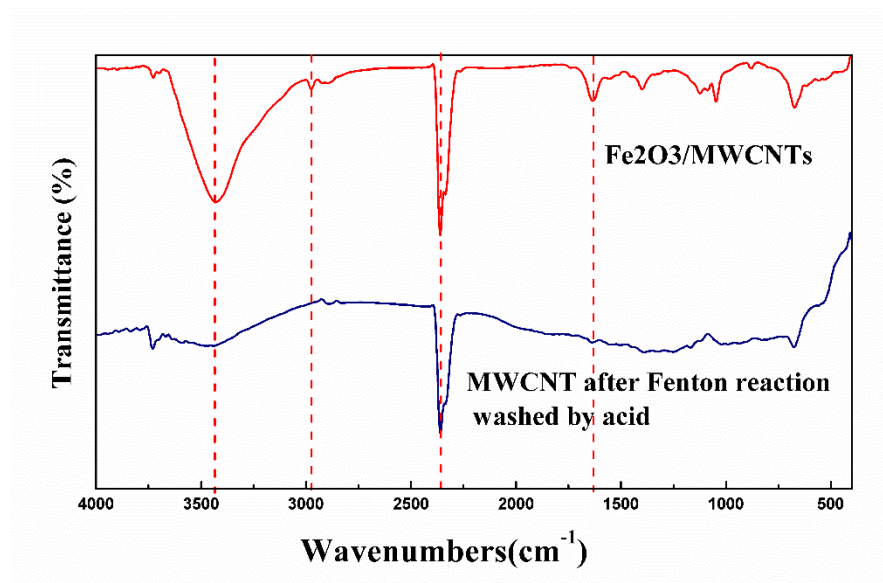


Fig. 5-3 FT-IR spectrums of $\text{Fe}_2\text{O}_3/\text{MWCNTs}$ and MWCNTs after Fenton reaction washed by acid.

5.3.4 N_2 Adsorption-Desorption Measurement

N_2 adsorption-desorption measurement was used to measure the surface area of $\text{Fe}_2\text{O}_3/\text{MWCNTs}$ and MWCNTs (Fig. 5-4). The isotherms display typical IV isotherm lines which show typical property of mesoporous materials, verifying that $\text{Fe}_2\text{O}_3/\text{MWCNTs}$ and MWCNTs have mesoporous structure, due to the network structure. They have classical H3 hysteresis loops at relative high pressure which usually caused by non-rigid aggregation by the plate-like particles. Here, it is caused by the multiwall of MWCNTs. The specific surface area S_{BET} was calculated by BET

method, The S_{BET} of $\text{Fe}_2\text{O}_3/\text{MWCNT}$ is $62.21\text{m}^2/\text{g}$ and it is smaller than that of MWCNTs ($132.74\text{m}^2/\text{g}$). The reason is that Fe_2O_3 nanoparticles on the surface or located in the tube cover and occupy the surface area and pores of MWCNTs. Hence, the S_{BET} of $\text{Fe}_2\text{O}_3/\text{MWCNT}$ s is smaller after Fenton reaction (Penki et al. 2015).

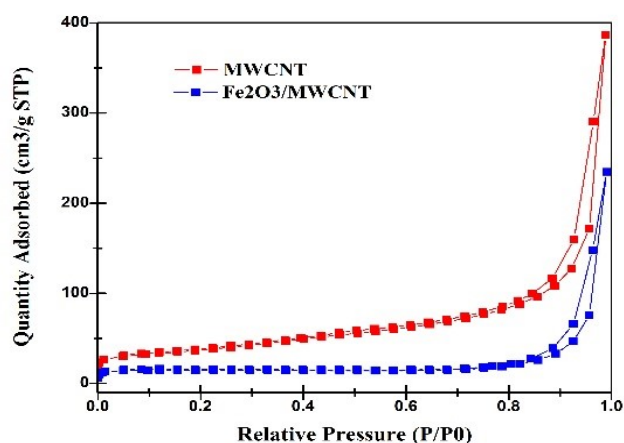


Fig. 5-4 N_2 -adsorption/desorption isotherms of $\text{Fe}_2\text{O}_3/\text{MWCNT}$ s and MWCNTs.

5.3.5 XPS

XPS was applied to investigate the chemical and valence states of $\text{Fe}_2\text{O}_3/\text{MWCNT}$ s. As shown in Fig. 5-5a, the XPS spectrum represents the existence of Fe, C, O elements. The high resolution of Fe 2p XPS spectrum shown in Fig. 5-5b reveals that it is deconvoluted into four peaks, and the binding energy peaks located at 711.5eV and 725.5eV stand for $\text{Fe}2p_{3/2}$, $\text{Fe}2p_{1/2}$, respectively, the other two peaks positioned at 719.1eV and 733.8eV represent the related shakeup satellites of $\text{Fe}2p_{3/2}$ and $\text{Fe}2p_{1/2}$. This implies that the valence of oxidized Fe is mostly 3. The C 1s spectrum in Fig. 5-5c was fitted into three peaks which reveals the presence of C=C, -C-O, and -O-C=O positioned at 284.3 eV, 285.7 eV, 290 eV, respectively (Park et al. 2018). The

high resolution O1s spectra shown in Fig. 5-5d are deconvoluted into three peaks, representing the oxygen bond of metal oxide (530 eV), metal hydroxide (531.4 eV) and H-O-H (532.9eV) (Lu et al. 2015).

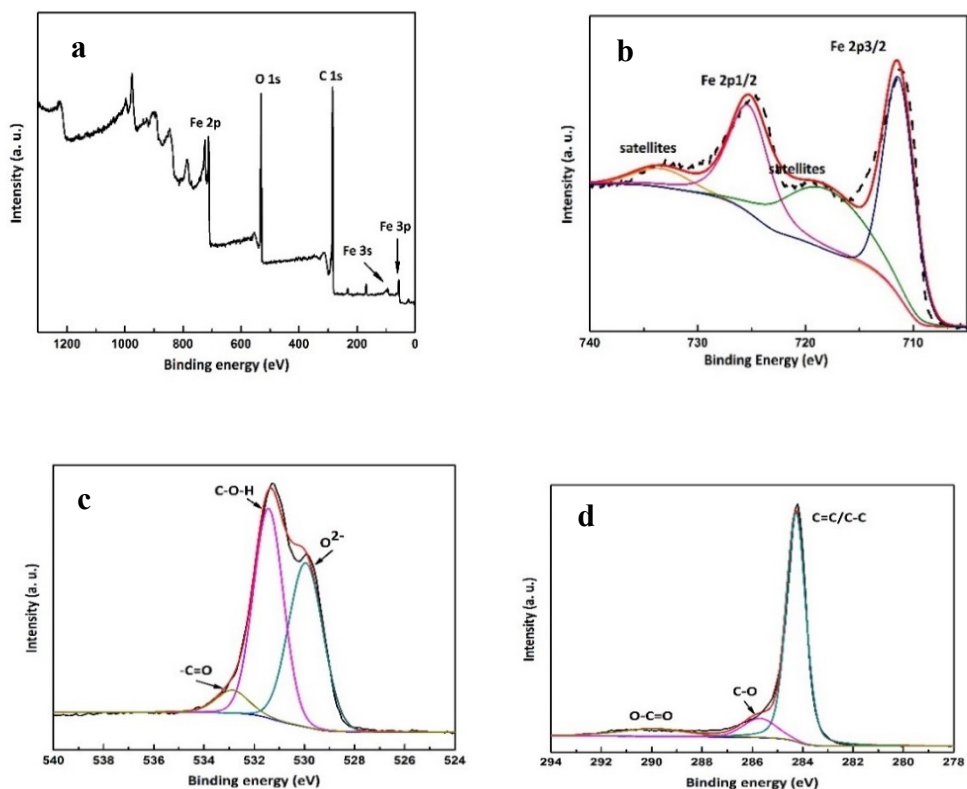


Fig. 5-5 XPS spectrum of (a) $\text{Fe}_2\text{O}_3/\text{MWCNTs}$ and high-resolution spectra of (b) Fe 2p, (c) C 1s and (d) O 1s.

5.4 Electrochemical Test

5.4.1 CV

The electrochemical performance of $\text{Fe}_2\text{O}_3/\text{MWCNTs}$ as anode material in LIBs was discussed in the following section. The half-cell was assembled by $\text{Fe}_2\text{O}_3/\text{MWCNTs}$ as anode or working electrode, Li foil as reference and counter electrode. Fig. 5-6a shows

CV curves of Fe₂O₃/MWCNTs which was scanned at a scan rate of 0.05 mV/s in the range of 0.01-3.0 V. As shown in Fig. 5-6a, two peaks are observed at about 1.3 V and 0.55 V in the first cathodic cycles, which implies a solid-solution-like compound was formed (1.3 V) during the process of insertion of Li ions into the amorphous Fe₂O₃ and Fe³⁺ is reduced to Fe⁰ at the potential of 0.55 V (Jiang et al. 2014, Huang et al. 2016). That is, a few parts of lithium insert into the amorphous structure of Fe₂O₃, and Fe²⁺ is reduced to Fe⁰ at last. In the anodic process, two anodic peaks located at 1.5V and 2.3 V demonstrate that the Fe⁰ is oxidized to Fe²⁺ and then Fe³⁺ (Chaudhari et al. 2013). It is obviously noticed that the peaks intensity decrease in the 2nd cycle compared to the 1st cycle. The significant reduction in the first two cycles is attributed to the inevitable formation of solid electrolyte interface (SEI) film and decomposition of electrolyte (Wang, Wang and Wang 2015). There is no obvious change after the second cycle for composite of Fe₂O₃/MWCNTs, indicating that composite of Fe₂O₃/MWCNTs has good capacity retention and structural stability. As shown in Fig. 5-6b, the cathodic peaks of commercial Fe₂O₃ located around 0.4 V is ascribed to the formation of SEI layer, after the second cycle, the cathodic peak around 0.7 and anodic peak around 1.7-2.3V indicate the reversible conversion reaction between Fe²⁺ to Fe⁰.

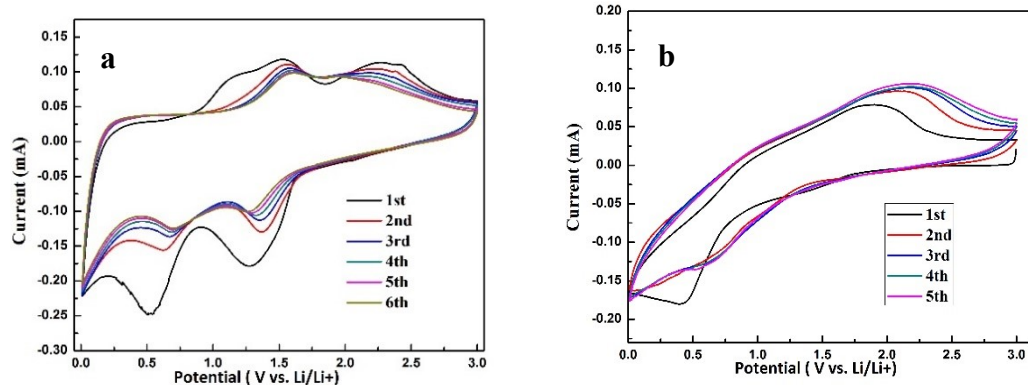


Fig. 5-6 (a) CV curves of Fe₂O₃/MWCNTs and (b) Fe₂O₃ at 0.05 mV/s.

5.4.2 GCD

The GCD curves of Fe₂O₃/MWCNTs at a current density of 100 mA/g in the voltage range of 0.01 to 3 V are shown in Fig. 5-7a. The initial discharge and charge capacities of Fe₂O₃/MWCNTs are 1914 and 1893 mAh/g, and the plateau of discharge curves around at 0.8 V-1.0 V is due to the reduction of Fe³⁺ to Fe⁰, and the charge plateau at 1.5-2.2 V indicates the oxidization of Fe⁰, they are well matched with the CV curves shown in Fig. 5-6a (Cai et al. 2017a). Fig. 5-7b is the GCD curves of commercial Fe₂O₃. The first initial discharge capacity is 1302 mAh/g, while the first charge capacity is 746.2 mAh/g, the columbic efficiency is only 57.2%. The low columbic efficiency is due to the irreversible loss of capacity caused by the side reaction between electrode and electrolyte, and the significant volume change during the charge-discharge process without the protecting of carbon matrix. The high efficiency and reversible capacity of Fe₂O₃/MWCNTs is attributed to the amorphous structure with small size which buffers the volume change and increases the contact surface area between electrode and

electrolyte. The MWCNTs substrate not only enhances the conductivity of Fe_2O_3 , but also prevents the pulverization of Fe_2O_3 during the reaction process.

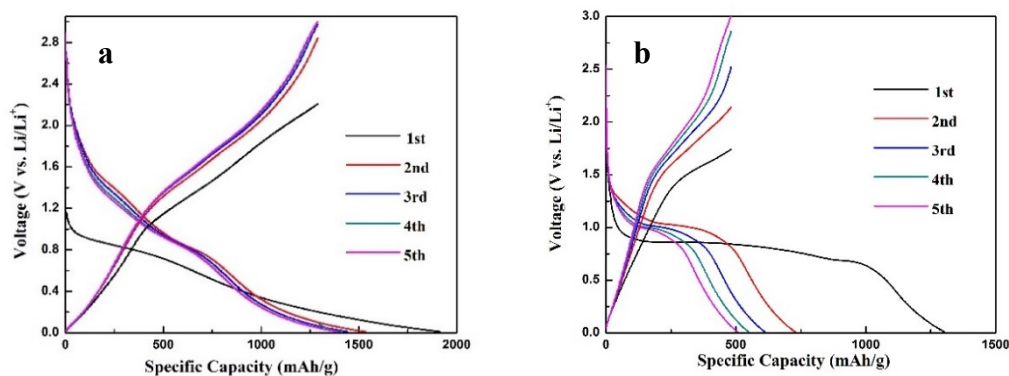


Fig. 5-7 GCD curves of (a) $\text{Fe}_2\text{O}_3/\text{MWCNTs}$ and (b) Fe_2O_3 at 100 mA/g.

5.4.3 Cycling Performance and Rate Capability

To evaluate the cycle stability of $\text{Fe}_2\text{O}_3/\text{MWCNTs}$, the cycling performance was studied at a current density of 500 mA/g (0.5 C) from 0.01V to 3V as shown in Fig. 5-8a. Firstly, the material should be activated at a current density of 100mA/g (0.1 C) for the first 6 cycles to stabilize the material. After the 6 cycles activation, the discharge and charge capacity of $\text{Fe}_2\text{O}_3/\text{MWCNTs}$ firstly decreases and then increases followed with stable steps. In the initial cycles which performs increased capacity, the columbic gradually close to 99, even to 100%, it implies that the activated process is finished in a slow process, and the irreversible decomposition of electrolyte happen slowly in this process. In the increasing process of capacity, it is suggested that the decomposition of electrolyte also forms a reversible organic polymeric/gel-like layer which could generated a ‘pseudo-capacitance-type’ behaviour and the size of electroactive material is reduced by the repeated volume expansion in the process of cycling and hence

facilitates the contact surface area between electrode and electrolyte. And this behaviour contributes parts of capacity to the increased capacity (Li et al. 2015, Wang et al. 2012, Fang et al. 2018). Last, the capacity keep stable at 900 mAh/g at a current density of 500 mA/g after 500cycles which indicates that the composite has a good cycling performance.

The rate capability is one of the most critical qualifications for LIBs. Fig. 5-8b displays the rate performances of Fe₂O₃/MWCNTs and Fe₂O₃ at current densities of 100, 200, 500, 1000, 2000 mAh/g. the average discharge capacity of Fe₂O₃/MWCNTs at every current density were 1435, 1066, 979, 896, 785 mAh/g respectively. And when the current density returns to 0.1C, the capacity is recovered to 1341 mAh/g, this indicates that the materials could be maintained stable even under a high current density and the composite performs an excellent conductivity and kinetic. Compared with the capability of Fe₂O₃, the capacities of Fe₂O₃/MWCNTs are larger at all the current densities, and after 30 cycles, it recovers to the similar capacity value of initial cycle and keep stable after 100 cycles, while the capacity of Fe₂O₃ are not well recovered and after 30 cycles. This is ascribed to the random ordered amorphous structure and the conductivity support of MWCNTs (Jiang et al. 2014, Huang et al. 2016).

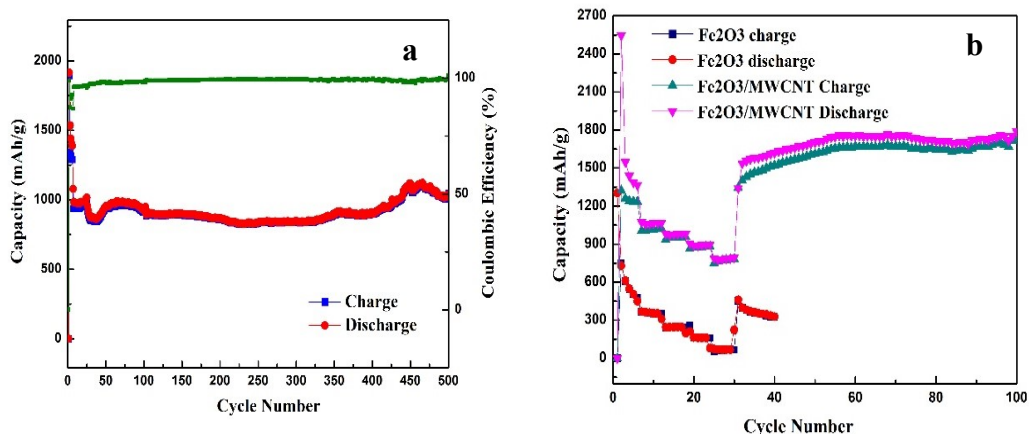


Fig. 5-8 Cycling performance of (a) $\text{Fe}_2\text{O}_3/\text{MWCNTs}$ at 500mA/g (activated at first 6 cycles under 100mA/g) and (b) rate capacity of $\text{Fe}_2\text{O}_3/\text{MWCNTs}$ and Fe_2O_3 at different charge-discharge rate from 0.1C to 2C , each rate was used for 6 cycles.

5.4.4 EIS

In order to further explore the electrochemical performance, EIS measurement was applied for $\text{Fe}_2\text{O}_3/\text{MWCNTs}$ before the charge-discharge and after 500 cycles of charge-discharge and Fe_2O_3 . Nyquist plots are shown in Fig. 5-9. In the middle frequency, the semicircle is related to the charge transfer resistance (R_{ct}) and interfacial resistance. The slope of the straight line in low frequency is associated with the Warburg (Z_w) which is assigned to the transport and diffusion of Li^+ ion from electrolyte to the electrode (Cai et al. 2017a). As Fig. 5-9a shown, the diameter of semicircle in the middle frequency of $\text{Fe}_2\text{O}_3/\text{MWCNTs}$ after 500 cycles of charge-discharge is smaller than that of $\text{Fe}_2\text{O}_3/\text{MWCNTs}$ before charge-discharge, it is proposed that the charge transfer resistance is smaller after 500 cycles due to the milling effect during the repeated process of lithium insertion/extraction, which causes the smaller sized nanoparticles and hence increases the contact active surface area. The decreased Li^+ ion

transportation and diffusion are ascribed to that the SEI film become thicker and thicker during the reaction process (Hao et al. 2016, Liu et al. 2015b). Compared with Fe_2O_3 , the $\text{Fe}_2\text{O}_3/\text{MWCNTs}$ has small R_{ct} and Z_w (Fig. 5-9b), because the conductive MWCNTs network which not only impede the aggregation and also provide an electronic path for fast charge transfer, another reason is that the amorphous structure combined with MWCNTs offers reinforced capacitive-like behaviour, that is well matched with the increased and stable cycle performance of $\text{Fe}_2\text{O}_3/\text{MWCNTs}$.

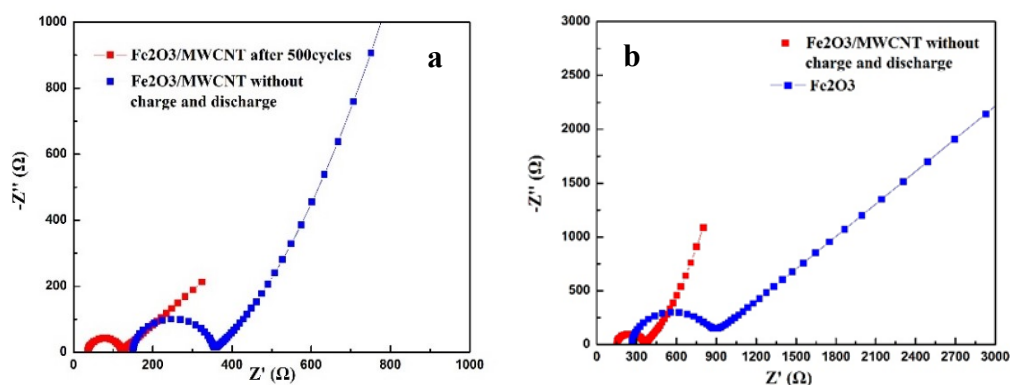


Fig. 5-9 Nyquist plots of $\text{Fe}_2\text{O}_3/\text{MWCNTs}$ before charge-discharge and after 500 cycles charge-discharge (a) and Nyquist plots of $\text{Fe}_2\text{O}_3/\text{MWCNTs}$ and Fe_2O_3 without charge-discharge (b).

5.5 Summary

In this chapter, composite of $\text{Fe}_2\text{O}_3/\text{MWCNTs}$ was prepared by a simple and scalable Fenton reaction process followed with co-precipitation. During the preparation process, no environmentally harmful by-product such as concentric acid commonly used for oxidizing MWCNTs was produced. The XRD and SEM indicate that the structure of Fe_2O_3 in composite of $\text{Fe}_2\text{O}_3/\text{MWCNTs}$ is amorphous. The electrochemical test demonstrates that the composite displays an excellent cycle performance with a

reversible capacity of 900 mAh/g at a current density of 500 mA/g after 500 cycles and a high rate capability of 785 mAh/g at a high current density of 2 A/g. It is ascribed to the random ordered amorphous structure of Fe₂O₃ provides a short ion pathway and the small size of Fe₂O₃ particles buffers the volume change, MWCNTs substrate offers an electronic path way for high charge transfer and improving the rate capability.

Chapter 6 Low-Crystalline NiFe LDHs/MWCNTs Composites Fabricated by Fenton Reaction and Their Application in OER

6.1 Introduction

In this chapter, low-crystalline NiFe LDHs combined with MWCNTs composite was fabricated by facile Fenton reaction and precipitation. Fenton reaction is used to oxidize MWCNTs and provide iron sources. The composite of NiFe LDHs/ MWCNTs was used as electrocatalyst in OER. According to the XRD, TEM test, the NiFe LDHs show low crystalline structure. And the low crystalline structure is beneficial for OER. The electrocatalytic measurement also indicates that the composite of F(3-1)3 (named by molar ratio and total molar of Ni,Fe, explained in the experimental section) shows an excellent electrocatalytic property.

6.2 Experiment Section

6.2.1 Preparation of NiFe LDHs/MWCNTs Composites

Firstly, 150mg MWCNTs was dispersed into 300mL ultra-pure water, and sonicated for 30min by microfluidizer (power: 300w) to obtain a well-dispersed MWCNTs suspension. Then a certain quantity of $\text{FeSO}_4 \cdot 7\text{H}_2\text{O}$ was dissolved in the above mixture and stirred for 30min to make sure the enough contact between ferrous ions and MWCNTs. After then, H_2O_2 was dropped into the mixture followed with another 30min ultra sonication with the same power. Then, $\text{Ni}(\text{NO}_3)_2 \cdot 6\text{H}_2\text{O}$ was added into the above mixture with ammonia until pH reach to 11 and then the mixture was stirred for 6h at room temperature. After washing with ultra-pure water, and drying in oven at 60°C for 12h, the product of NiFe LDHs/MWCNTs composite was obtained. Based on the total

molar and the molar ratio of Ni and Fe, the materials was named as F (molar ratio of Ni and Fe)/total molar (mmol), for example, when the molar ratio of Ni and Fe was 3:1 and the total molar was 3mmol, the prepared material was named as F(3-1)3.

6.3 Material Characterization

6.3.1 SEM and TEM

It can be seen from SEM images that NiFe-LDHs coat on the surface of MWCNTs, and some aggregation of NiFe LDHs also can be observed (Fig. 6-1a). TEM patterns display that most of NiFe LDHs cover on the surface of MWCNTs and few NiFe LDHs exist in the tube of MWCNTs which can be shown in Fig. 6-1c, MWCNTs wrap small NiFe LDHs nanoparticles, and the distance $d=0.23$ labelled in Fig. 6-1c indicates the existence of NiFe LDHs which represents the lattice plane of (015) of NiFe LDHs, and the distance $d=0.34$ means the lattice plane of (002) of MWCNTs. The SAED pattern in the inset of Fig. 6-1b shows a broad halo ring, indicating that NiFe LDHs has low crystalline structure (Lu and Zhao 2015). And it has been demonstrated that disordered and short range could provide more active sites for electrocatalysis. The element mapping shows the exist of Ni, Fe, C, O.

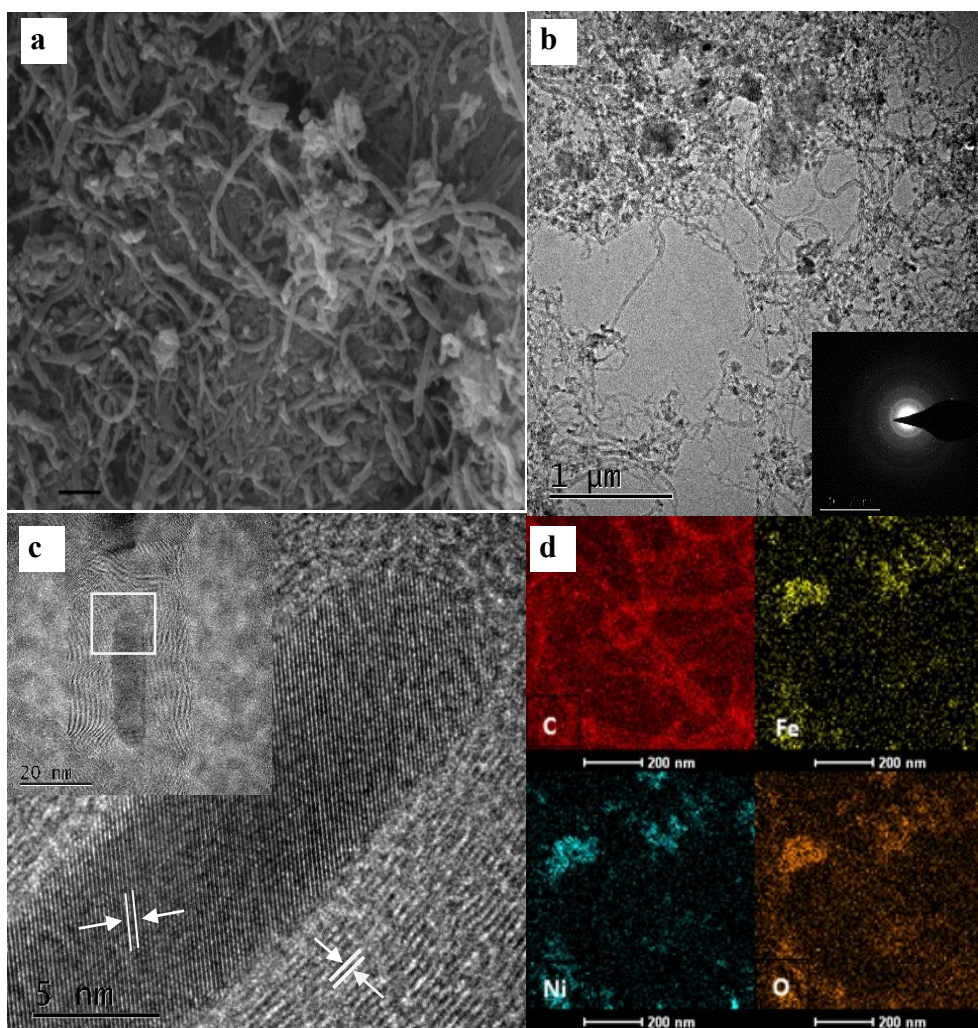


Fig. 6-1 (a) SEM image of F(3-1)3, (b) TEM image of F(3-1)3 (the inset is the SAED patterns), (c) HRTEM image of F(3-1)3 with different scales and (d) EDS element mapping images of F(3-1)3.

6.3.2 XRD

The XRD patterns display the structural information of NiFe LDHs (Fig. 6-2). It can be clearly noticed that obvious diffraction peaks at 26, 42 and 43.7 corresponding to the (002), (100), (101) plane demonstrate that MWCNTs have no noticeable change (Gupta and Saleh 2011). The diffraction peaks at 11.4, 22.9, 33.5, 34.4 and 38.9 indexed to the reflections of (003), (006), (101), (012), (015) is consistent with the XRD pattern

of NiFe LDHs (JCPDS#40-0215). For samples with the molar ratio of 3:1 of Ni: Fe, the intensity of major peaks of NiFe LDHs increase with the increase of total molar. For different molar ratio of Ni and Fe, when the molar ratio is 4:1, apparent XRD peaks of NiFe LDHs is not observed which means when the quantity of Ni increase, ferrous salt used for Fenton reaction was not enough to oxidize MWCNTs and hence, only few NiFe LDHs is generated and located on the surface of MWCNTs during the precipitation process (Zhang et al. 2016b, Hunter et al. 2016).

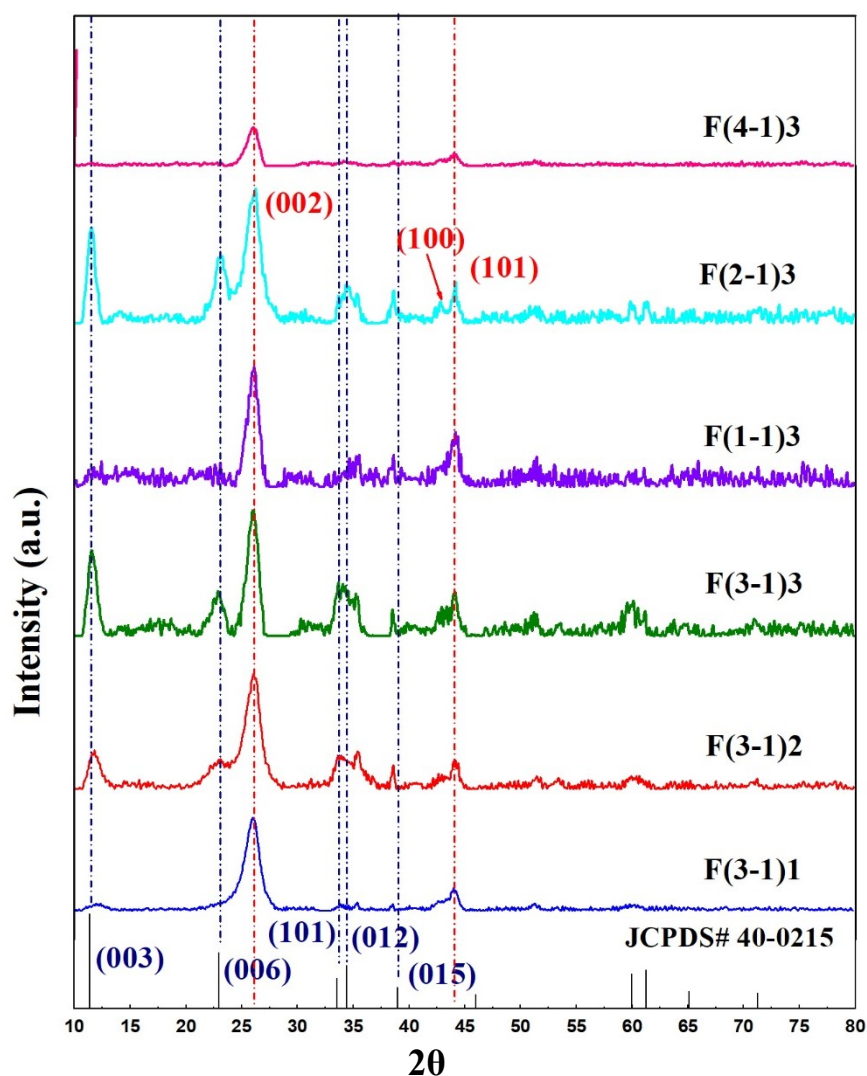


Fig. 6-2 XRD patterns with different molar ratio of Ni: Fe and different total molar.

6.3.3 N₂ Adsorption-Desorption Measurement

N₂ adsorption-desorption measurement was applied to evaluate the surface area of NiFe LDHs/MWCNTs (Fig. 6-3). As shown in Fig. 6-3, MWCNTs and NiFe LDHs/MWCNTs display typical IV isotherm line which is typical for mesoporous materials. They have classical H3 hysteresis loops at relative high pressure (Zhou et al. 2018a, Gadipelli et al. 2016, Xia et al. 2012). And the specific surface area S_{BET} was calculated by BET method, which are summarized in Table. 6-1. The S_{BET} of F(3-1)3 is 98.28 m²/g and is the smallest than that of others materials. Since some NiFe LDHs nanoparticles locate in the tube of MWCNTs. Hence, when the molar ration of Ni: Fe is 3:1, S_{BET} become smaller with the increase of total molar, because that more NiFe LDHs nanoparticles coat on the surface of MWCNTs and take the place of tube. However, the S_{BET} of F(1-1)3 is the biggest due to the fierce Fenton reaction with large ferrous salt quantity which caused the damage of the wall of WMCTN and few F(1-1)3 product generated in the preparation process locate and cover on MWCNTs.

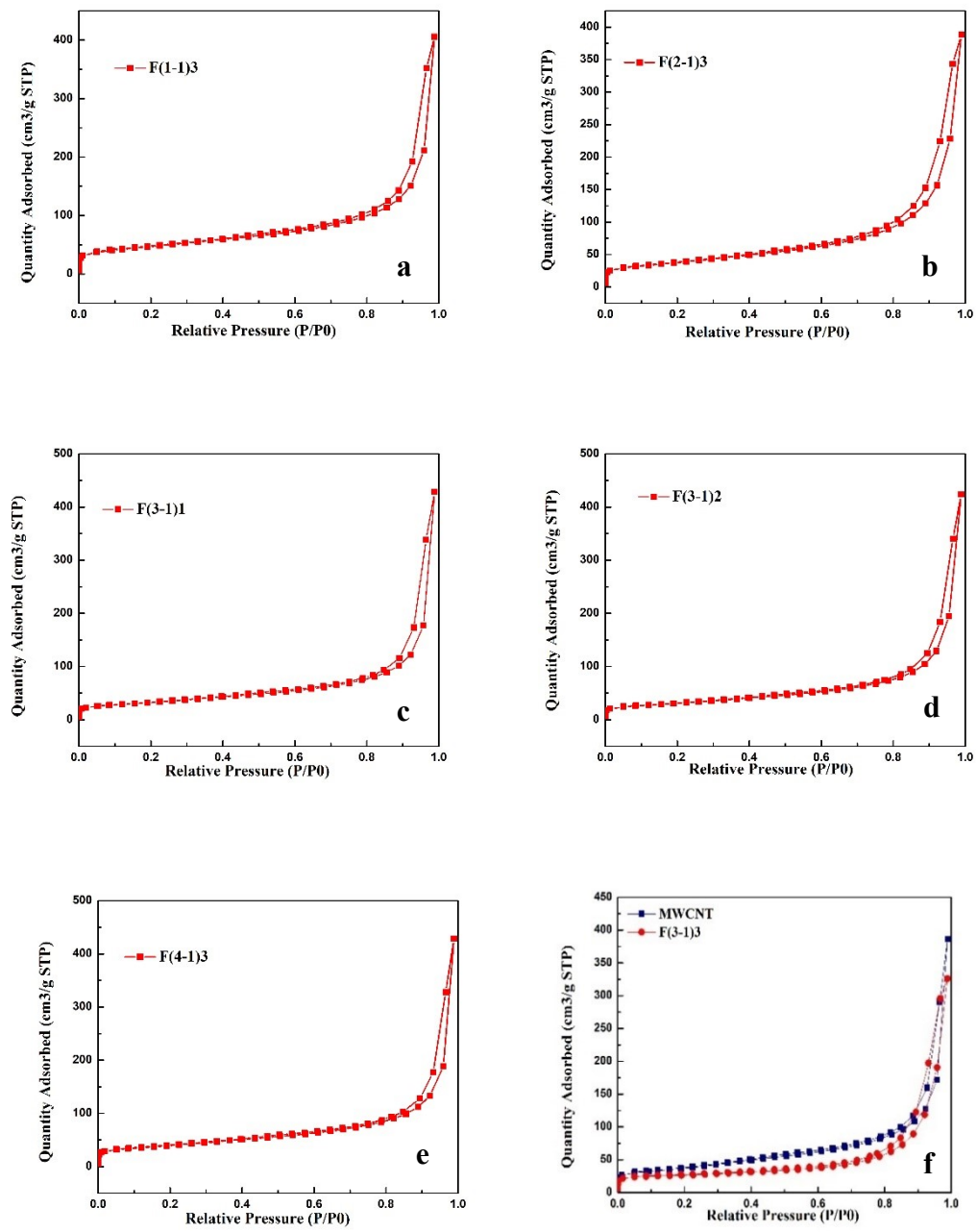


Fig. 6-3 N₂-adsorption/desorption isotherms of (a) F(1-1)3, (b) F(2-1)3, (c) F(3-1)1, (d) F(3-1)2, (e) F(4-1)3 and (f) F(3-1)3 and raw material of MWCNTs.

Table. 6-1 S_{BET} , overpotentials at different current densities of 10, 50,100 mA/cm², Tafel slopes, C_{dl} value of materials of F(1-1)3, F(2-1)3, F(3-1)1, F(3-1)2, F(3-1)3, F(4-1)3.

Products characterizations	F(1-1)3	F(2-1)3	F(3-1)1	F(3-1)2	F(3-1)3	F(4-1)3
BET(m ² /g)	166.34	133.89	115.57	110.49	98.28	139.50
Overpotential (mV) (10 mA/cm ²)	261	245	240	235	212	253
Overpotential (mV) (50 mA/cm ²)	292	278	289	276	264	284
Overpotential (mV) (100 mA/cm ²)	312	298	305	294	283	300
Tafel slope (mV/dec)	52.598	54.661	52.136	58.225	62.466	49.359
C_{dl} (mF/cm ²)	1.05	0.78	1.52	1.095	0.945	1.205

6.3.4 XPS

The chemical and valence state of F(3-1)3 was investigated by XPS. As shown in Fig. 6-4a, XPS spectrum represents the existence of Ni, Fe, C, O elements. The high resolution XPS spectrum of Ni 2p in Fig. 6-4b reveals the two spin-orbit peaks of Ni2p_{3/2}, Ni2p_{1/2} and their shakeup satellites peaks. And the spectrum can be fitted into four peaks corresponding to Ni²⁺ at 856.18 eV and 873.74 eV and Ni³⁺ at 857.31 eV and 874.82 eV respectively (Ye et al. 2017). Similarly, Fe 2p XPS spectrum is deconvoluted into three peaks, and the binding energy peaks located at 712.15eV and 725.49 eV are stands for Fe2p_{3/2}, Fe2p_{1/2}, respectively, and this implies that the oxidation state of Fe is mostly Fe³⁺ (Guo et al. 2018). And the deconvoluted O 1s peaks reveal the presence of C=C, -C=O, and -O-C=O positioned at 284.4 eV, 286.5 eV, 288.8 eV, respectively (Ni et al. 2017). The high resolution O1s spectra are categorised into three peaks marked with O1, O2, O3 which indicates metal oxide (530.2 eV), metal

hydroxide (531.4 eV) and adsorbed water (532.1 eV), suggesting the existence of NiFe LDHs (Ali-Löyty et al. 2016).

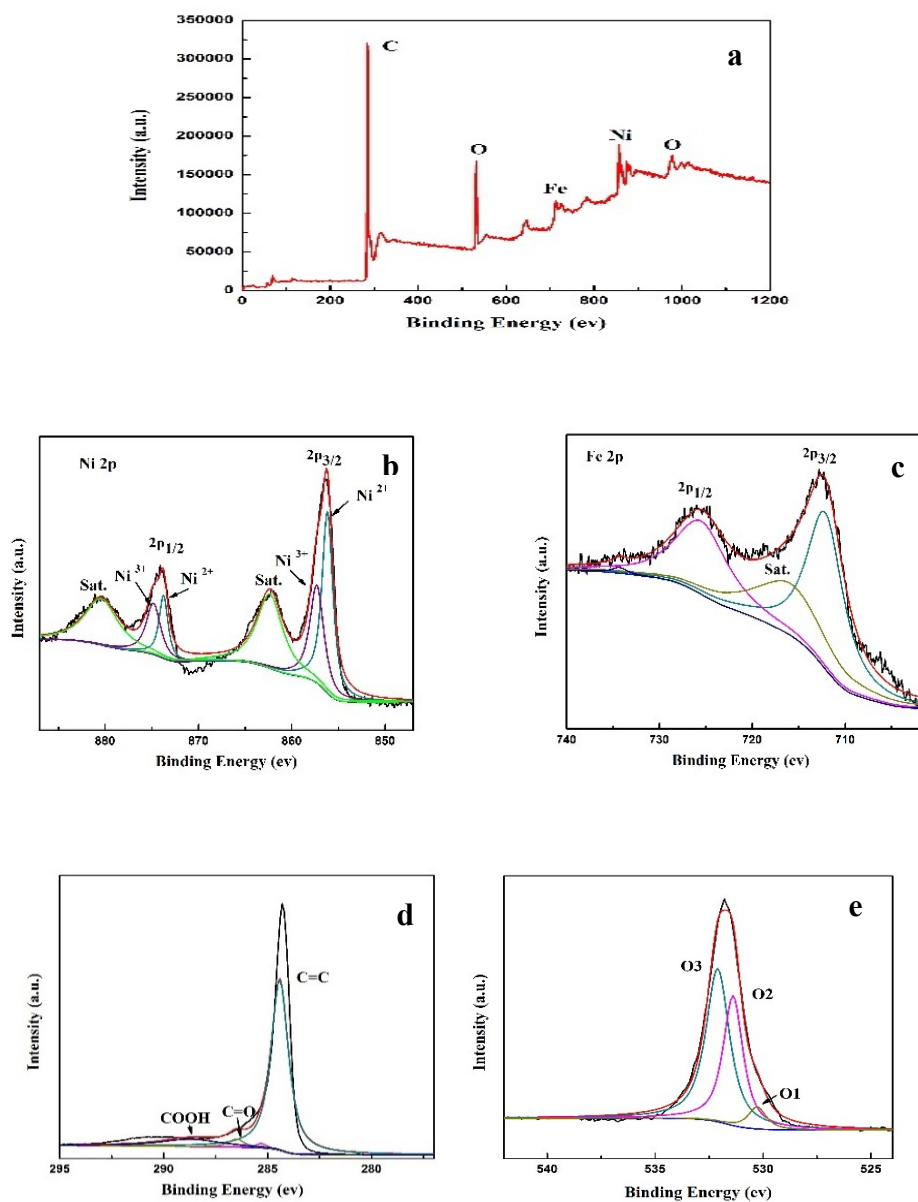


Fig. 6-4 XPS spectrum of (a) F(3-1)3 and high-resolution spectra of (b) Ni 2p, (c) Fe 2p, (d) C 1s and (e) O 1s.

6.4 Electrochemical Measurements

6.4.1 LSV and Tafel plot

In order to evaluate the OER performance of NiFe LDHs with different molar ratio of Ni and Fe and different total molar ratios, the NiFe LDHs/MWCNTs slurry were dropped on glassy carbon (GCE) as working electrode in a three-electrode system in 1.0M KOH. High purity O₂ was bubbled into the electrolyte to get rid of the air for 30 min before the test. The GCE was rotated at 1600 rpm to remove the gas generated during the OER reaction. Firstly, CV test was cycled for 15 cycles in 1.0-1.6V (vs. RHE) to active and stable the products loaded on GCE. Fig. 6-5a shows LSV curves for all the electrocatalysts at a scan rate of 5 mV/s, it can be noticed that F(3-1)3 is optimized with a small overpotential of 212 mV, 283 mV at current density of 10 mA/cm² and 100 mA/cm², respectively, which are the smallest than that of other electrocatalysts (all the overpotentials are listed in Table. 6-1). However, the Tafel plot of F(3-1)3 calculated by Tafel equation is 64.7 mV/dec is the biggest among the as-prepared composites. Due to the more quantity of NiFe LDHs located on the surface of MWCNTs which decrease the conductivity of composite of F(3-1)3. Although the high Tafel plot is not the smallest, F(3-1)3 still exists the best of electrocatalytic performance due to the intrinsic properties of NiFe LDHs. Tafel slope represents the reaction kinetics of OER, compared to F(3-1)1, F(3-1)2, the quantity of NiFe LDHs in F(3-1)3 located on MWCNTs was the largest, and NiFe LDHs has poor conductivity, hence, conductivity of F(3-1)3 is not as well as other two materials, compared to F(1-1)3, F(2-1)3 and F(4-1)3, we have recognized from XRD that only few NiFe LDHs produced in F(4-1)3, hence, it has high conductivity, which is consistent with the Tafel slope of it,

and F(3-1)3 have more generated NiFe LDHs than F(2-1)3 and F(1-1)3 when their total molar are the same, hence, it has the largest Tafel slope. The high OER performance of optimized F(3-1)3 is attributed that the high conductivity and porous structure of MWCNTs not only enhance the electron transfer of F(3-1)3, but also increase the surface area of NiFe LDHs and impede the aggregation of nanoparticles. And the low crystalline of NiFe LDHs exists short range structure and small size and hence could expose more active sites which is beneficial for OER (Detsi et al. 2016, Li et al. 2017, Doyle et al. 2013, Burke et al. 2015).

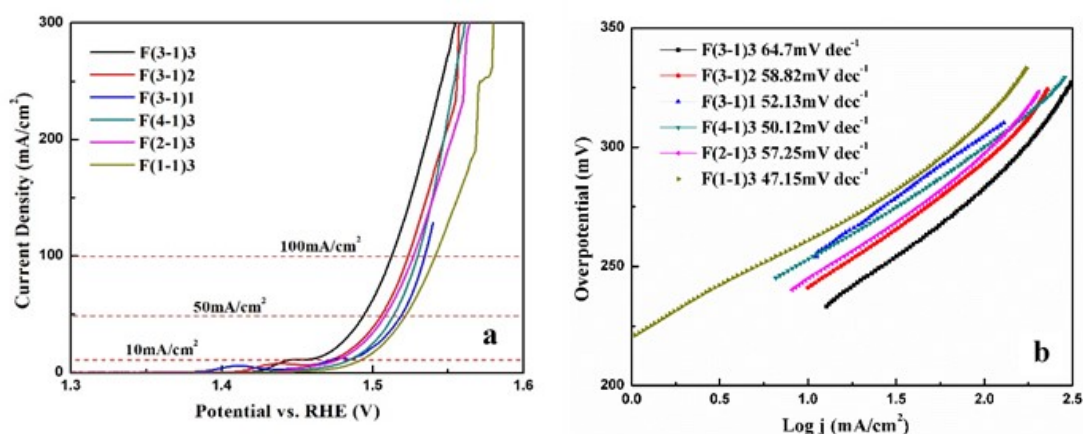


Fig. 6-5 (a) LSV curves of the NiFe LDHs with different molar ratio and different total molar ratios in 1M KOH at a scan rate of 5 mV/s (95% iR-correction) and the corresponding (b) Tafel plots calculated by Tafel equation.

6.4.2 CP/Multi-CP

Fig. 6-6a demonstrates the multi-step CP curve of F(3-1)3 with current density from 10 to 80 mA/cm² with an increment of 10 mA/cm² every 500 s without iR-correction. The potential at first is 1.47 V (vs.RHE) when the current density is 10 mA/cm². The potentials increase immediately without any delay with increasing of current density

and keep constant at each step, these results infer that F(3-1)3 has effective mass and electron transportation and high stability in a large range of current densities (Xu et al. 2018b). The long-term durability of F(3-1)3 is investigated by using CP method with a constant current density of 10 mA/cm² for 40 h. The first potential is 1.469 V and then potential become 1.495 V after 40 h, and the potential after 40 h shows 1.9% up (Fig. 6-6b). The inset in the Fig. 6-6b is the partial CP curves and the blue rectangular line shows the potential will regularly raise with the increasing of time and then drop down quickly, that is because the generated oxygen gradually cover the surface of working electrode and accumulate to a certain degree, and then the oxygen gas is removed by rotating WE and the uncovered surface of WE ensure the contact area between electrolyte and electrolysis. Hence, the potential shows cut down immediately. And this process repeats in the whole reaction(Shen et al. 2018).

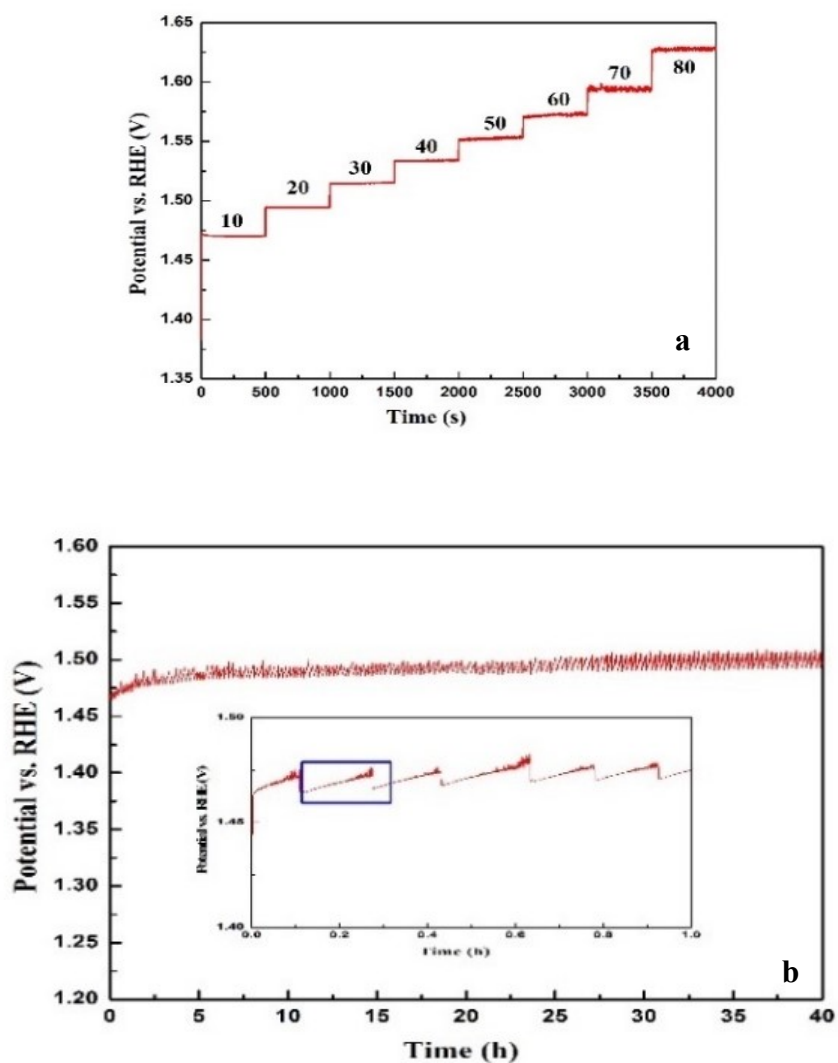
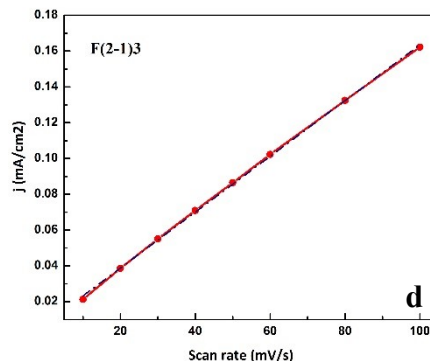
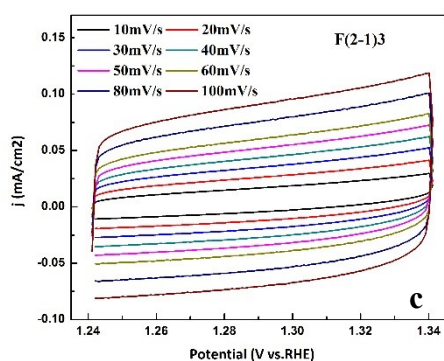
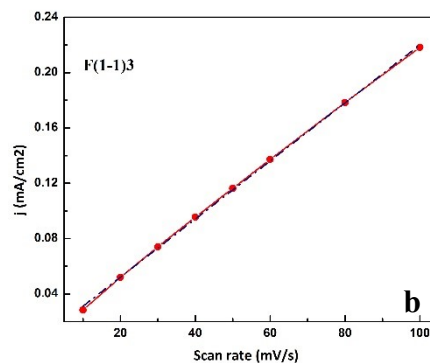
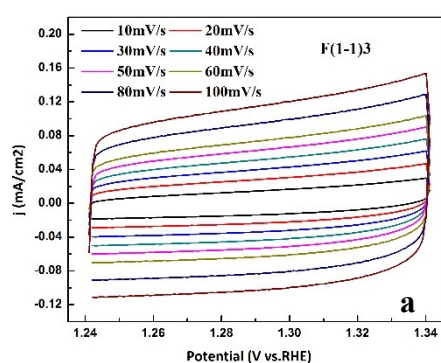


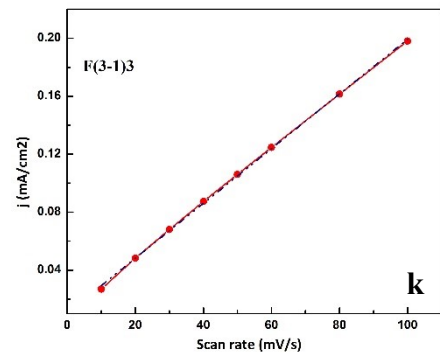
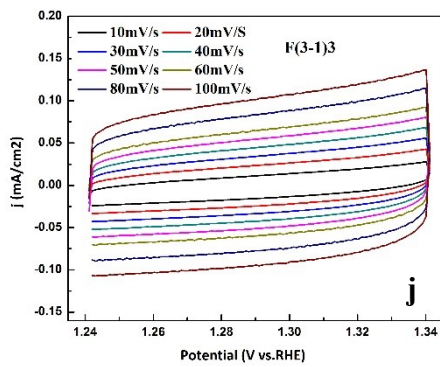
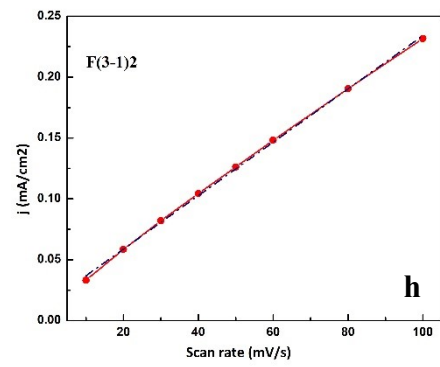
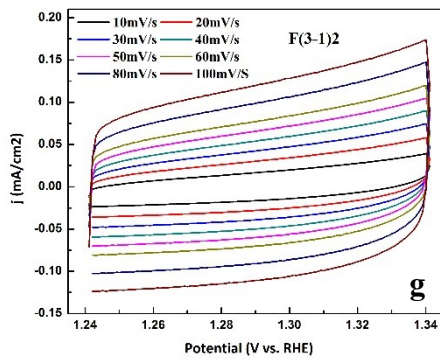
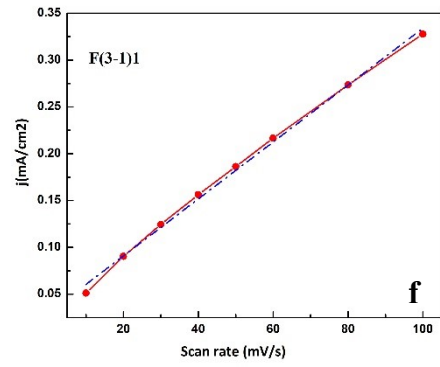
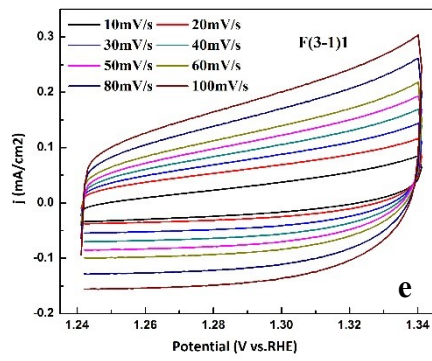
Fig. 6-6 (a) Multi-step CP curve of F(3-1)3 in 1M KOH, the current density started from 10 mA/cm² and ended at 80 mA/cm² with an increment of 10 mA/cm² every 500 s without iR correction.(b) CP curve of F(3-1)3 in 1M KOH with an current density of 10 mA/cm² for 40 h without iR correction and the inset is the CP curve of F(3-1)3 collected in the first 1h.

6.4.3 ECSA and Faradic Efficiency

To get insight into OER, ECSA was obtained from C_{dl} , C_{dl} was measured from CV curves in a potential range of 1.24-1.34 V vs. RHE at different scan rates arranged from 10 mA/cm² to 100 mA/cm².and the difference of capacitive current ($\Delta j = j_{anodic} - j_{cathodic}$)

at 1.29 V vs.RHE were plotted against the different scan rates. And the C_{dl} is the twice of the slope of the plot (Fig. 6-7). However, the C_{dl} of F(3-1)3 listed in Table 6-1 is not the smallest compared with other materials, that is because the C_{dl} represents a capacitive process and in this material, it usually performed by MWCNTs, not the intrinsic catalyst of NiFe LDHs which commonly accompanied with a pseudo-capacitance. Hence, although the BET and ECSA of F(3-1)3 are not the best, it still show superior OER electrocatalytic performance due to the intrinsic electrocatalytic properties (Dinh et al. 2018, Lu et al. 2017). The Faradaic efficiency was calculated based on the molar of oxygen generated and it is about 108%.





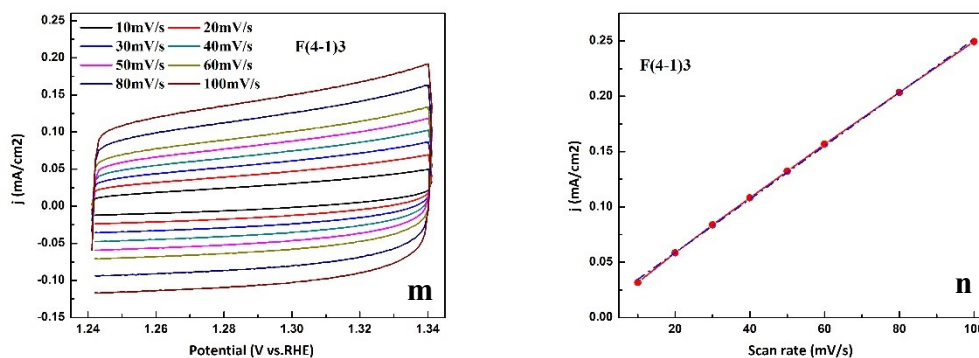


Fig. 6-7 CV curves and corresponding slopes of capacitive current densities at 1.29V vs.RHE against different scan rates of samples of (a), (b) F(1-1)3, (c), (d) F(2-1)3, (e),(f) F(3-1)1, (g), (h), F(3-1)2, (j), (k) F(3-1)3 and (m), (n) F(4-1)3.

6.5 XPS Test for Composites after Activation

To investigate the difference of NiFe LDHs/MWCNTs before activation and after activation, XPS was applied. From Fig. 6-8a and 8b, it is observed that the intensities of satellite $2P_{3/2}$ peaks of Ni and Fe increase, it is proposed that the hydrated nickel oxide and ferric oxide increase after activation in 1M KOH solution (Zhou et al. 2013, Fu et al. 2018). The increased binding energy of C-OH and COOH in high solution spectrum of C1s as shown in Fig. 6-8c also reveals this phenomenon. The small peaks in O1s after activation is the peak of Nafion.

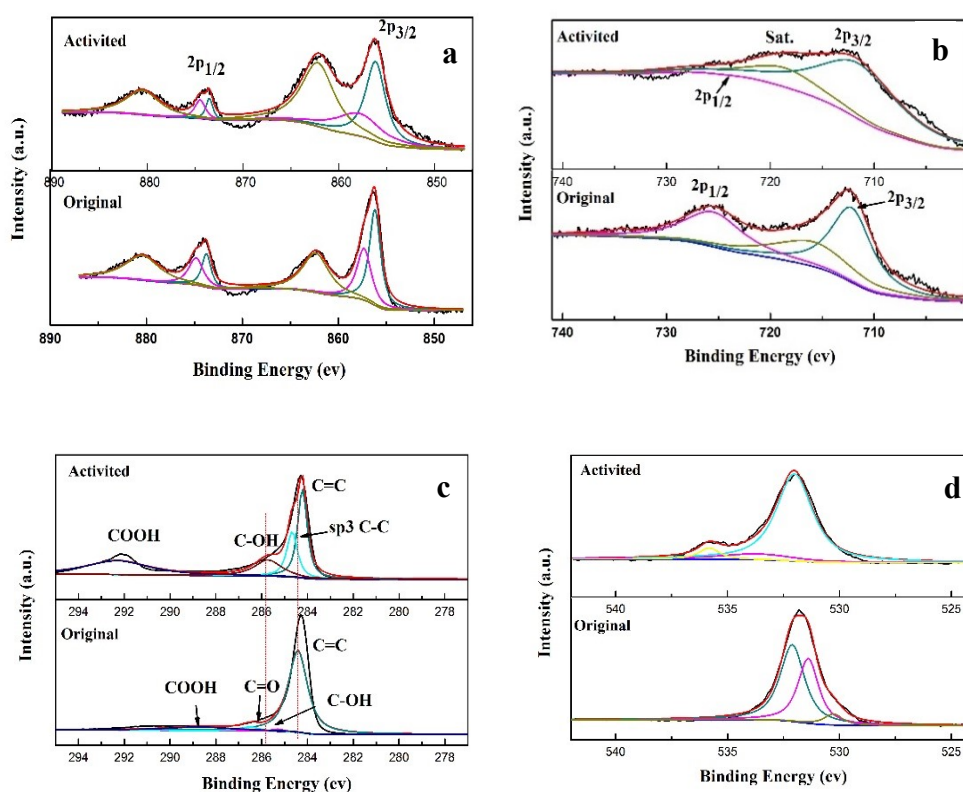


Fig. 6-8 XPS spectra of (a) Ni 2p, (b) Fe 2p, (c) C1s and (d)O1s of product of F(3-1)3 before activation and after activation.

6.6 Summary

In this chapter, composites of NiFe LDHs/MWCNTs with low crystalline NiFe LDHs were prepared by Fenton reaction and coprecipitation method. The optimized material of F(3-1)3 performs an excellent OER properties with a small overpotential of 212 mV at 10 mA/cm² and a Tafel slope of 64.46 mV/dec. The superior electrocatalytic performance of F(3-1)3 is ascribed to the followed points: (i) NiFe LDHs with a suitable molar ratio (Ni: Fe= 3:1) shows outstanding and intrinsic electrocatalytic properties, (ii) the composite has a weak crystalline with random orders and small size could expose more active site and facilitate the reaction of OER, (iii) the high conductivity of

MWCNTs enhances the charge transfer and (iv) the strong interaction and the synergetic effect between NiFe LDHs and MWCNTs ensure the long-term stability and fast mass transportation.

Chapter 7 Summary and Future Work

In this chapter, the aim is to summarize every experiment which have done in this work and make recommendations for future work which still exist in this work.

7.1 The Comparison Between Different Composites Prepared by Fenton Reaction

In this part, EG-F, AEG-F were prepared by Fenton reaction. After comparison of their CV curves and electrochemical properties, it is concluded that (i) AEG-F shows better cycling performance compared with EG-F, because EG was oxidized heavily by concentric acid to introduce more oxygen functional groups, and hence AEG is easily reacted with Fenton reagents, (ii) EG with worm-like structure are not easily reacted with Fenton reagents, because the worm-like structure impede the contact of Fenton reagents with the layer of EG. MWCNTs-F was also prepared by Fenton reaction and MWCNTs-F-H was synthesized by Fenton reaction followed with hydrothermal reaction. Compared with EG-F, MWCNTs-F exhibits better electrochemical performance due to the network conductive structure which not only provide an electronic path for electrochemical reaction, but also suffer the dropping off Fe_2O_3 particles. MWCNTs-F-H also shows the similar phenomenon like EG-F and EG-F-H, but the electrochemical property of MWCNTs-F-H is worse than that of MWCNTs-F. because that in the process of hydrothermal reaction, part of $\text{Fe}(\text{OH})_3$ nanoparticles dissolved into the solution and part of them become bigger which decrease the contact surface area between electrode and electrolyte. In the preparation process, sonication was used to promote reaction. And considering time consuming cost and the properties of composites, the optimized sonication time is 3h.

7.2 Preparation of Composite of Fe₂O₃/MWCNTs and Their Application as Anode in LIBs

In this part, composite of Fe₂O₃/MWCNTs was prepared by Fenton reaction followed with a 200°C heat treatment to make sure that Fe(OH)₃ was totally convert to Fe₂O₃.

The composite was used as anode material in LIBs. XRD and SAED demonstrate that the crystal structure of Fe₂O₃ in the composite of Fe₂O₃/MWCNTs is amorphous. CV and cycling performance test demonstrate that the composite display an excellent cycling performance with a reversible capacity of 900 mAh/g at 500 mA/g after 500 cycles and a high rate capability of 785 mAh/g at a high current density of 2 A/g. The outstanding electrochemical performance is attributed that the random ordered amorphous structure of Fe₂O₃ with nanometre size shorten the ion pathway and increase the charge transfer. The small size of Fe₂O₃ particles buffers the volume change during the charge-discharge process. MWCNTs substrate not only offers an electronic path way for high charge transfer, but also improves the rate capability and prevents the aggregation of Fe₂O₃ in the process of reaction.

7.3 Preparation of NiFe LDHs/MWCNTs Composites and Their Application as Electrocatalyst in OER

In this part, composites of NiFe LDHs/MWCNTs were fabricated by Fenton reaction followed with a coprecipitation process. The composites were characterized by SEM, TEM, XRD and XPS. XRD and SAED images indicate that the composites have low crystalline structure. The optimized product of F(3-1)3 display excellent electrocatalytic properties. and it has small overpotential of 212 mV and 283mV at 10

mA/cm² and 100 mA/cm², respectively, and a Tafel slope of 64.46 mV/dec. The outstanding electrocatalytic performance of F(3-1)3 is ascribed to that: (i) NiFe LDHs with a suitable molar ratio (Ni: Fe= 3:1) show outstanding and intrinsic electrocatalytic properties, (ii) the weak crystalline with random ordered structure and small size which could expose more active site and enhance the active surface area between electrode and electrolyte, (iii) the high conductivity of MWCNTs enhance the electron transfer and increase the kinetics of OER, (iv) the synergetic effect between NiFe LDHs and MWCNTs ensure the cycle stability and fast mass transportation.

7.4 Further Work

For comparison, it is necessary to get strong acid treated MWCNTs and react with Fenton reaction to compare with MWCNTs-F materials.

The further work on the investigate the type of oxygen functional groups and the degree of oxidation is carried out, due to different oxygen functional groups may influence the electrochemical performance of composite.

Due to the metal salts used as Fenton reagents are not just iron, therefore, other metal salts could be selected as catalyst in Fenton reaction and act as the sources for synthesizing other composites of MWCNTs with other metal oxides (hydroxide), and investigate their electrochemical properties in LIBs or OER.

Considering the merits of amorphous structure of metal oxide (hydroxide) used in LIBs and OER, another work on preparing a series of amorphous metal oxide (hydroxide)/MWCNTs composite by simple precipitation method is suggested.

Considering the phase evolution in the reaction process of LIBs, investigating the phase evolution during the electrochemical reaction process is also listed on work.

Bibliography

- Ali-Löytty, H., M. W. Louie, M. R. Singh, L. Li, H. G. Sanchez Casalongue, H. Ogasawara, E. J. Crumlin, Z. Liu, A. T. Bell, A. Nilsson & D. Friebe (2016) Ambient-Pressure XPS Study of a Ni-Fe Electrocatalyst for the Oxygen Evolution Reaction. *The Journal of Physical Chemistry C*, 120, 2247-2253.
- Anantharaj, S., S. R. Ede, K. Karthick, S. Sam Sankar, K. Sangeetha, P. E. Karthik & S. Kundu (2018) Precision and correctness in the evaluation of electrocatalytic water splitting: revisiting activity parameters with a critical assessment. *Energy & Environmental Science*, 11, 744-771.
- Bai, S., S. Chen, X. Shen, G. Zhu & G. Wang (2012) Nanocomposites of hematite (α -Fe₂O₃) nanospindles with crumpled reduced graphene oxide nanosheets as high-performance anode material for lithium-ion batteries. *RSC Advances*, 2, 10977.
- Balogun, M.-S., W. Qiu, H. Yang, W. Fan, Y. Huang, P. Fang, G. Li, H. Ji & Y. Tong (2016) A monolithic metal-free electrocatalyst for oxygen evolution reaction and overall water splitting. *Energy & Environmental Science*, 9, 3411-3416.
- Boettcher, A. S. B. a. S. W. (2015) Pulse-Electrodeposited Ni-Fe(Oxy)hydroxide Oxygen Evolution Electrocatalysts with High Geometric and Intrinsic Activities at Large Mass Loadings. *ACS Catalysis* 5 9.
- Brian J. Landi, M. J. G., Cory D. Cress,†Roberta A. DiLeo and Ryne P. Raffaele (2009) Carbon nanotubes for lithium ion batteries. *Energy & Environmental Science*, 2, 638-654.
- Bruce Dunn, H. K., Jean-Marie Tarascon (2011) electrical energy storage for the grid a battery of choices. *Science* 334, 928-935.
- Burke, M. S., M. G. Kast, L. Trotochaud, A. M. Smith & S. W. Boettcher (2015) Cobalt-iron(oxy)hydroxide oxygen evolution electrocatalysts: the role of structure and composition on activity, stability, and mechanism. *J Am Chem Soc*, 137, 3638-48.
- Cai, J., P. Zhao, Z. Li, W. Li, J. Zhong, J. Yu & Z. Yang (2017a) A corn-inspired structure design for an iron oxide fiber/reduced graphene oxide composite as a high-performance anode material for Li-ion batteries. *RSC Advances*, 7, 44874-44883.
- Cai, S., Z. Meng, H. Tang, Y. Wang & P. Tsiakaras (2017b) 3D Co-N-doped hollow carbon spheres as excellent bifunctional electrocatalysts for oxygen reduction reaction and oxygen evolution reaction. *Applied Catalysis B: Environmental*, 217, 477-484.
- Chakthranont, P., J. Kibsgaard, A. Gallo, J. Park, M. Mitani, D. Sokaras, T. Kroll, R. Sinclair, M. B. Mogensen & T. F. Jaramillo (2017) Effects of Gold Substrates on the Intrinsic and Extrinsic Activity of High-Loading Nickel-Based Oxyhydroxide Oxygen Evolution Catalysts. *ACS Catalysis*, 7, 5399-5409.
- Charles C. L. McCrory*†‡, S. J., Ivonne M. Ferrer†‡, Shawn M. Chatman†‡, Jonas C. Peters*†‡, and Thomas F. Jaramillo*†§ (2015) Benchmarking HER and OER electrocatalysts for solar water splitting devices. *J. Am. Chem. Soc*, 137, 4347-4357.

- Chaudhari, N. K., M.-S. Kim, T.-S. Bae & J.-S. Yu (2013) Hematite (α -Fe₂O₃) nanoparticles on vulcan carbon as an ultrahigh capacity anode material in lithium ion battery. *Electrochimica Acta*, 114, 60-67.
- Chaudhari, S. & M. Srinivasan (2012) 1D hollow α -Fe₂O₃ electrospun nanofibers as high performance anode material for lithium ion batteries. *Journal of Materials Chemistry*, 22, 23049.
- Chen, D., W. Wei, R. Wang, J. Zhu & L. Guo (2012) α -Fe₂O₃ nanoparticles anchored on graphene with 3D quasi-laminated architecture: in situ wet chemistry synthesis and enhanced electrochemical performance for lithium ion batteries. *New Journal of Chemistry*, 36, 1589.
- Chen, M., J. Liu, D. Chao, J. Wang, J. Yin, J. Lin, H. Jin Fan & Z. Xiang Shen (2014) Porous α -Fe₂O₃ nanorods supported on carbon nanotubes-graphene foam as superior anode for lithium ion batteries. *Nano Energy*, 9, 364-372.
- Chen, Z., Q. Wang, X. Zhang, Y. Lei, W. Hu, Y. Luo & Y. Wang (2018) N-doped defective carbon with trace Co for efficient rechargeable liquid electrolyte-/all-solid-state Zn-air batteries. *Science Bulletin*, 63, 548-555.
- Cheng, F., K. Huang, S. Liu, J. Liu & R. Deng (2011) Surfactant carbonization to synthesize pseudocubic α -Fe₂O₃/C nanocomposite and its electrochemical performance in lithium-ion batteries. *Electrochimica Acta*, 56, 5593-5598.
- Chou, S.-L., J.-Z. Wang, D. Wexler, K. Konstantinov, C. Zhong, H.-K. Liu & S.-X. Dou (2010) High-surface-area α -Fe₂O₃/carbon nanocomposite: one-step synthesis and its highly reversible and enhanced high-rate lithium storage properties. *Journal of Materials Chemistry*, 20, 2092.
- Chunyu Wu, X. L., Weishan Li, Bin Li, Yaqiong Wang, Yating Wang, Mengqing Xu, Lidan Xing (2014) Fe₂O₃ nanorods/ carbon nanofibers composite: Preparation and performance as anode of high rate lithium ion battery. *Journal of Power Sources*, 251, 85-91.
- Detsi, E., J. B. Cook, B. K. Lesel, C. L. Turner, Y.-L. Liang, S. Robbennolt & S. H. Tolbert (2016) Mesoporous Ni₆₀Fe₃₀Mn₁₀-alloy based metal/metal oxide composite thick films as highly active and robust oxygen evolution catalysts. *Energy & Environmental Science*, 9, 540-549.
- Dinh, K. N., P. Zheng, Z. Dai, Y. Zhang, R. Dangol, Y. Zheng, B. Li, Y. Zong & Q. Yan (2018) Ultrathin Porous NiFeV Ternary Layer Hydroxide Nanosheets as a Highly Efficient Bifunctional Electrocatalyst for Overall Water Splitting. *Small*, 14.
- Doyle, R. L., I. J. Godwin, M. P. Brandon & M. E. Lyons (2013) Redox and electrochemical water splitting catalytic properties of hydrated metal oxide modified electrodes. *Phys Chem Chem Phys*, 15, 13737-83.
- Du, D., W. Yue, Y. Ren & X. Yang (2014) Fabrication of graphene-encapsulated CoO/CoFe₂O₄ composites derived from layered double hydroxides and their application as anode materials for lithium-ion batteries. *Journal of Materials Science*, 49, 8031-8039.
- Enric Brillas, B. B., Ignasi Sirés, José Antonio Garrido, Rosa Mar'ia Rodr'iguez, Conchita Arias, Pere-Llu'ís Cabot, Christos Comninellis (2004) Electrochemical destruction of chlorophenoxy herbicides by anodic oxidation

- and electro-Fenton using a boron-doped diamond electrode. *Electrochimica Acta*, 49, 4487-4496.
- Fabbri, E., A. Habereder, K. Waltar, R. Kötz & T. J. Schmidt (2014) Developments and perspectives of oxide-based catalysts for the oxygen evolution reaction. *Catal. Sci. Technol.*, 4, 3800-3821.
- Fang, H., W. Zou, J. Yan, Y. Xing & S. Zhang (2018) Facile Fabrication of Fe₂O₃ Nanoparticles Anchored on Carbon Nanotubes as High-Performance Anode for Lithium Ion Batteries. *ChemElectroChem*.
- Feng, Y., H. Zhang, Y. Zhang, X. Li & Y. Wang (2015) Ultrathin Two-Dimensional Free-Standing Sandwiched NiFe/C for High-Efficiency Oxygen Evolution Reaction. *ACS Appl Mater Interfaces*, 7, 9203-10.
- Fu, G., Z. Cui, Y. Chen, Y. Li, Y. Tang & J. B. Goodenough (2017) Ni₃Fe-N Doped Carbon Sheets as a Bifunctional Electrocatalyst for Air Cathodes. *Advanced Energy Materials*, 7, 1601172.
- Fu, Y., H.-Y. Yu, C. Jiang, T.-H. Zhang, R. Zhan, X. Li, J.-F. Li, J.-H. Tian & R. Yang (2018) NiCo Alloy Nanoparticles Decorated on N-Doped Carbon Nanofibers as Highly Active and Durable Oxygen Electrocatalyst. *Advanced Functional Materials*, 28, 1705094.
- Gür, T. M. (2018) Review of electrical energy storage technologies, materials and systems: challenges and prospects for large-scale grid storage. *Energy & Environmental Science*, 11, 2696-2767.
- Gadipelli, S., T. Zhao, S. A. Shevlin & Z. Guo (2016) Switching effective oxygen reduction and evolution performance by controlled graphitization of a cobalt–nitrogen–carbon framework system. *Energy & Environmental Science*, 9, 1661-1667.
- Georgakilas, V., M. Otyepka, A. B. Bourlinos, V. Chandra, N. Kim, K. C. Kemp, P. Hobza, R. Zboril & K. S. Kim (2012) Functionalization of graphene: covalent and non-covalent approaches, derivatives and applications. *Chem Rev*, 112, 6156-214.
- Gong, M. & H. Dai (2014) A mini review of NiFe-based materials as highly active oxygen evolution reaction electrocatalysts. *Nano Research*, 8, 23-39.
- Gong, M., Y. Li, H. Wang, Y. Liang, J. Z. Wu, J. Zhou, J. Wang, T. Regier, F. Wei & H. Dai (2013) An advanced Ni-Fe layered double hydroxide electrocatalyst for water oxidation. *J Am Chem Soc*, 135, 8452-5.
- Guo, J., X. Li, Y. Sun, Q. Liu, Z. Quan & X. Zhang (2018) In-situ confined formation of NiFe layered double hydroxide quantum dots in expanded graphite for active electrocatalytic oxygen evolution. *Journal of Solid State Chemistry*, 262, 181-185.
- Guo, S., G. Zhang, Y. Guo & J. C. Yu (2013) Graphene oxide–Fe₂O₃ hybrid material as highly efficient heterogeneous catalyst for degradation of organic contaminants. *Carbon*, 60, 437-444.
- Gupta, V. & T. A. Saleh (2011) Syntheses of Carbon Nanotube-Metal Oxides Composites; Adsorption and Photo-degradation.
- Han, L., S. Dong & E. Wang (2016) Transition-Metal (Co, Ni, and Fe)-Based Electrocatalysts for the Water Oxidation Reaction. *Adv Mater*, 28, 9266-9291.

- Han, S., X. Hu, J. Wang, X. Fang & Y. Zhu (2018) Novel Route to Fe-Based Cathode as an Efficient Bifunctional Catalysts for Rechargeable Zn-Air Battery. *Advanced Energy Materials*, 8, 1800955.
- Han, X., X. Wu, C. Zhong, Y. Deng, N. Zhao & W. Hu (2017) NiCo₂S₄ nanocrystals anchored on nitrogen-doped carbon nanotubes as a highly efficient bifunctional electrocatalyst for rechargeable zinc-air batteries. *Nano Energy*, 31, 541-550.
- Hao Bai, W. J., Gregg P. Kotchey, Wissam A. Saidi, Benjamin J. Bythell, Jacqueline M. Jarvis, Alan G. Marshall, RenãA. S. Robinson, Alexander Star (2014) Insight into the Mechanism of Graphene Oxide Degradation via the Photo-Fenton Reaction. *J. Phys. Chem. C* 118,, 10519-10529.
- Hao, S., B. Zhang, S. Ball, J. Wu, M. Srinivasan & Y. Huang (2016) Phase transition of hollow-porous α -Fe₂O₃ microsphere based anodes for lithium ion batteries during high rate cycling. *Journal of Materials Chemistry A*, 4, 16569-16575.
- Hector D. Abruna, Y. K., and Jay C Henderson (2008) batteries and electrochemical capacitors. *Physics Today*, 43-47.
- Heron Vrubel, T. M., Michael Grätzel and Xile Hu (2013) Revealing and accelerating slow electron transport in amorphous molybdenum sulphide particles for hydrogen evolution reaction *Chemical Communications* 49.
- Hu, J., C. F. Sun, E. Gillette, Z. Gui, Y. Wang & S. B. Lee (2016) Dual-template ordered mesoporous carbon/Fe₂O₃ nanowires as lithium-ion battery anodes. *Nanoscale*, 8, 12958-69.
- Hu, J., J. Zheng, L. Tian, Y. Duan, L. Lin, S. Cui, H. Peng, T. Liu, H. Guo, X. Wang & F. Pan (2015) A core-shell nanohollow-gamma-Fe₂O₃@graphene hybrid prepared through the Kirkendall process as a high performance anode material for lithium ion batteries. *Chem Commun (Camb)*, 51, 7855-8.
- Huang, B., Z. Pan, X. Su & L. An (2018) Recycling of lithium-ion batteries: Recent advances and perspectives. *Journal of Power Sources*, 399, 274-286.
- Huang, Y., Z. Lin, M. Zheng, T. Wang, J. Yang, F. Yuan, X. Lu, L. Liu & D. Sun (2016) Amorphous Fe₂O₃ nanoshells coated on carbonized bacterial cellulose nanofibers as a flexible anode for high-performance lithium ion batteries. *Journal of Power Sources*, 307, 649-656.
- Hunter, B. M., W. Hieringer, J. R. Winkler, H. B. Gray & A. M. Müller (2016) Effect of interlayer anions on [NiFe]-LDH nanosheet water oxidation activity. *Energy & Environmental Science*, 9, 1734-1743.
- Jia, Y., L. Zhang, G. Gao, H. Chen, B. Wang, J. Zhou, M. T. Soo, M. Hong, X. Yan, G. Qian, J. Zou, A. Du & X. Yao (2017) A Heterostructure Coupling of Exfoliated Ni-Fe Hydroxide Nanosheet and Defective Graphene as a Bifunctional Electrocatalyst for Overall Water Splitting. *Adv Mater*, 29.
- Jiang, X., W. Guo, P. Lu, D. Song, A. Guo, J. Liu, J. Liang & F. Hou (2018) CNTs@ γ -Fe₂O₃ @C composite electrode for high capacity lithium ion storage. *International Journal of Hydrogen Energy*.
- Jiang, Y., D. Zhang, Y. Li, T. Yuan, N. Bahlawane, C. Liang, W. Sun, Y. Lu & M. Yan (2014) Amorphous Fe₂O₃ as a high-capacity, high-rate and long-life anode material for lithium ion batteries. *Nano Energy*, 4, 23-30.

- Jin Suntivich, K. J. M., Hubert A. Gasteiger, John B. Goodenough, Yang Shao-Horn (2011) A Perovskite Oxide Optimized for Oxygen Evolution Catalysis from molecular orbital principles. *Science*, 334, 1383-1385.
- Jinlong Liu, J. J., Dong Qian, Gongrong Tan, Sanjun Peng, Huimin Yuan, Dongming Luo, Qunfeng Wang and Youcai Liu (2013) Facile assembly of a 3D rGO MWCNTs Fe₂O₃ ternary composite as the anode material for high-performance lithium ion batteries *RSC Adv.*, 3, 15457-15466.
- Jun Liu, Z. W., Qingyong Tian, Wei Wu and Xiangheng Xiao (2016) Shape-controlled iron oxide nanocrystals synthesis, magnetic properties and energy conversion applications. *CrystEngComm*, 18, 6303-6326.
- K. S. Novoselov, A. K. G., S. V. Morozov, D. Jiang, Y. Zhang, S. V. Dubonos, I. V. Grigorieva, A. A. Firsov (2004) Electric Field Effect in Atomically Thin Carbon Films. *Science* 306, 666-669.
- Keppeler, M., N. Shen, S. Nageswaran & M. Srinivasan (2016) Synthesis of α -Fe₂O₃/carbon nanocomposites as high capacity electrodes for next generation lithium ion batteries: a review. *Journal of Materials Chemistry A*, 4, 18223-18239.
- Khan, M., M. N. Tahir, S. F. Adil, H. U. Khan, M. R. H. Siddiqui, A. A. Al-warthan & W. Tremel (2015) Graphene based metal and metal oxide nanocomposites: synthesis, properties and their applications. *Journal of Materials Chemistry A*, 3, 18753-18808.
- Kong, D., C. Cheng, Y. Wang, B. Liu, Z. Huang & H. Y. Yang (2016) Seed-assisted growth of α -Fe₂O₃ nanorod arrays on reduced graphene oxide: a superior anode for high-performance Li-ion and Na-ion batteries. *Journal of Materials Chemistry A*, 4, 11800-11811.
- Lee, Y.-C., S.-J. Chang, M.-H. Choi, T.-J. Jeon, T. Ryu & Y. S. Huh (2013) Self-assembled graphene oxide with organo-building blocks of Fe-aminoclay for heterogeneous Fenton-like reaction at near-neutral pH: A batch experiment. *Applied Catalysis B: Environmental*, 142-143, 494-503.
- Li, H. B., M. H. Yu, F. X. Wang, P. Liu, Y. Liang, J. Xiao, C. X. Wang, Y. X. Tong & G. W. Yang (2013) Amorphous nickel hydroxide nanospheres with ultrahigh capacitance and energy density as electrochemical pseudocapacitor materials. *Nat Commun*, 4, 1894.
- Li, K., H. Chen, F. Shua, D. Xue & X. Guo (2014) Facile synthesis of iron-based compounds as high performance anode materials for Li-ion batteries. *RSC Advances*, 4, 36507.
- Li, P., X. Duan, Y. Kuang, Y. Li, G. Zhang, W. Liu & X. Sun (2018a) Tuning Electronic Structure of NiFe Layered Double Hydroxides with Vanadium Doping toward High Efficient Electrocatalytic Water Oxidation. *Advanced Energy Materials*, 8, 1703341.
- Li, R., J. Xu, J. Ba, Y. Li, C. Liang & T. Tang (2018b) Facile synthesis of nanometer-sized NiFe layered double hydroxide/nitrogen-doped graphite foam hybrids for enhanced electrocatalytic oxygen evolution reactions. *International Journal of Hydrogen Energy*, 43, 7956-7963.

- Li, W., Y. Bai, Y. Zhang, M. Sun, R. Cheng, X. Xu, Y. Chen & Y. Mo (2005) Effect of hydroxyl radical on the structure of multi-walled carbon nanotubes. *Synthetic Metals*, 155, 509-515.
- Li, X., Y. Ma, L. Qin, Z. Zhang, Z. Zhang, Y.-Z. Zheng & Y. Qu (2015) A bottom-up synthesis of α -Fe₂O₃ nanoaggregates and their composites with graphene as high performance anodes in lithium-ion batteries. *Journal of Materials Chemistry A*, 3, 2158-2165.
- Li, Z., L. Li, W. Zhong, A. Cheng, W. Fu, Z. Li & H. Zhang (2018c) Simple and efficient fabrication of pomegranate-like Fe₂O₃@C on carbon cloth as an anode for lithium-ion batteries. *Journal of Alloys and Compounds*, 766, 253-260.
- Li, Z., M. Shao, Q. Yang, Y. Tang, M. Wei, D. G. Evans & X. Duan (2017) Directed synthesis of carbon nanotube arrays based on layered double hydroxides toward highly-efficient bifunctional oxygen electrocatalysis. *Nano Energy*, 37, 98-107.
- Lim, H.-S., Y.-K. Sun & K.-D. Suh (2013) Rattle type α -Fe₂O₃ submicron spheres with a thin carbon layer for lithium-ion battery anodes. *Journal of Materials Chemistry A*, 1, 10107.
- Liu, J., Y. Ji, J. Nai, X. Niu, Y. Luo, L. Guo & S. Yang (2018a) Ultrathin amorphous cobalt–vanadium hydr(oxy)oxide catalysts for the oxygen evolution reaction. *Energy & Environmental Science*.
- Liu, M.-R., Q.-L. Hong, Q.-H. Li, Y. Du, H.-X. Zhang, S. Chen, T. Zhou & J. Zhang (2018b) Cobalt Boron Imidazolate Framework Derived Cobalt Nanoparticles Encapsulated in B/N Codoped Nanocarbon as Efficient Bifunctional Electrocatalysts for Overall Water Splitting. *Advanced Functional Materials*, 28, 1801136.
- Liu, R., C. Zhang, Q. Wang, C. Shen, Y. Wang, Y. Dong, N. Zhang & M. Wu (2018c) Facile synthesis of α -Fe₂O₃@C hollow spheres as ultra-long cycle performance anode materials for lithium ion battery. *Journal of Alloys and Compounds*, 742, 490-496.
- Liu, S., Z. Chen, K. Xie, Y. Li, J. Xu & C. Zheng (2014) A facile one-step hydrothermal synthesis of α -Fe₂O₃ nanoplates imbedded in graphene networks with high-rate lithium storage and long cycle life. *J. Mater. Chem. A*, 2, 13942-13948.
- Liu, W., H. Liu, L. Dang, H. Zhang, X. Wu, B. Yang, Z. Li, X. Zhang, L. Lei & S. Jin (2017) Amorphous Cobalt-Iron Hydroxide Nanosheet Electrocatalyst for Efficient Electrochemical and Photo-Electrochemical Oxygen Evolution. *Advanced Functional Materials*, 27, 1603904.
- Liu, X., M. Park, M. G. Kim, S. Gupta, G. Wu & J. Cho (2015a) Integrating NiCo Alloys with Their Oxides as Efficient Bifunctional Cathode Catalysts for Rechargeable Zinc-Air Batteries. *Angew Chem Int Ed Engl*, 54, 9654-8.
- Liu, Y., J. Xu, X. Qin, H. Xin, X. Yuan, J. Zhang, D. Li & C. Song (2015b) Electrode activation via vesiculation: improved reversible capacity of γ -Fe₂O₃@C/MWNT composite anodes for lithium-ion batteries. *Journal of Materials Chemistry A*, 3, 9682-9688.
- Lu, F., M. Zhou, Y. Zhou & X. Zeng (2017) First-Row Transition Metal Based Catalysts for the Oxygen Evolution Reaction under Alkaline Conditions: Basic Principles and Recent Advances. *Small*, 13.

- Lu, X. & C. Zhao (2015) Electrodeposition of hierarchically structured three-dimensional nickel-iron electrodes for efficient oxygen evolution at high current densities. *Nat Commun*, 6, 6616.
- Lu, X. F., X. Y. Chen, W. Zhou, Y. X. Tong & G. R. Li (2015) alpha-Fe₂O₃@PANI Core-Shell Nanowire Arrays as Negative Electrodes for Asymmetric Supercapacitors. *ACS Appl Mater Interfaces*, 7, 14843-50.
- Lu, Z., W. Xu, W. Zhu, Q. Yang, X. Lei, J. Liu, Y. Li, X. Sun & X. Duan (2014) Three-dimensional NiFe layered double hydroxide film for high-efficiency oxygen evolution reaction. *Chem Commun (Camb)*, 50, 6479-82.
- M. Li, J. P. C., J.H. Fang, Y. Yang, F. Liu, X.B. Zhang (2014) NiAl-layered Double Hydroxide Reduced Graphene Oxide Composite Microwave-assisted Synthesis and Supercapacitive Properties. *Electrochimica Acta*, 134, 309-318.
- Ma, J., X. Guo, Y. Yan, H. Xue & H. Pang (2018) FeO_x-Based Materials for Electrochemical Energy Storage. *Adv Sci (Weinh)*, 5, 1700986.
- Ma, Y., G. Ji & J. Y. Lee (2011) Synthesis of mixed-conducting carbon coated porous γ-Fe₂O₃ microparticles and their properties for reversible lithium ion storage. *Journal of Materials Chemistry*, 21, 13009.
- Mahala, C., M. D. Sharma & M. Basu (2018) 2D Nanostructures of CoFe₂O₄ and NiFe₂O₄: Efficient Oxygen Evolution Catalyst. *Electrochimica Acta*, 273, 462-473.
- Min Hong, Y. S., Chao Zhou, Lu Yao, Jing Hu, Zhi Yang, Liying Zhang, Zhihua Zhou, Nantao Hu, Yafei Zhang (2019) Scalable synthesis of g-Fe₂O₃ CNT composite as high-performance. *Journal of Alloys and Compounds*, 770, 116-124.
- Mishra, A., A. Mehta, S. Basu, S. J. Malode, N. P. Shetti, S. S. Shukla, M. N. Nadagouda & T. M. Aminabhavi (2018) Electrode materials for lithium-ion batteries. *Materials Science for Energy Technologies*, 1, 182-187.
- Mo, C., J. Jian, J. Li, Z. Fang, Z. Zhao, Z. Yuan, M. Yang, Y. Zhang, L. Dai & D. Yu (2018) Boosting water oxidation on metal-free carbon nanotubes via directional interfacial charge-transfer induced by an adsorbed polyelectrolyte. *Energy & Environmental Science*, 11, 3334-3341.
- Ni, Y., L. Yao, Y. Wang, B. Liu, M. Cao & C. Hu (2017) Construction of hierarchically porous graphitized carbon-supported NiFe layered double hydroxides with a core-shell structure as an enhanced electrocatalyst for the oxygen evolution reaction. *Nanoscale*, 9, 11596-11604.
- Parimal Routh, S. D., Arnab Shit, Partha Bairi, Pradip Das, and Arun K. Nandi (2013) Graphene quantum dots from a facile sono-Fenton reaction. *ACS Appl. Mater. Interfaces*, 5, 12672-12680.
- Park, S. K., G. D. Park & Y. C. Kang (2018) Three-dimensional porous microspheres comprising hollow Fe₂O₃ nanorods/CNT building blocks with superior electrochemical performance for lithium ion batteries. *Nanoscale*, 10, 11150-11157.
- Pendashteh, A., J. Palma, M. Anderson & R. Marcilla (2017) NiCoMnO₄ nanoparticles on N-doped graphene: Highly efficient bifunctional electrocatalyst for oxygen reduction/evolution reactions. *Applied Catalysis B: Environmental*, 201, 241-252.

- Penki, T. R., S. Shivakumara, M. Minakshi & N. Munichandraiah (2015) Porous Flower-like α -Fe₂O₃ Nanostructure: A High Performance Anode Material for Lithium-ion Batteries. *Electrochimica Acta*, 167, 330-339.
- Qi, T., J. Jiang, H. Chen, H. Wan, L. Miao & L. Zhang (2013) Synergistic effect of Fe₃O₄/reduced graphene oxide nanocomposites for supercapacitors with good cycling life. *Electrochimica Acta*, 114, 674-680.
- Qi, W., J. G. Shapter, Q. Wu, T. Yin, G. Gao & D. Cui (2017) Nanostructured anode materials for lithium-ion batteries: principle, recent progress and future perspectives. *Journal of Materials Chemistry A*, 5, 19521-19540.
- Qu, K., Y. Zheng, S. Dai & S. Z. Qiao (2016) Graphene oxide-polydopamine derived N, S-codoped carbon nanosheets as superior bifunctional electrocatalysts for oxygen reduction and evolution. *Nano Energy*, 19, 373-381.
- Rao, C. N., A. K. Sood, K. S. Subrahmanyam & A. Govindaraj (2009) Graphene: the new two-dimensional nanomaterial. *Angew Chem Int Ed Engl*, 48, 7752-77.
- Ren, Y., J. Wang, X. Huang & J. Ding (2016) Enhanced lithium-ion storage performance by structural phase transition from two-dimensional rhombohedral Fe₂O₃ to cubic Fe₃O₄. *Electrochimica Acta*, 198, 22-31.
- Roy, P. & S. K. Srivastava (2015) Nanostructured anode materials for lithium ion batteries. *Journal of Materials Chemistry A*, 3, 2454-2484.
- Sengeni Anantharaj, M. V., Ashish S. Salunke, Tangella V. S. V. Simha, Vijayakumar Prabu, and Subrata Kundu (2017) High-Performance Oxygen Evolution Anode from Stainless Steel via Controlled Surface Oxidation and Cr Removal. *ACS Sustainable Chem. Eng.*, 5, 10072-10083.
- Shao, J., J. Zhang, J. Jiang, G. Zhou & M. Qu (2011) α -Fe₂O₃@CNSs nanocomposites as superior anode materials for lithium-ion batteries. *Electrochimica Acta*, 56, 7005-7011.
- Shen, J., M. Wang, L. Zhao, P. Zhang, J. Jiang & J. Liu (2018) Amorphous Ni(Fe)O_x H_y-coated nanocone arrays self-supported on stainless steel mesh as a promising oxygen-evolving anode for large scale water splitting. *Journal of Power Sources*, 389, 160-168.
- Song, F., L. Bai, A. Moysiadou, S. Lee, C. Hu, L. Liardet & X. Hu (2018) Transition Metal Oxides as Electrocatalysts for the Oxygen Evolution Reaction in Alkaline Solutions: An Application-Inspired Renaissance. *J Am Chem Soc*, 140, 7748-7759.
- Song, F. & X. Hu (2014) Exfoliation of layered double hydroxides for enhanced oxygen evolution catalysis. *Nat Commun*, 5, 4477.
- Srivastava, M., J. Singh, T. Kuila, R. K. Layek, N. H. Kim & J. H. Lee (2015) Recent advances in graphene and its metal-oxide hybrid nanostructures for lithium-ion batteries. *Nanoscale*, 7, 4820-68.
- Stevens, M. B., L. J. Enman, A. S. Batchellor, M. R. Cosby, A. E. Vise, C. D. M. Trang & S. W. Boettcher (2016) Measurement Techniques for the Study of Thin Film Heterogeneous Water Oxidation Electrocatalysts. *Chemistry of Materials*, 29, 120-140.
- Suen, N. T., S. F. Hung, Q. Quan, N. Zhang, Y. J. Xu & H. M. Chen (2017) Electrocatalysis for the oxygen evolution reaction: recent development and future perspectives. *Chem Soc Rev*, 46, 337-365.

- Swierk, J. R., S. Klaus, L. Trotochaud, A. T. Bell & T. D. Tilley (2015) Electrochemical Study of the Energetics of the Oxygen Evolution Reaction at Nickel Iron (Oxy)Hydroxide Catalysts. *The Journal of Physical Chemistry C*, 119, 19022-19029.
- Tang, C., H. F. Wang & Q. Zhang (2018) Multiscale Principles To Boost Reactivity in Gas-Involving Energy Electrocatalysis. *Acc Chem Res*, 51, 881-889.
- Tang, D., J. Liu, X. Wu, R. Liu, X. Han, Y. Han, H. Huang, Y. Liu & Z. Kang (2014) Carbon quantum dot/NiFe layered double-hydroxide composite as a highly efficient electrocatalyst for water oxidation. *ACS Appl Mater Interfaces*, 6, 7918-25.
- Tingting Wang , J. W., Yiling Liu , Xiao Cui, Pan Ding, Jun Deng, Chenyang Zha, Emerson Coy, Yanguang Li (2019) Scalable preparation and stabilization of atomic-thick CoNi layered double hydroxide nanosheets for bifunctional oxygen electrocatalysis and rechargeable zinc-air batteries. *Energy Storage Materials*, 16, 24-30.
- Tong, Y., X. Yu, H. Wang, B. Yao, C. Li & G. Shi (2018) Trace Level Co–N Doped Graphite Foams as High-Performance Self-Standing Electrocatalytic Electrodes for Hydrogen and Oxygen Evolution. *ACS Catalysis*, 8, 4637-4644.
- Wang, H.-F., C. Tang, B. Wang, B.-Q. Li, X. Cui & Q. Zhang (2018a) Defect-rich carbon fiber electrocatalysts with porous graphene skin for flexible solid-state zinc–air batteries. *Energy Storage Materials*, 15, 124-130.
- Wang, J., G. Wang & H. Wang (2015) Flexible free-standing Fe₂O₃/graphene/carbon nanotubes hybrid films as anode materials for high performance lithium-ion batteries. *Electrochimica Acta*, 182, 192-201.
- Wang, Q., K. Dastafkan & C. Zhao (2018b) Design strategies for non-precious metal oxide electrocatalysts for oxygen evolution reactions. *Current Opinion in Electrochemistry*, 10, 16-23.
- Wang, Q., L. Jiao, H. Du, Y. Wang & H. Yuan (2014) Fe₃O₄ nanoparticles grown on graphene as advanced electrode materials for supercapacitors. *Journal of Power Sources*, 245, 101-106.
- Wang, Q., L. Shang, R. Shi, X. Zhang, G. I. N. Waterhouse, L.-Z. Wu, C.-H. Tung & T. Zhang (2017a) 3D carbon nanoframe scaffold-immobilized Ni₃FeN nanoparticle electrocatalysts for rechargeable zinc-air batteries' cathodes. *Nano Energy*, 40, 382-389.
- Wang, Q., L. Shang, R. Shi, X. Zhang, Y. Zhao, G. I. N. Waterhouse, L.-Z. Wu, C.-H. Tung & T. Zhang (2017b) NiFe Layered Double Hydroxide Nanoparticles on Co,N-Codoped Carbon Nanoframes as Efficient Bifunctional Catalysts for Rechargeable Zinc-Air Batteries. *Advanced Energy Materials*, 7, 1700467.
- Wang, Y., D. Yan, S. El Hankari, Y. Zou & S. Wang (2018c) Recent Progress on Layered Double Hydroxides and Their Derivatives for Electrocatalytic Water Splitting. *Adv Sci (Weinh)*, 5, 1800064.
- Wang, Z., D. Luan, S. Madhavi, Y. Hu & X. W. Lou (2012) Assembling carbon-coated α -Fe₂O₃ hollow nanohorns on the CNT backbone for superior lithium storage capability. *Energy Environ. Sci.*, 5, 5252-5256.

- Wu, M., J. Chen, C. Wang, F. Wang, B. Yi, W. Su, Z. Wei & S. Liu (2014) Facile Synthesis of Fe₂O₃ Nanobelts/CNTs Composites as High-performance Anode for Lithium-ion Battery. *Electrochimica Acta*, 132, 533-537.
- Wu, M., Y. Wang, Z. Wei, L. Wang, M. Zhuo, J. Zhang, X. Han & J. Ma (2018a) Ternary doped porous carbon nanofibers with excellent ORR and OER performance for zinc-air batteries. *Journal of Materials Chemistry A*, 6, 10918-10925.
- Wu, Z., P. Li, Q. Qin, Z. Li & X. Liu (2018b) N-doped graphene combined with alloys (NiCo, CoFe) and their oxides as multifunctional electrocatalysts for oxygen and hydrogen electrode reactions. *Carbon*, 139, 35-44.
- Wu, Z., Z. Zou, J. Huang & F. Gao (2018c) Fe-doped NiO mesoporous nanosheets array for highly efficient overall water splitting. *Journal of Catalysis*, 358, 243-252.
- Xia, B. Y., S. Ding, H. B. Wu, X. Wang & X. Wen (2012) Hierarchically structured Pt/CNT@TiO₂ nanocatalysts with ultrahigh stability for low-temperature fuel cells. *RSC Adv.*, 2, 792-796.
- Xiang Zhang, H. L., Shaikshavali Petnikota, Seeram Ramakrishna and Hong Jin Fan (2014) Electrospun Fe₂O₃-carbon composite nanofibers as durable anode materials for lithium ion batteries *Journal of materials Chemistry A*, 2, 10835-10841.
- Xiao, L., M. Schroeder, S. Kluge, A. Balducci, U. Hagemann, C. Schulz & H. Wiggers (2015) Direct self-assembly of Fe₂O₃ /reduced graphene oxide nanocomposite for high-performance lithium-ion batteries. *Journal of Materials Chemistry A*, 3, 11566-11574.
- Xiaomei Wang, W. M., Chunmei Ding, Zhiqiang Xu, Hong Wang, Xu Zong, and Can Li (2018) Amorphous Multi-elements Electrocatalysts with Tunable Bifunctionality toward Overall Water Splitting. *ACS Catalysis*, 8, 9926-9935.
- Xie, Q., Z. Cai, P. Li, D. Zhou, Y. Bi, X. Xiong, E. Hu, Y. Li, Y. Kuang & X. Sun (2018) Layered double hydroxides with atomic-scale defects for superior electrocatalysis. *Nano Research*, 11, 4524-4534.
- Xiong, W.-S., Y. Jiang, Y. Xia, Y. Qi, W. Sun, C.-L. Hu, R.-X. He, B. Chen, Y. Liu & X.-Z. Zhao (2018) A sustainable approach for scalable production of α - Fe₂O₃ nanocrystals with 3D interconnected porous architectures on flexible carbon textiles as integrated electrodes for lithium-ion batteries. *Journal of Power Sources*, 401, 65-72.
- Xu, B., X. Guan, L. Y. Zhang, X. Liu, Z. Jiao, X. Liu, X. Hu & X. S. Zhao (2018a) A simple route to preparing γ - Fe₂O₃ /RGO composite electrode materials for lithium ion batteries. *Journal of Materials Chemistry A*, 6, 4048-4054.
- Xu, L., F.-T. Zhang, J.-H. Chen, X.-Z. Fu, R. Sun & C.-P. Wong (2018b) Amorphous NiFe Nanotube Arrays Bifunctional Electrocatalysts for Efficient Electrochemical Overall Water Splitting. *ACS Applied Energy Materials*, 1, 1210-1217.
- Xu, W., F. Lyu, Y. Bai, A. Gao, J. Feng, Z. Cai & Y. Yin (2018c) Porous cobalt oxide nanoplates enriched with oxygen vacancies for oxygen evolution reaction. *Nano Energy*, 43, 110-116.

- Xu, X., Y. Wan, Y. Sha, W. Deng, G. Xue & D. Zhou (2015) Nanoporous iron oxide@carbon composites with low carbon content as high-performance anodes for lithium-ion batteries. *RSC Advances*, 5, 89092-89098.
- Xueyan Huang, X. C., Donghui Xu, Wenyan Chen, Shuanjin Wang, Wuyi Zhou, Yuezhong Meng, Yueping Fang and Xiaoyuan Yu (2018) Hierarchical Fe₂O₃@CNF fabric decorated with MoS₂ nanosheets as a robust anode for flexible lithium-ion batteries exhibiting ultrahigh areal capacity *J.Mater. Chem.A*, 6, 16890-16899.
- Xueying Li, L. C., Yongquan Qu and Yuanyuan Ma (2018) Carbon-assisted conversion reaction-based oxide nanomaterials for lithium-ion batteries *Sustainable Energy & Fuels*, 2, 1124-1140.
- Yan, Y., H. Tang, F. Wu, Z. Xie, S. Xu, D. Qu, R. Wang, F. Wu, M. Pan & D. Qu (2017) Facile synthesis of Fe₂O₃@graphite nanoparticle composite as the anode for Lithium ion batteries with high cyclic stability. *Electrochimica Acta*, 253, 104-113.
- Yang, D., S. Xu, S. Dong, J. Liu, A. Guo, X. Yan & F. Hou (2015) Facile synthesis of free-standing Fe₂O₃/carbon nanotube composite films as high-performance anodes for lithium-ion batteries. *RSC Advances*, 5, 106298-106306.
- Yang, W., Z. Gao, J. Wang, B. Wang & L. Liu (2013) Hydrothermal synthesis of reduced graphene sheets/ Fe₂O₃ nanorods composites and their enhanced electrochemical performance for supercapacitors. *Solid State Sciences*, 20, 46-53.
- Yang, Y., L. Dang, M. J. Shearer, H. Sheng, W. Li, J. Chen, P. Xiao, Y. Zhang, R. J. Hamers & S. Jin (2018) Highly Active Trimetallic NiFeCr Layered Double Hydroxide Electrocatalysts for Oxygen Evolution Reaction. *Advanced Energy Materials*, 8, 1703189.
- Ye, Y.-J., N. Zhang & X.-X. Liu (2017) Amorphous NiFe(oxy)hydroxide nanosheet integrated partially exfoliated graphite foil for high efficiency oxygen evolution reaction. *Journal of Materials Chemistry A*, 5, 24208-24216.
- Yin, S., W. Tu, Y. Sheng, Y. Du, M. Kraft, A. Borgna & R. Xu (2018) A Highly Efficient Oxygen Evolution Catalyst Consisting of Interconnected Nickel-Iron-Layered Double Hydroxide and Carbon Nanodomains. *Adv Mater*, 30.
- Yu, L., J. F. Yang, B. Y. Guan, Y. Lu & X. W. D. Lou (2018a) Hierarchical Hollow Nanoprisms Based on Ultrathin Ni-Fe Layered Double Hydroxide Nanosheets with Enhanced Electrocatalytic Activity towards Oxygen Evolution. *Angew Chem Int Ed Engl*, 57, 172-176.
- Yu, L., H. Zhou, J. Sun, I. K. Mishra, D. Luo, F. Yu, Y. Yu, S. Chen & Z. Ren (2018b) Amorphous NiFe layered double hydroxide nanosheets decorated on 3D nickel phosphide nanoarrays: a hierarchical core-shell electrocatalyst for efficient oxygen evolution. *Journal of Materials Chemistry A*.
- Yu, L., H. Zhou, J. Sun, F. Qin, D. Luo, L. Xie, F. Yu, J. Bao, Y. Li, Y. Yu, S. Chen & Z. Ren (2017a) Hierarchical Cu@CoFe layered double hydroxide core-shell nanoarchitectures as bifunctional electrocatalysts for efficient overall water splitting. *Nano Energy*, 41, 327-336.
- Yu, L., H. Zhou, J. Sun, F. Qin, F. Yu, J. Bao, Y. Yu, S. Chen & Z. Ren (2017b) Cu nanowires shelled with NiFe layered double hydroxide nanosheets as

- bifunctional electrocatalysts for overall water splitting. *Energy & Environmental Science*, 10, 1820-1827.
- Yujie Chen, X. Z., Ying Liu, Amir Abdul Razzaq, Anupriya K. Haridas, Kwon-Koo Cho, Yang Peng, Zhao Deng, Jou-Hyeon Ahn (2018) γ -Fe₂O₃ nanoparticles aligned in porous carbon nanofibers towards long life span LIB. *Electrochimica Acta*, 289, 264-271.
- Yuta Kobayashi, J. A., Koki Kawase, Keisuke Takahashi, Bryan D. Vogt and Seimei Shirator (2018) Enhanced stability of smoothly electrodeposited amorphous Fe₂O₃ @electrospun carbon nanofibers as self-standing anodes for lithium ion batteries *New J. Chem*, 42, 1867-1878.
- Zainab Karam, R. A. S., Ayoob Alhammadi, Ibrahim Mustafa, Chieh-Han Wu, and Saif Almheiri (2018) development of surface engineered tape casting method for fabricating freestanding carbon nanotube sheets containing Fe₂O₃ nanoparticles for flexible batteries. *Advanced Energy Materials*, 20, 1701019.
- Zeyuan Cao, B. W. (2013) α -Fe₂O₃ single-walled carbon nanotube hybridfilms as highperformance anodes for rechargeable lithium-ion batteries. *Journal of Power Sources*, 241, 330-340.
- Zhan, T., Y. Zhang, X. Liu, S. Lu & W. Hou (2016) NiFe layered double hydroxide/reduced graphene oxide nanohybrid as an efficient bifunctional electrocatalyst for oxygen evolution and reduction reactions. *Journal of Power Sources*, 333, 53-60.
- Zhang, C., M. Shao, L. Zhou, Z. Li, K. Xiao & M. Wei (2016a) Hierarchical NiFe Layered Double Hydroxide Hollow Microspheres with Highly-Efficient Behavior toward Oxygen Evolution Reaction. *ACS Appl Mater Interfaces*, 8, 33697-33703.
- Zhang, G., Y. Li, Y. Zhou & F. Yang (2016b) NiFe Layered-Double-Hydroxide-Derived NiO-NiFe₂O₄/Reduced Graphene Oxide Architectures for Enhanced Electrocatalysis of Alkaline Water Splitting. *ChemElectroChem*, 3, 1927-1936.
- Zhang, H., H. Zhao, M. A. Khan, W. Zou, J. Xu, L. Zhang & J. Zhang (2018a) Recent progress in advanced electrode materials, separators and electrolytes for lithium batteries. *Journal of Materials Chemistry A*, 6, 20564-20620.
- Zhang, J., J. Liu, L. Xi, Y. Yu, N. Chen, S. Sun, W. Wang, K. M. Lange & B. Zhang (2018b) Single-Atom Au/NiFe Layered Double Hydroxide Electrocatalyst: Probing the Origin of Activity for Oxygen Evolution Reaction. *J Am Chem Soc*, 140, 3876-3879.
- Zhang, L., J. Xiao, H. Wang & M. Shao (2017a) Carbon-Based Electrocatalysts for Hydrogen and Oxygen Evolution Reactions. *ACS Catalysis*, 7, 7855-7865.
- Zhang, X., Y. Niu, X. Meng, Y. Li & J. Zhao (2013) Structural evolution and characteristics of the phase transformations between α -Fe₂O₃, Fe₃O₄ and γ -Fe₂O₃ nanoparticles under reducing and oxidizing atmospheres. *CrystEngComm*, 15, 8166.
- Zhang, Y., X. Fan, J. Jian, D. Yu, Z. Zhang & L. Dai (2017b) A general polymer-assisted strategy enables unexpected efficient metal-free oxygen-evolution catalysis on pure carbon nanotubes. *Energy & Environmental Science*, 10, 2312-2317.

- Zhong, H., X. Cheng, H. Xu, L. Li, D. Li, P. Tang, N. Alonso-Vante & Y. Feng (2017) Carbon fiber paper supported interlayer space enlarged Ni₂Fe-LDHs improved OER electrocatalytic activity. *Electrochimica Acta*, 258, 554-560.
- Zhou, D., Z. Cai, X. Lei, W. Tian, Y. Bi, Y. Jia, N. Han, T. Gao, Q. Zhang, Y. Kuang, J. Pan, X. Sun & X. Duan (2018a) NiCoFe-Layered Double Hydroxides/N-Doped Graphene Oxide Array Colloid Composite as an Efficient Bifunctional Catalyst for Oxygen Electrocatalytic Reactions. *Advanced Energy Materials*, 8, 1701905.
- Zhou, G., D.-W. Wang, P.-X. Hou, W. Li, N. Li, C. Liu, F. Li & H.-M. Cheng (2012) A nanosized Fe₂O₃ decorated single-walled carbon nanotube membrane as a high-performance flexible anode for lithium ion batteries. *Journal of Materials Chemistry*, 22, 17942.
- Zhou, H., F. Yu, Q. Zhu, J. Sun, F. Qin, L. Yu, J. Bao, Y. Yu, S. Chen & Z. Ren (2018b) Water splitting by electrolysis at high current densities under 1.6 volts. *Energy & Environmental Science*, 11, 2858-2864.
- Zhou, T., Z. Cao, H. Wang, Z. Gao, L. Li, H. Ma & Y. Zhao (2017) Ultrathin Co-Fe hydroxide nanosheet arrays for improved oxygen evolution during water splitting. *RSC Advances*, 7, 22818-22824.
- Zhou, W., X.-J. Wu, X. Cao, X. Huang, C. Tan, J. Tian, H. Liu, J. Wang & H. Zhang (2013) Ni₃S₂ nanorods/Ni foam composite electrode with low overpotential for electrocatalytic oxygen evolution. *Energy & Environmental Science*, 6, 2921.
- Zhou, W., J. Zhu, C. Cheng, J. Liu, H. Yang, C. Cong, C. Guan, X. Jia, H. J. Fan, Q. Yan, C. M. Li & T. Yu (2011) A general strategy toward graphene@metal oxide core-shell nanostructures for high-performance lithium storage. *Energy & Environmental Science*, 4, 4954.
- Zhu, S., M. Chen, W. Ren, J. Yang, S. Qu, Z. Li & G. Diao (2015) Microwave assisted synthesis of α -Fe₂O₃/reduced graphene oxide as anode material for high performance lithium ion batteries. *New Journal of Chemistry*, 39, 7923-7931.
- Zhu, W., L. Liu, Z. Yue, W. Zhang, X. Yue, J. Wang, S. Yu, L. Wang & J. Wang (2017) Au Promoted Nickel-Iron Layered Double Hydroxide Nanoarrays: A Modular Catalyst Enabling High-Performance Oxygen Evolution. *ACS Appl Mater Interfaces*, 9, 19807-19814.